Corso di dottorato di ricerca in scienze biomediche e biotecnologiche

Ciclo XXX

Titolo della tesi

"Challenging protein-nanoparticle interactions.
Results with gold nanoparticle and β2-microglobulin system."

Dottorando
Cristina Cantarutti

Supervisore
Prof. Gennaro Esposito

Co-supervisore
Dott.ssa Alessandra Corazza

Anno 2017/201

INDEX

Abstract

The work presented here deals with the investigation of the interaction of gold nanoparticles (AuNPs) with a paradigmatic amyloidogenic protein, namely β2-microglobulin (β2m). The interaction between proteins and nanoparticles is currently a topic of great interest concerning both nanomedical applications and nano-safety issues. However, a deep knowledge about the molecular mechanisms that drive these interactions is still lacking.

To contribute improving the understanding of these interactions, several techniques (dynamic light scattering, microscopy, nuclear magnetic resonance, fluorescence and UV-Vis spectroscopy and quartz crystal microbalance) were exploited to elucidate the characteristics of protein-NP systems. β2m was chosen as a convenient model for amyloidogenic proteins that are quite unstable polypeptides with a high tendency to misfold and aggregate into fibrils. Among the nanoparticles, AuNPs were selected for their versatility and their widespread application.

AuNPs with different organic shell composition were synthesized, characterized and tested mainly with β2m wild-type and in some cases also with two more amyloidogenic variants, i.e. ΔN6 and D76N. The obtained results showed that the nature of the organic shell and the dimensions of AuNPs play a critical role in determining the nature of the interaction.

It has been found that 7.5 nm citrate-stabilized AuNPs (Cit-AuNPs) form transient adducts with β2m that proved capable of reducing protein association and aggregation and, as far as ΔN6 variant is concerned, to avoid intrinsic protein partial unfolding. Furthermore, Cit-AuNPs were able to partially hamper D76N fibrillogenesis *in vitro*. AuNPs coated with 6-mercaptohexanoic acid (MHA), (11-mercaptoundecyl)-N,N,N-trimethylammonium (MUTAB) were prepared starting from Cit-AuNPs and smaller 3-mercaptopropionic acid (MPA) AuNPs were obtained through a

direct synthesis. It was found that MHA-AuNPs caused β2m unfolding and its precipitation in protein-NP large agglomerates. On the other hand, MUTAB-AuNPs in presence of β2m irreversibly aggregate while the overall protein structure was preserved except for some minimal conformational changes. With the smaller MPA-AuNPs β2m formed dynamic complexes through a highly localized patch maintaining mainly its native structure. These results underline once again the complexity and the versatility of protein-NP systems, but also suggest the possibility to exploit these interactions to interfere with physiological or pathological processes.

Regardless the specific results obtained with the particular protein-NP system considered, in this thesis the inadequacy of some techniques to describe quantitatively protein-NP interactions and the care that should be taken in the interpretation of the results are highlighted.

Abbreviations

2D	Two dimensional
AFM	Atomic force microscopy
AHT	6-aminohexane thiol
ANS	1-anilinonaphtalene-8-sulfate
AT-AuNPs	Alkanethiolate-covered gold nanoparticles
AuNPs	Gold nanoparticles
AuNRs	Gold nanorods
β2m	β2-microglobulin
BSA	Bovine serum albumin
CD	Circular dichroism
Cit-AuNPs	Citrate-stabilized gold nanoparticles
CPMG	Carr-Purcell-Meiboom-Gill
cryoEM	Cryoelectron microscopy
CSA	Chemical shift anisotropy
Cya	Cysteamine
Δδ	Chemical shift difference
$\Delta\delta_{av}$	Average chemical shift difference
ΔD_{sat}	Dissipation change at saturation
Δf_{sat}	Frequency change at saturation
ΔN6	β2m devoid of first six residues at the N-terminus
ΔG	Gibbs free energy
D76N	β2m mutated as Asp in position 76 is replaced by Asn
DCVJ	4-(dicyanovinyl)-julolidine
DD	Dipole-dipole interaction
DEST	Dark state exchange saturation transfer

DLS	Dynamic light scattering
DOSY	Diffusion ordered spectroscopy
DRA	Dialysis-related amyloidosis
DSTEBPP	Double stimulated echo bipolar pulse
HEPES	4-(2-hydroxyethyl)-1-piperazineethanesulfonic acid
HSQC	Heteronuclear single quantum correlation
IR	Infrared
ITC	Isothermal titration calorimetry
MHA	6-mercaptohexanoic acid
MHA-AuNPs	6-mercaptohexanoic acid-coated gold nanoparticles
MHC I	Major histocompatibility complex class I
MPA	3-mercaptopropionic acid
MPA-AuNPs	3-mercaptopropionic acid-coated gold nanoparticles
MUTAB	(11-mercaptoundecyl)-N,N,N-trimethylammonium bromide
MUTAB-AuNPs	(11-mercaptoundecyl)-N,N,N-trimethylammonium-AuNPs
NMR	Nuclear magnetic resonance
NOE	Nuclear Overhauser effect
NPs	Nanoparticles
PICUP	Photo-induced cross-linking
QCMD	Quartz crystal microbalance dissipation
R_1	Longitudinal relaxation rate
R_2	Transverse relaxation rate
$R_{1\rho}$	Rotating-frame relaxation rate
RI	Relative intensity
RI_{av}	Average relative intensity
SC	Side chain
SDS-PAGE	Sodium dodecyl sulphate polyacrylamide gel electrophoresis
SOFAST-	Band-selective optimized flip-angle short-transient

HMQC	heteronuclear multiple quantum coherence
SPR	Surface plasmon resonance
TA	Thioctic acid
TA/AHT-AuNPs	Thioctic acid and 6-aminohexane thiol-coated AuNPs
TEM	Transmission electron microscopy
TGA	Thermogravimetric analysis
ThT	Thioflavin T
TIRFM	Total internal reflection fluorescence microscopy
TPE-TPP	Tetraphenylethene-triphenylphosphonium
UV-Vis	UV-visible
W60G	β2m mutated as Trp in position 60 is replaced by Gly
WATERGATE	Water suppression by gradient tailored excitation
WT	Wild-type

Amino acids abbreviations

Amino acid	One letter abbreviation	Three letters abbreviation
Alanine	A	Ala
Cysteine	C	Cys
Aspartic acid	D	Asp
Glutamic acid	E	Glu
Phenylalanine	F	Phe
Glycine	G	Gly
Histidine	H	His
Isoleucine	I	Ile
Lysine	K	Lys
Leucine	L	Leu
Methionine	M	Met
Asparagine	N	Asn
Proline	P	Pro
Glutamine	Q	Gln
Arginine	R	Arg
Serine	S	Ser
Threonine	T	Thr
Valine	V	Val
Tryptophan	W	Trp
Tyrosine	Y	Tyr

1 INTRODUCTION

In the last years the production, the characterization and the application of nanomaterials have attracted the interest of many fields of science like physics, chemistry, biology and material science.[1–4] In particular, nanoparticles (NP) assumed a central role because of their peculiar and unique mechanical, optical, chemical and magnetic properties.[5–7]

From a biomedical point of view, NPs are intriguing tools to develop new smart nanobiomaterials for theranostic applications, but the increasing spread of their use calls for attention on their safety assessment.[8,9] Therefore, research efforts must be performed both in nanomedicine and in nanotoxicology.

In this frame, the investigation of the interaction between nanoparticles and proteins is of the highest concern.

1.1 Nanoparticle-protein corona formation

NP tendency to reduce their surface energy by interacting with the surrounding entities drives the NP surface coverage by biomacromolecules, among which proteins are the most abundant ones, as soon as NPs contact a biological system.[10,11] This dynamic protein layer, called corona (Figure 1.1), modulates the behaviour of the NP in the biological environment and the cellular response. It has been demonstrated that there can be an inner layer of proteins strongly bound to the gold surface with a long residence time, i.e. hard corona, and a second shell of proteins, called soft corona, which is characterized by a weaker interaction and a fast exchange rate.[12,13] It is the protein corona that actually interacts with the cellular receptors and determines the impact of the nanomaterial on the biological system.[14]

Therefore, understanding the protein layer composition and organization is a crucial issue in predicting NP safety.

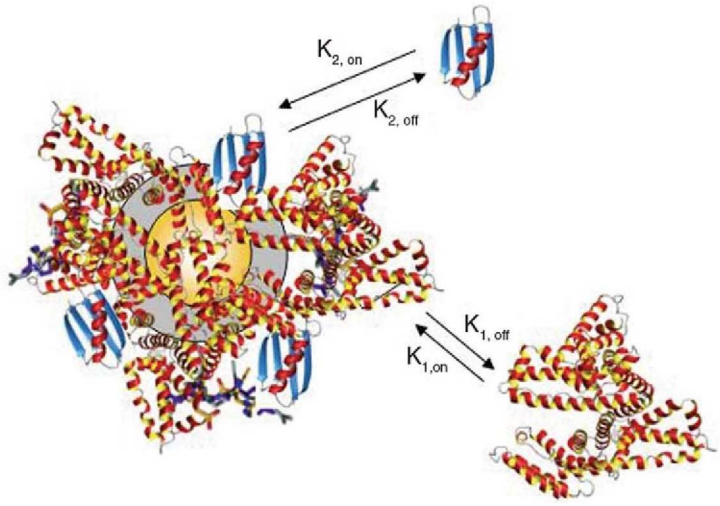

Figure 1.1 Protein corona schematic representation. The exchange processes with their constants are indicated for two different proteins.[15]

The corona nature depends on many factors such as the NP physico-chemical properties, the protein/NP ratio and the specific protein features.[16] Different proteins show different affinities for NP surfaces and can be more or less strongly associated with various exchange kinetics. The first layer of proteins can be reversibly or irreversibly bound depending on binding constants and exchange kinetics. Considering gold nanoparticles, for example, it has been proposed that after a first step of reversible association, the protein undergoes a reorientation in order to increase the packing density and then, for proteins bearing surface cysteines, the binding becomes irreversible.[17]

1.2 Protein conformational response to nanoparticle binding

Proteins are polymers characterized by a specific amino acid sequence which defines their structure. The secondary structure is the local arrangement of the polypeptide chain. There are two main local structural

units, namely α-helix and β-strand. The overall three-dimensional arrangement of these units is the tertiary structure. The native structure of a protein is strictly linked to its function implying that any perturbation of the latter can lead to severe biological consequences. This explains why the NP interaction effect on protein conformation is a key point when investigating NP biological impact.

It has been shown that the adsorption of proteins on NP surfaces can affect either in a reversible or irreversible manner the protein conformation with potential variation of the function and behaviour.[18,19] For example, it has been shown that the interaction of bovine serum albumin (BSA) with gold nanoparticles essentially preserves the native-like protein structure and its esterase activity, whereas in presence of gold nanorods (AuNRs) BSA substantially loses its secondary and tertiary structure along with its enzymatic activity.[20] Moreover, while AuNPs did not modify the BSA fibrillation kinetics, AuNRs increase the rate of amorphous aggregate formation.

1.3 Methods for protein corona investigation

Several methods are commonly used to study protein-nanoparticle interaction in order to estimate the binding parameters, e.g. thermodynamic constants, kinetic rates and stoichiometry, and elucidate the implications on protein structure.

UV-visible spectroscopy

The absorption spectrum of nanoparticles has been shown to be influenced by protein-NP adduct formation.[21–24] For example, it was reported that adding progressive amounts of azurin to gold nanoparticles lead to red shift and broadening of the NP absorption band.[25] This phenomenon appears to be suitable to study the binding in a fast and easy way, but quantitative

results should be taken with proper care, since the contributions to the spectrum shape, position and intensity are often not so trivial and simple to address, especially in the highly complex NP supramolecular systems.

Fluorescence spectroscopy

Proteins and nanoparticles could be labelled with fluorescent probes whose emission response can be used to track the protein-NP interaction. However, the introduction of dyes can affect protein binding leading to artefacts. If the protein bears tryptophan residues that contribute to a significative intrinsic fluorescence, this technique can be exploited to prove the protein structural modifications introduced by the NP presence and monitor the NP-protein binding. Steady-state or time-resolved fluorescence spectroscopy,[21,23,26] fluorescence resonance energy transfer (FRET),[27–29] stepwise single-molecule photobleaching[30] and fluorescence correlation spectroscopy (FCS)[31] have all been used to investigate protein-NP interactions.

Infrared and Raman spectroscopy

Vibrational spectroscopies, Raman and infrared (IR), can be used to investigate the conformation and secondary structure of proteins when they bind to NPs. With IR spectroscopy, the changes in amide I band (1700 – 1600 cm^{-1}) are mainly used to sense eventual perturbations in protein conformation or to monitor isotopic exchange[27,32,33] instead with Raman it is possible to access more detailed information not only about the backbone, but also about the aromatic and sulfur-including side chains.[34,35] For example, it was demonstrated that the heme vinyl groups of haemoglobin change their orientation from in-plane to out-of-plane as a consequence of the interaction with bare CdS quantum dots.[34]

Circular dichroism

Circular dichroism spectra are characteristic of different secondary structures, therefore by this spectroscopic technique it is possible to evaluate if the interaction of the protein with the NP affects the extent of α-helices and β-sheets.[22,27,36] Unless NP size is not too big to give scattering contributions, NP usually do not interfere with the protein CD spectrum. This approach is very convenient to analyse the protein conformational changes, but it is not able to give any information about the locations involved in the structural rearrangement. To reach more specific molecular insights, other techniques must be exploited.

Dynamic light scattering

In dynamic light scattering (DLS), the autocorrelation function of the scattered light intensity is measured and used to calculate by a Laplace transform the particle hydrodynamic size distribution. DLS is used to detect the increase in NP hydrodynamic diameter upon protein adsorption and to estimate the ratio of the binding.[37,38] However, this technique has some drawbacks. Being the scattered intensity proportional to the sixth power of the particle radius, the contribution from larger particles could dominate leading to artefacts especially if the samples are polydisperse.

Isothermal titration calorimetry

Fitting by an isothermal function the heat changes measured when the NP solution is titrated with the protein, the thermodynamic parameters of the interaction can be calculated.[20,27,39] The results obtained with isothermal titration calorimetry (ITC) for the system made up of quantum dots and human serum albumin revealed that the binding is mainly driven by electrostatic interactions because negative enthalpy and positive entropy values were found.[27] Cedervall *et al*.[12] showed that ITC is a proper method to

analyse the affinity and stoichiometry of NP-protein complexes in a quantitative and reliable way.

Nuclear magnetic resonance

Nuclear magnetic resonance (NMR) gives the possibility to investigate with high precision the effects of intermolecular interactions on protein structure and dynamics and to map the protein regions that are more perturbed. By labelling the protein of interest with particular isotopes, mainly ^{15}N, it is possible to observe protein NMR spectra without NP signals interference. Local mobility, exchange kinetics, rotational and translational diffusion can be probed performing specific NMR experiments. Unfortunately, the unique possibilities offered by this technique are limited by its quite low sensitivity, i.e. high protein concentration requirements, and by the restricted molecular size range operativity, i.e. only proteins with MW < 25 kDa are suitable for the required NMR determinations. Protein-NP adducts have been studied by NMR exploiting different experiments: signal chemical shift perturbation and intensity variation in ^{1}H-^{15}N two-dimensional experiments were used mainly to identify interaction patches and conformational rearrangements,[38,40–44] hydrogen-deuterium exchange experiments were used to control structural changes that occur on different time scales[17,45] and saturation transfer experiments proved to be able to detect exchanging invisible species estimating the exchange rates.[46,47]

Quartz crystal microbalance

Quartz crystal microbalance (QCM) measures the changes in the resonance frequency of an oscillating quartz crystal positioned between two electrodes when additional mass adsorbs onto the substrate. The frequency variation, Δf, is proportional to the mass density of the adsorbed material.[48] This very sensitive technique allows one to investigate the behaviour of proteins and nanoparticles during deposition and to observe any change in

surface affinity. For example, Franzen *et al.* probed by QCM the adsorption of BSA on citrate-coated gold nanoparticles and on gold surfaces revealing that while BSA denaturates on bare gold, the presence of citrate allows an interaction that preserves protein overall folding.[49]

1.4 Effect of protein-NP interaction on protein fibrillation

The interaction with NP can affect not only the structure and conformation of proteins, but also their behaviour under specific conditions. Particularly, it is recognized that the presence of NP can have different effects on amyloidogenic protein fibrillation.

1.4.1 Protein fibrillation and amyloidosis

Amyloidogenic proteins undergo a conversion from a soluble native-like structure to insoluble fibrillary aggregates whose deposition on body tissues have been identified as the cause of many serious pathologies like Alzheimer's and Parkinson's diseases.[50]

Amyloid fibres are characterized by a common structure, i.e. cross-β structure, made up of extended intermolecular β-sheets in which β-strands are perpendicular to the major axis of the fibril.[51–53] The vast occurrence of this particular structure is quite surprising because amyloidogenic proteins are known to have highly different native conformations. It has been proposed that the cross-β structure is a general structural pattern of polypeptides and the formation of amyloid fibrils happens when the protein native state is destabilized and undergoes partial unfolding through conformation changes.[54] The flexibility of the partially folded intermediates thus produced could explain their ability to undergo the conformational rearrangements needed to achieve the cross-β structure.

1.4.1.1 β2-microglobulin

β2-microglobulin is a paradigmatic amyloidogenic protein since it resembles all the characteristic features of this class of proteins. In addition of being a model for amyloidogenic proteins, it is itself responsible of dialysis-related amyloidosis (DRA), a pathology that affects patients with chronic renal failure treated with long-term hemodialysis.[55] β2m is the nonpolymorphic light chain of the class first major histocompatibility complex (MHC I) from which it detaches because of the continuous regeneration of the membrane proteins. After the separation from the heavy chain, β2m is secreted in the plasma and reaches the kidneys to be excreted. If the kidneys are damaged, they couldn't remove β2m from the blood and it consequently accumulates. Moreover, being a small protein the dialysis apparatus is not able to completely filter it away from blood. The resulting up to 60-fold concentration increase causes the protein tissue-specific deposition into amyloid fibrils especially at the joints.

The primary sequence of β2m is constituted by 99 residues and its molecular weight is 11.8 kDa. The seven anti-parallel β-strands that characterize β2m secondary structure fold into a typical β-sandwich immunoglobulin motif stabilized by a single disulfide bridge between Cys25 and Cys80 which belong to strand B and strand F, respectively (Figure 1.2).[56,57]

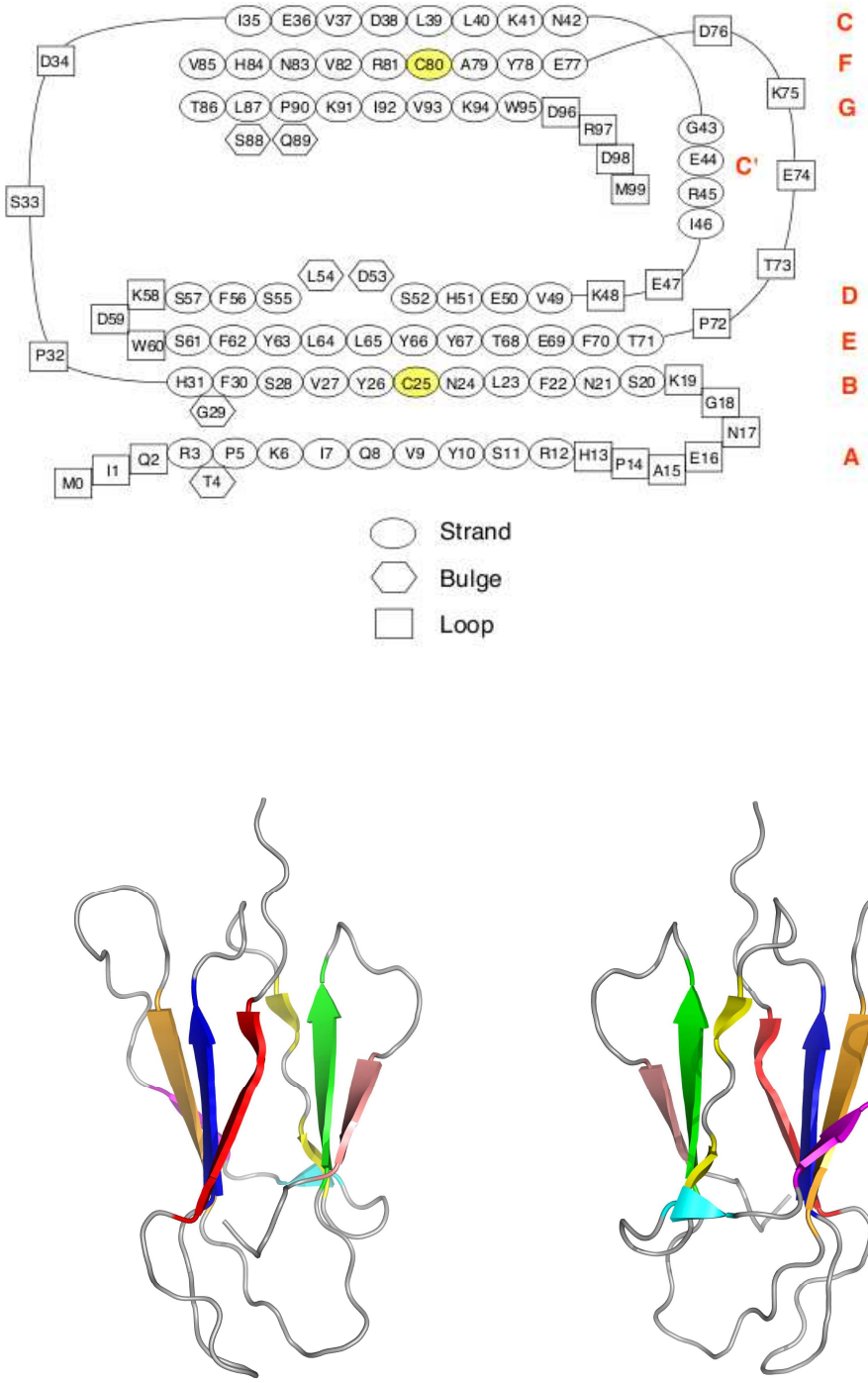

Figure 1.2. Scheme of primary and secondary β2m structures (above). The two cysteines that form the disulphide bridge are coloured in yellow. The strand naming is reported on the right. Cartoon of β2m solution NMR structure (below): A strand in red, B strand in blue, C strand in yellow, C' strand in cyan, D strand in magenta, E strand in orange, F strand in green and G strand in salmon.

There are five peptidyl-prolyl bonds in β2m structure, the one preceding Pro32 in the BC-loop adopts a *cis* configuration that is thermodynamically unfavourable. Upon unfolding, His31-Pro32 peptide bond isomerizes from *cis* to *trans*. This proline switch is considered to have a crucial role in the development of destabilized intermediates that lead to β2m amyloidogenic transition.[58]

An alternative mechanism that accounts for the tissue-specific β2m amyloid deposition considers an electrostatic surface effect. It was shown that β2m aggregates preferentially in presence of collagen and glycosaminoglycans that exposes positively and negatively charged surfaces. The presence of charge arrays could affect the protein conformational stability provoking a spontaneous destructuration.[59]

There are many β2m variants that have been studied during the last years. Among them, D76N and ΔN6 are particularly interesting.

D76N is the variant in which the Asp in position 76 is replaced by an Asn, it is naturally occurring and it is related to a fatal hereditary systemic amyloidosis.[60] This mutant is the only one able to fibrillate *in vitro* under physiological conditions requiring only agitation, whereas all the other β2m forms need acidic conditions.[61] The three-dimensional structure of D76N is almost the same as the wild-type even if it is destabilized with an unfolding ΔG value of 2.86 kcal mol^{-1} lower than wild-type at 30 °C.[61] Its increased amyloidogenicity is related to a higher amount in the folding pathway of a specific intermediate which is critical in amyloid transition.[61]

Six N-terminally truncated (ΔN6) β2m is the most abundant variant present in *ex vivo* fibrils.[62] It has been demonstrated that *in vitro* it has a higher propensity to aggregate in fibrils than the wild-type and while the overall globular structure is maintained by the disulfide bridge, the strands pairing is slightly perturbed leading to a loss of inner core protection.[63]

1.4.2 Fibrillogenesis analysis

The most direct way to assess and follow fibril formation is microscopy observation. Transmission electron microscopy (TEM) and atomic force microscopy (AFM) allow to clearly visualize the fibres morphology and in some cases to detect the oligomers that are produced during the early phase of amyloidosis.[64,65] Among the microscopic techniques, AFM is preferred because while TEM samples must be dried with the risk of potential alteration of the fibres, AFM can be performed also in liquid phase.

Historically, however, the established method to detect amyloid fibrils is the Congo Red assay based on the typical green birifrangence upon visualization under polarized light of specimens stained with the organic dye Congo Red.[66] The birifrangent behaviour stems from the ordered structural organization of amyloid fibrils that prove anisotropic for the propagation of polarized light.

An indirect method to detect fibrils and follow the fibrillogenesis kinetic is the use of fluorescence probes that bind to amyloids. The most common dye is thioflavin T (ThT) whose fluorescence rapidly increases upon its binding to the highly ordered structures of the fibres.[67] ThT was also used to label fibres during total internal reflection fluorescence microscopy (TIRFM) which has been used to analyse the morphology of the fibrils.[68] Other probes like 1-anilinonaphtalene-8-sulfate (ANS),[69] 4-(dicyanovinyl)-julolidine (DCVJ)[70] and tetraphenylethene-triphenylphosphonium (TPE-TPP)[71] have been shown to be able to detect also prefibrillar oligomeric species in the early phase of protein fibrillation.

Another way to identify protein oligomers, i.e. fibril precursors, is photo-induced cross-linking (PICUP).[72,73] The extremely rapid photolysis of a tris-bipyridyl Ru(II) complex leads to highly reactive Ru(III) species which generate carbon radicals within the main chain of the polypeptide. These radicals react quickly producing carbon-carbon bonds between groups that

are spatially close. Then, cross-linked oligomers are analysed by SDS-PAGE. The nature of the oligomers that accumulate in the first steps of aggregation can be elucidated by their separation onto an agarose gel through electrophoresis followed by their transfer onto a semi-dry membrane and the application of a monoclonal antibody against the monomer.[74]

The atomic three-dimensional structure of amyloids can be determined by solid state NMR which allows to investigate the supramolecular organization of the amyloids.[75] In addition, the recent advances in cryoelectron microscopy (cryoEM) methodologies have made possible the application of the technique also to amyloids.[76] The electron densities that are observed by cryoEM can be fit to extract the parent molecular arrangement.

1.4.3 Effect of NP on fibril formation

Protein fibrillation is a very complex phenomenon that can be influenced by intermolecular interactions with foreign substances, like small organic molecules (e.g. inositols, phenols and indoles),[77–79] peptides[80] and macromolecules (e.g. antibodies and molecular chaperones).[81–83] With the increasing interest in NP medical applications and in the related toxicological issues, the effect of nanomaterials on amyloid formation started to be investigated. Different and contrasting results have been reported revealing the impossibility to draw general trends.[84] The interaction patterns are case-specific and depend both on protein surface properties and on NP features. In some cases, NPs have been shown to promote protein fibrillogenesis. Linse *et al.*[85] found that cerium oxide nanoparticles, quantum dots, carbon nanotubes and copolymeric nanoparticles enhance the fibrillation process of β2m wild-type in acidic conditions. They claimed that the protein binding on NP surface increases the local β2m concentration and facilitates the protein intermolecular interactions which promote the fibre assembly. Other studies reported the capability of NP to hinder the amyloid formation. For example,

maghemite (γ-Fe_2O_3) particles showed an inhibitory effect on insulin fibril formation[86] and nanogels composed of a pullulan polysaccharide backbone with hydrophobic cholesterol moieties induce a change in the conformation of Aβ from a random coil to an α-helix- or a β-sheet-rich structure that is fibrillation incompetent.[87] If there is not a specific effect on protein conformation, the reduction in fibril formation is usually explained by a competition effect of the NP-protein interaction which removes the protein from the fibrillogenesis pathway.[88] Nanoparticles can also leave the fibrillogenesis process unchanged without any interference, as for silica, C_{60} and C_{70} NPs on Aβ peptide.[89] A dual effect was observed with amine-modified polystyrene NPs on Aβ fibres formation depending on the protein to NP surface area ratio.[90] The fibrillation was accelerated at low particle surface area, whereas it was inhibited at high particle surface area.

The depicted scenario tells that further efforts must be undertaken to improve the understanding of the complex effects of the nano-bio interfaces on protein fibrillation.

2 AIM OF THE PROJECT

This PhD thesis deals with the investigation of protein-NP interactions.

The adduct formed by gold nanoparticles (AuNPs) and the amyloidogenic protein β2-microglobulin (β2m) was characterized at a molecular level and the effects of this interaction on protein conformation and fibrillation were examined.

Gold nanoparticles are supramolecular systems made up of a gold core and an organic shell. AuNPs are excellent candidates for biomedical applications because of their unique properties, such as size and shape dependent optical features, large surface to volume ratio, gold inertness and surface functionalization versatility.[91] A great variety of AuNPs have been prepared for biological tasks like drug delivery, gene transfection, RNA interference, imaging and photothermal therapy.[92] Although some studies have been performed, there are still no general conclusions about their toxicity since their biocompatibility and biodistribution is extremely dependent on their shape, size and on the chemistry of the surface coatings.[93,94] Even more scarce is the identification of general trends concerning their effect on proteins, especially if amyloidogenic proteins are considered.

To contribute in filling this lack, the PhD project presented here analyses the molecular aspects related to the formation of an adduct between AuNPs with different ligand shell composition and β2m that, beyond being itself responsible for dialysis-related amyloidosis (DRA), is a paradigmatic amyloidogenic protein.[55] Moreover, the consequence of this interaction on protein association and aggregation into fibrils was assessed.

To reach this aim differently capped AuNPs were prepared and the interaction between synthesized AuNPs and β2m was analysed by different techniques underlining the resources offered by each technique to address different issues but sometimes also their inadequacy.

3 METHODS

3.1 AuNP synthesis and characterization

It is well known that gold surfaces can adsorb easily organic molecules through a process called self-assembly. The presence of an organic layer that covers the gold surface is particularly important in the case of gold nanoparticles since it provides stability to the colloidal solution preventing the gold core aggregation. The ligands can be weakly bound to the surface by electrostatic interactions or can be covalently anchored and the strength of the interaction reflects the stability of the nanoparticles.

Turkevich *et al.* proposed a synthetic method that allows to prepare gold nanoparticles stabilized by citrate.[95] The carboxylate groups of citrate anions coordinate to the metal surface and the electrostatic repulsion between the negatively charged citrate molecules avoids the NP aggregation. Citrate-stabilized AuNPs (Cit-AuNPs) can be thus considered the simplest kind of nanoparticles. Among all the possible ligands e.g. amines and phosphines, the ones that produce the more stable organic monolayers are thiols. Gold forms with sulfur covalent bonds that are characterized by an energy of 45 kcal/mol, approximately.[96] In addition to the sulfur atom that binds the gold surface, thiols are made of a linker chain and a terminal group. Usually, the linker corresponds to an alkyl or polyethylene glycol chain of variable length. Van der Waals interactions between the chains are essential to confer stability to the nanoparticles. As far as the ending group is concerned, a variety of solutions is possible giving to the NPs different surface properties. Alkanethiolate coated AuNPs (AT-AuNPs) are mostly synthesized by the Brust and Schiffrin method.[97] This synthetic approach can be in double phase (water/toluene) if the resulting NPs are soluble in organic solvents or in single phase if the NPs are water soluble. An alternative route to the direct synthesis is the place-exchange reaction. It is possible to displace the weakly

bound citrate molecules by incubating Cit-AuNPs with an excess of thiols. However, sometimes this process can cause irreversible aggregation. The same reaction can be done also on AT-AuNPs producing mixed-monolayer protected gold clusters.

In this section, the synthesis methods and the characterization analysis of Cit-AuNPs and AT-AuNPs are presented.

To prepare citrate-stabilized gold nanoparticles with a size range from 5 to 10 nm, a standard cold synthesis using $NaBH_4$ as gold reducing agent was employed,[38] varying the gold/citrate ratio (Scheme 3.1). The ratio between the gold salt used as a precursor of nanoparticles and the ligand is in general crucial in determining the NP size.

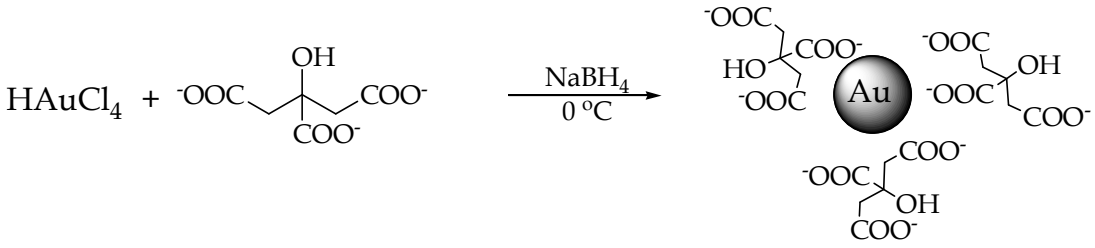

Scheme 3.1. Cit-AuNP synthesis.

The colloidal nature of the solution was assessed by the presence of the Surface Plasmon Resonance (SPR) band[98] in the UV-Vis spectrum with an absorbance maximum at 518 nm (Figure 3.1 a). The average diameter of the nanoparticles was determined analysing the transmission electron microscopy images of the nanoparticles (Figure 3.1 b).

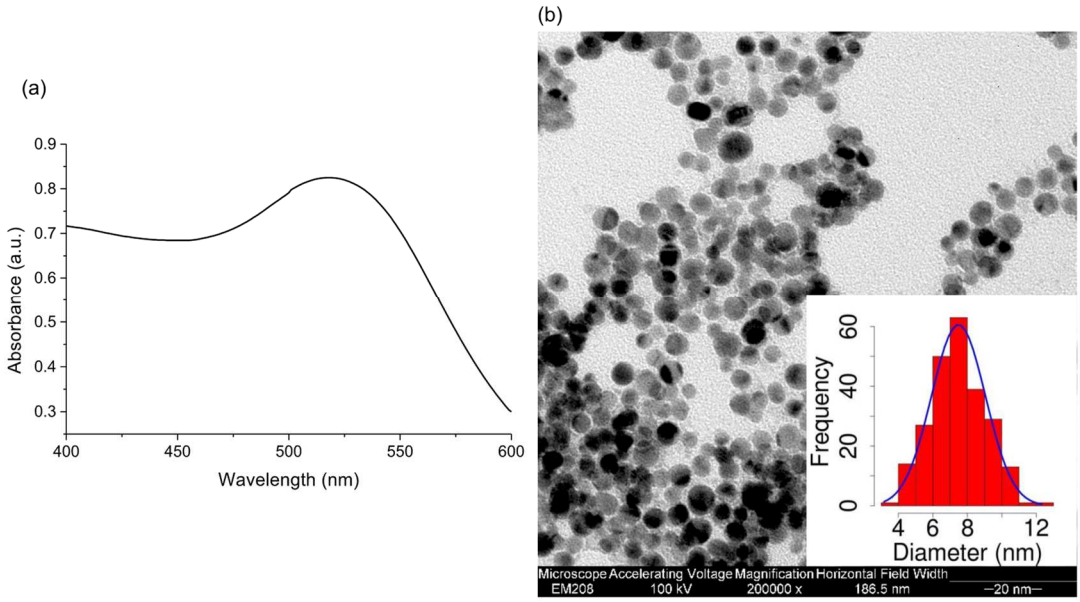

Figure 3.1. a) Absorption spectrum and b) TEM micrograph of synthesized Cit-AuNPs. The insert presents the size distribution histogram.

To determine the NP concentration, the following equation[99] that allows one to calculate the average number of gold atoms per NP (N_{Au}) was applied:

$$N_{Au} = \frac{\pi}{6}\frac{\rho d^3}{M_{Au}} = 30.89602 d^3$$

Equation 3.1

where d is the nanoparticle diameter expressed in nm, ρ is the density for face-centered cubic gold (19.3 g/cm^3) and M_{Au} stands for the atomic weight of gold (197 g/mol).

Knowing the amount of reduced gold from the absorbance at 400 nm[100] and the volume of the solution, the NP concentration can be estimated.

The pH of the reaction solution was basic (8.2) due to the hydrolysis of $NaBH_4$.[101] The NPs could not be buffered with phosphate (20 mM, pH 7) because the high ionic strength affected the NP stability and led to precipitation, whereas in HEPES 50 mM pH 7 Cit-AuNPs were found to be perfectly stable.

The weakly bound citrate molecules were exchanged with mercaptocarboxylic acids to introduce a ω-carboxylate alkyl coating. A first attempt was done using 3-mercaptopropionic acid (MPA), but after the addition of different amounts of the thiol, the nanoparticles suddenly aggregated and precipitated. MPA is too short and does not establish enough van der Waals interactions leading to monolayer instability and nanoparticle irreversible aggregation during the exchange. Mercaptocarboxylic acids with longer alkyl chains like 6-mercaptohexanoic acid (MHA) are able to stabilize sufficiently the nanoparticles preventing their aggregation. To produce MHA-AuNPs the procedure reported in literature[102] and depicted in Scheme 3.2 was followed.

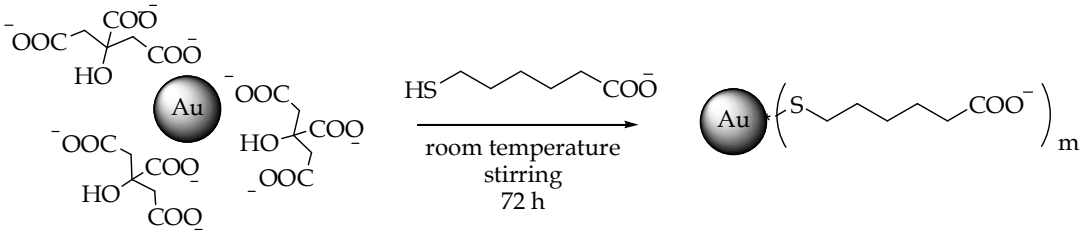

Scheme 3.2. MHA-AuNP synthesis through place-exchange reaction.

After the addition of MHA, the solution colour became a little darker and the SPR band shifted, but the NP core average size did not change (Figure 3.2). These considerations suggest that the ligand exchange took place.

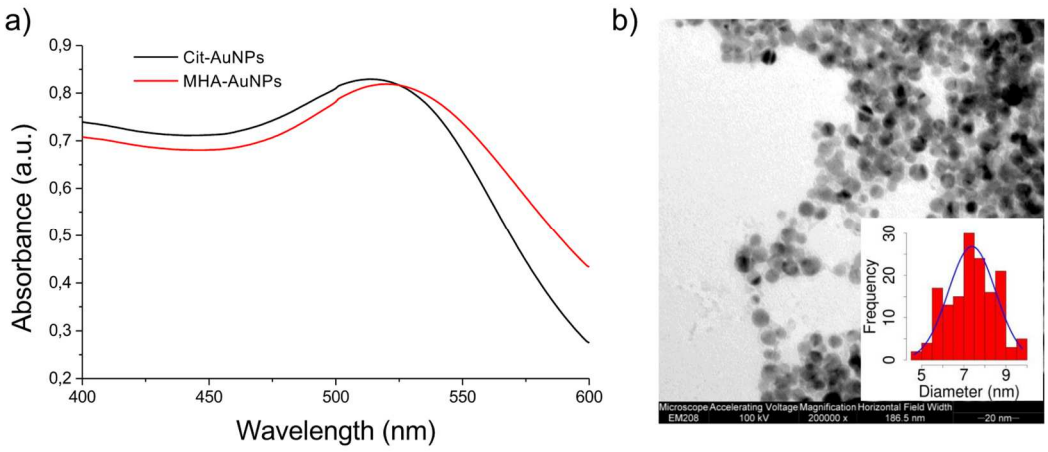

Figure 3.2. a) Overlap of Cit-AuNP (black line) and MHA-AuNP (red line) UV-Vis spectra and b) TEM micrograph and size distribution histogram of MHA-AuNPs.

Since to obtain MPA-AuNPs a place-exchange reaction could not be undertaken, a direct single-phase synthesis[103] using MPA was employed to produce negatively charged AuNPs with a diameter smaller than 5 nm which could not be achieved using citrate as stabilizing agent (Scheme 3.3).

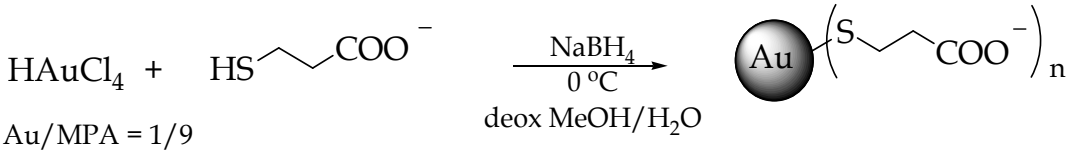

Scheme 3.3. MPA-AuNP direct synthesis.

The average diameter was found to be 3.6 ± 1.3 nm from TEM (Figure 3.3 a). The SPR band in the UV-Vis spectrum was very weak because of the small size of the NPs (Figure 3.3 b). To estimate the NP concentration, it was necessary to determine their composition. First, MPA-AuNPs were purified by centrifugation and dried in vacuum. The gold core composition was calculated from Equation 3.1 and the number of ligands that are bound to the gold core was estimated from thermogravimetric analysis (TGA). This experiment gives the percentage of weight loss during a temperature ramp (from 0 to 600 °C) that is addressed exclusively to the burning of the organic

component, following solvent removal. Applying the following equation, it is possible to calculate the monolayer composition:

$$N_L = \frac{N_{Au} M_{Au} W\%}{(1 - W\%) M_{thiolate}}$$

Equation 3.2

where N_L is the number of ligands, $W\%$ is the percentage of weight loss due to organic ligands burning and $M_{thiolate}$ is the molecular weight of the thiolate molecule.

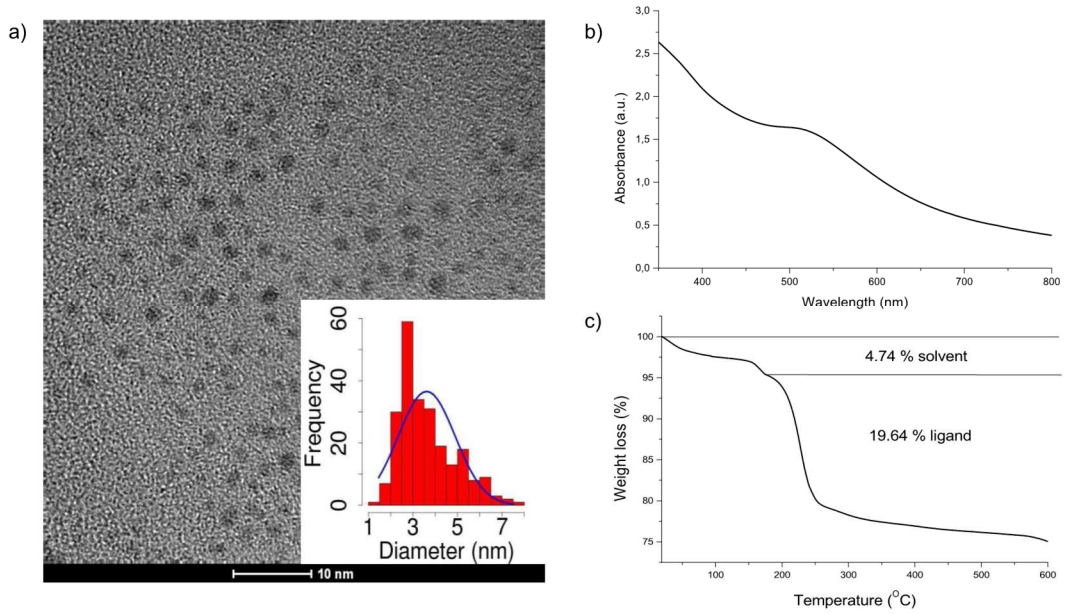

Figure 3.3. a) TEM micrograph of MPA-AuNPs along with the corresponding size distribution histogram showed in the inset; b) UV-Vis spectrum of MPA-AuNPs presenting a very broad SPR peak around 505 nm and c) TGA analysis of MPA-AuNPs.

Combining this information with the size of the nanoparticles, the average composition of the nanoparticles was determined (Table 3.1) and their concentration can be easily calculated.

Table 3.1. Composition of MPA-AuNPs.

Core diameter (nm)	Organic percentage (%)	Average composition	Molecular weight (g/mol)
3.6	19.64	$Au_{1441}(SCH_2CH_2COO^-)_{661}$	353315.33

The synthesis of positively charged gold nanoparticles was much more challenging. A monolayer made by ω-aminothiols seemed to be suitable to reach this aim. First, cysteamine (Cya) was chosen, but exchange reaction starting from Cit-AuNPs failed for the same reason as for MPA. A direct synthesis following a procedure reported by Feng *et al.* to prepare 3-mercapto-propylamine-coated gold nanoparticles was used,[104] but with cysteamine it produced agglomerated nanoparticles as shown in Figure 3.4.

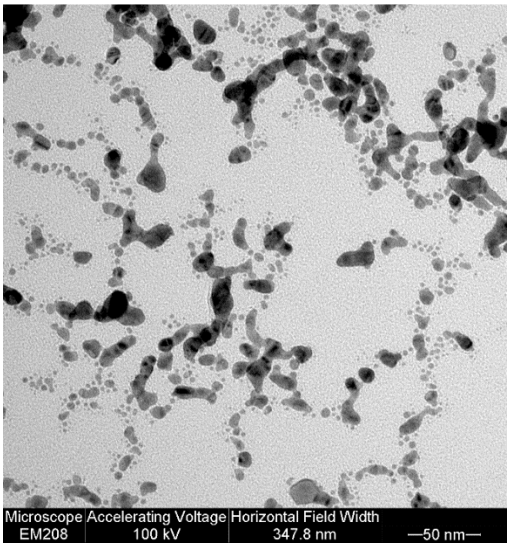

Figure 3.4. TEM micrograph of Cya-AuNPs prepared following the procedure reported by Feng *et al*.[104] The image shows a large extent of NP aggregation.

In literature,[105] only the synthesis of Cya-AuNPs with an average diameter of 30 nm is reported (Scheme 3.4).

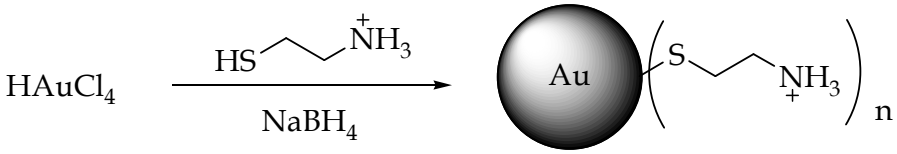

Scheme 3.4. Cya-AuNP direct synthesis.

That result was reproduced, though the obtained nanoparticles proved to have a polygonal shape (Figure 3.5 b). These Cya-AuNPs were stable for at least one month, but when they were mixed with the protein they suddenly precipitated into a black powder.

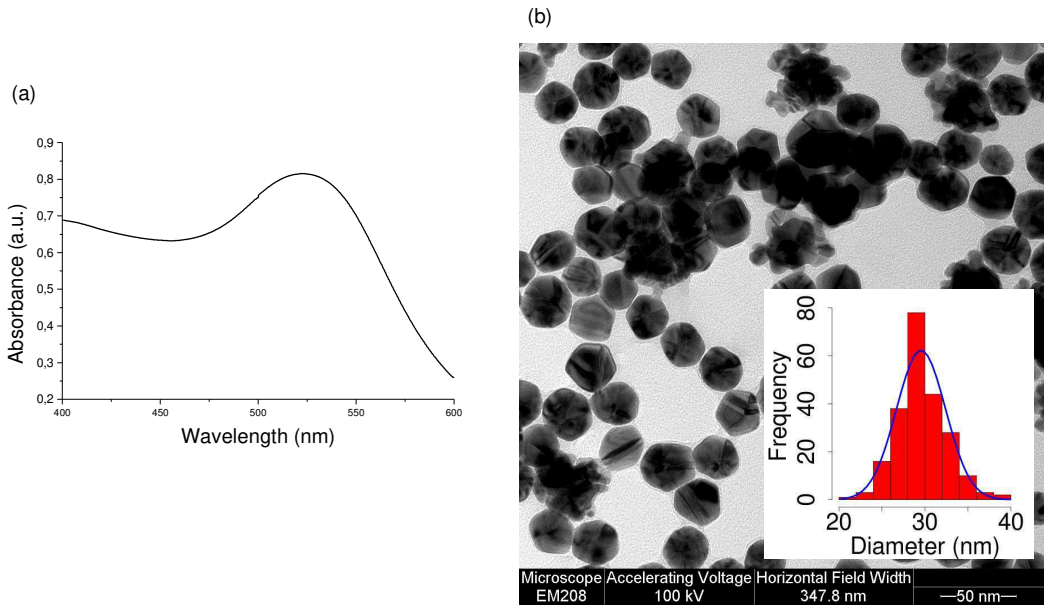

Figure 3.5. a) Absorption spectrum and b) TEM micrograph of Cya-AuNPs. The insert presents the size distribution histogram.

By varying the conditions (Cya/Au ratio and $NaBH_4$ amount) of the two procedures described above, it was not possible to prepare stable Cya-AuNPs with a diameter ranging from 5 nm to 10 nm. Therefore, cysteamine did not appear to be a proper stabilizing agent for AuNPs.

Even with longer positively charged thiols the exchange reaction proved to be hard to achieve, because the solution is destabilized by the interference of opposite charges which lead to detrimental repulsion.[106] By using 6-aminohexanethiol (AHT), it was possible to produce gold nanoparticles with a mixed monolayer through a two-step exchange.[102] First, the stability of Cit-AuNPs was increased by substituting citrate with thioctic acid (TA) that provides a double sulfide attachment. Then the positive charge was introduced by incubating TA-AuNPs with AHT (Figure 3.6 a). The exchange of the ligands can be followed by the shift of the SPR band (Figure 3.6 b).

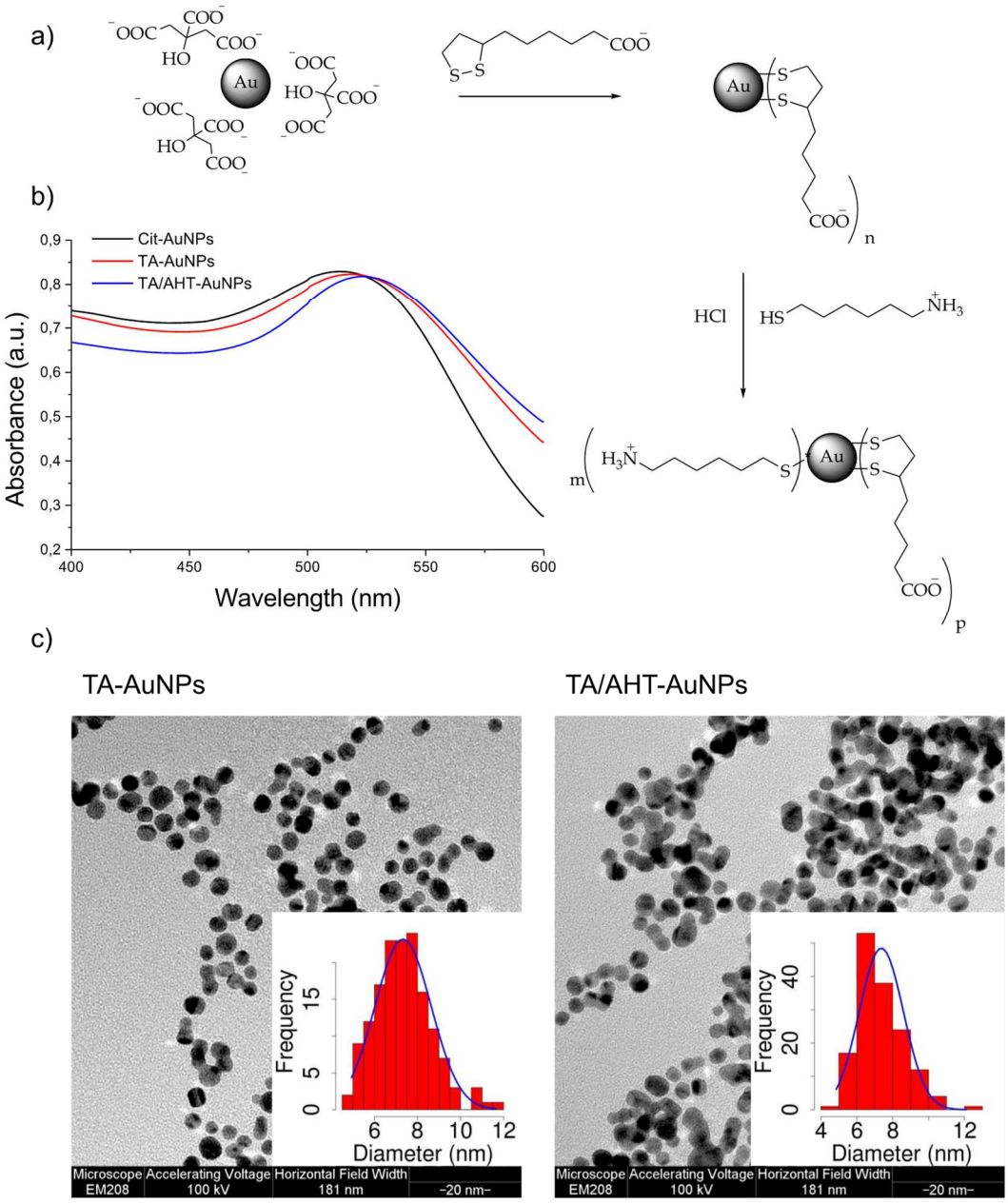

Figure 3.6. a) Scheme of TA/AHT-AuNP synthesis; b) UV-Vis spectrum of Cit-AuNPs (back line), TA-AuNPs (red line) and TA/AHT-AuNPs (blue line) and c) TEM micrographs and corresponding size distribution histograms of TA-AuNPs on the left and TA/AHT-AuNPs on the right.

The stability of gold nanoparticles covered by alkanethiolates ending with primary amines is highly pH dependent. Since the pK_a of amino groups bound to nanoparticles was found to be from 2 to 6 units lower than the solution values,[107] they are protonated only at very low pH values while at

physiological pH they are mainly uncharged leading to nanoparticle instability and consequent agglomeration. In particular, TA/AHT-AuNP were stable at pH around 2 that is incompatible with protein stability, as can be seen in Figure 3.7.

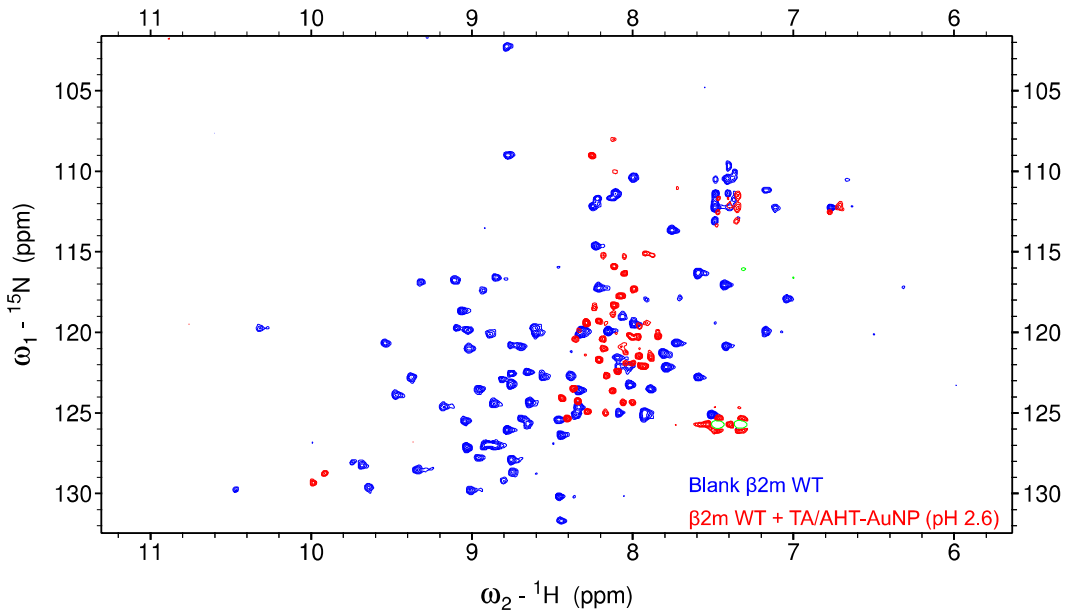

Figure 3.7. Superimposition of ^{15}N ^{1}H HSQC spectra of β2m WT in absence (blue) and in presence (red) of TA/AHT-AuNPs, pH 7 and 2.6, respectively. The red spectrum is typical of an unfolded protein.

To overcome this AuNP pH stability dependence, trimethylammonium terminated thiols were chosen for positively charged AuNP synthesis. Quaternary ammonium salts are permanently charged independently of the pH, supporting NP stability even under physiological conditions. As ligand, (11-mercaptoundecyl)-N,N,N-trimethylammonium bromide (MUTAB) was selected because it was the only one available on the market. To cationize Cit-AuNPs a reported procedure[108] that involves a two-step phase transfer was followed (Figure 3.8 a). First, Cit-AuNPs were transferred from water to an organic solvent by adding a neutral alkylamine. The amine substitutes citrate because of its stronger interaction with gold, but being neutral avoids detrimental electrostatic interactions between oppositely charged ligands which would lead to AuNP aggregation. Then, the AuNP coating was again

changed from the amine to the positively charged alkanethiol which forms stronger covalent bonds with Au and the NPs returned back to water.

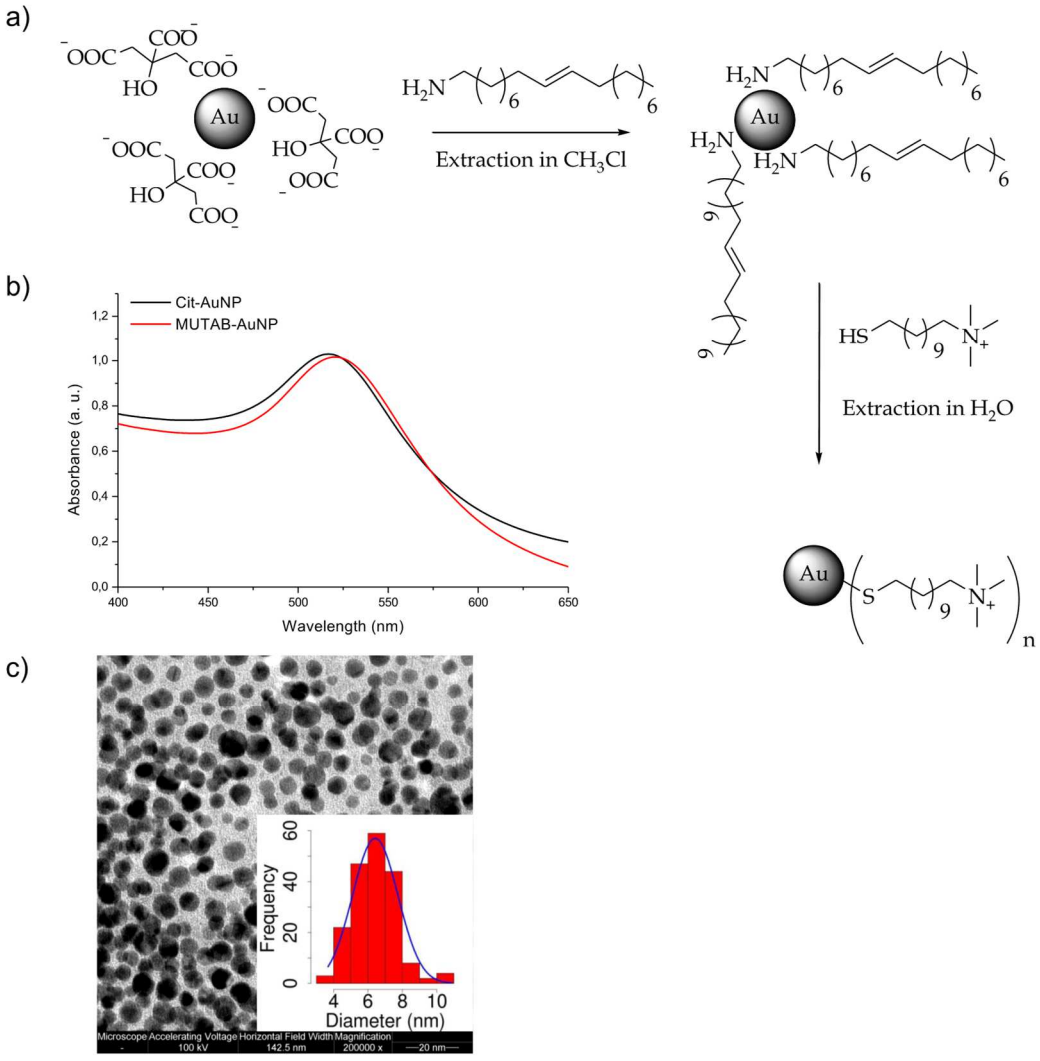

Figure 3.8. a) Scheme of MUTAB-AuNP synthesis; b) UV-Vis spectrum of Cit-AuNPs (back line) and MUTAB-AuNPs (red line) and c) TEM micrograph and corresponding size distribution histogram of MUTAB-AuNP.

Experimental section

All glassware used in nanoparticle synthesis was washed with *aqua regia* to remove metals which could reduce $HAuCl_4$ and dried in oven before use. Since the gold salt used as AuNP precursor is highly hygroscopic, it was weighted in a glove bag filled with nitrogen.

Synthesis of Cit-AuNPs

A solution of sodium citrate dihydrate (1.5 mM) and $HAuCl_4$ trihydrate (0.5 mM) in milliQ water was reduced under stirring at 0 °C by 1 mL of freshly prepared ice-cold $NaBH_4$ solution (0.1 M). The reduction of Au(III) to Au(0) and the consequent formation of the nanoparticles stabilized by the presence of citrate was assessed by the instantaneous colour change of the solution from pale yellow to ruby red after the addition of the reductant. The solution was allowed to reach room temperature under stirring and then was stored at 4 °C.

UV-Vis: ν_{max} = 518 nm.

TEM: d_{av} = 7.5 ± 1.0 nm.

Synthesis of MHA-AuNPs

A 10 mM solution of MHA was prepared in ethanol and 1 mL was added to 5 mL of Cit-AuNPs. The solution was stirred for 72 hours at room temperature. The solution became a little darker. These AuNPs could be two-fold concentrated by ultracentrifugation (MWCO = 10000) at 4000 rpm for 15 minutes. The integrity of the nanoparticles was assessed by UV-Vis.

UV-Vis: ν_{max} = 520 nm.

TEM: d_{av} = 7.4 ± 1.1 nm.

Synthesis of MPA-AuNPs

To a solution of $HAuCl_4 \cdot 3H_2O$ (49.2 mg, 0.125 mmol) in deoxygenated methanol (5 mL) cooled at 0 °C and purged with nitrogen, nine equivalents (65.3 μL) of 3-mercaptopropionic acid, dissolved in deoxygenated water (5

mL), were added under stirring. Upon the addition of the thiol the solution colour changed from yellow to cloudy white. After two hours of stirring, a freshly prepared cooled aqueous solution of $NaBH_4$ (1.25 mmol, 47.3 mg, in 2 mL of water) was dripped inside the gold/thiol solution. One hour later, the brown solution obtained was purified by centrifugation (5000 rpm, 15 minutes at 25 °C) repeating the removal of the supernatant and the dispersion in methanol five times.

UV-Vis: monotonic decay with a broad band from 450 to 550 nm.

TEM: d_{av} = 3.6 ± 1.3 nm.

Synthesis of Cya-AuNPs (1)

67.5 µL of 0.1 M $HAuCl_4 \cdot 3H_2O$, 427.5 µL of 0.1 M HCl and 37.5 µL of cysteamine hydrochloride were diluted in 30 mL of water and stirred at vortex for 10 minutes after which 300 µL of 0.1 M $NaBH_4$ were added. The solution was stirred at a lower speed for other 3 hours. The resulting solution was violet.

UV-Vis: monotonic decay with a broad band from 475 to 575 nm.

TEM: nanoparticle aggregates.

Synthesis of Cya-AuNPs (2)

15.8 mg of $HAuCl_4 \cdot 3H_2O$ were dissolved in 28.2 mL of water. After the addition of 284 µL of 213 mM cysteamine, the solution was stirred in dark for 20 minutes. The reduction of gold was achieved with 7.1 µL of $NaBH_4$ 10 mM. After 30 minutes stirring, the solution was stored in dark at 4 °C and used within one month.

UV-Vis: ν_{max} = 523 nm.

TEM: 29.5 ± 2.86 nm.

Synthesis of TA/AHT-AuNPs

A solution of 4 mL of Cit-AuNPs and 400 μL of TA 4 mM in ethanol was stirred overnight at room temperature.

UV-Vis: ν_{max} = 520 nm.

TEM: 7.3 ± 1.3 nm.

In an ice bath 400 μL of AHT 4 mM in ethanol were added to the NP solution. After one hour the solution became violet and suddenly after the addition of 400 μL of HCl 1 M it returned red. The exchange mixture was stirred overnight.

UV-Vis: ν_{max} = 523 nm.

TEM: 7.4 ± 1.2 nm.

Synthesis of MUTAB-AuNPs

5 mL of Cit-AuNPs were extracted with 2 mL of CH_3Cl in which 1.2 μL of oleylamine (OLAM) were dissolved. The nanoparticles were extracted to chloroform and backwashed three times with water to remove citrate. 330 μL of 4 mM MUTAB in ethanol and 500 μL of water were used to bring nanoparticles back to water. To remove OLAM, the aqueous solution was washed with the organic phase three times. These AuNPs could be twofold concentrated by ultracentrifugation (MWCO = 10000) at 4000 rpm for 15 minutes. The integrity of the nanoparticles was assessed by UV-Vis.

UV-Vis: ν_{max} = 521 nm.

TEM: 7.4 ± 1.2 nm.

3.2 AuNP-protein adduct characterization

To fully characterize the adduct made up by β2m and AuNPs, several different techniques were employed: dynamic light scattering (DLS), UV-Vis spectroscopy, transmission electron microscopy, fluorescence spectroscopy, nuclear magnetic resonance (NMR) and quartz crystal microbalance with dispersion monitoring (QCMD).

Dynamic light scattering

To determine the nanoparticle size in solution and if it changes upon protein addition, dynamic light scattering (DLS) was performed. β2m and nanoparticles were analysed first separately and then they were mixed in a ratio of 100/1.

A Horiba Particle Size Analyser LB-550 with a fixed scattering angle of 90° and a laser wavelength of 650 nm was employed for DLS measurements. The refractive index used was 0.34-3.200, as reported by the manufacturer of the instrument for gold. The samples were filtered with PVDF 0.2 μm filter and collected in disposable cuvettes of 4 mL with 10 mm optical path. At least 3 concordant measurements expressed in terms of scattering light intensity were recorded.

UV-Vis spectroscopy

Absorption spectra of AuNPs were recorded in the absence and in the presence of increasing amounts of protein. By following the progressive movement of the absorbance maximum it was possible to estimate the adsorption capacity of a single AuNP and by fitting the data with the Langmuir adsorption isotherm model (Equation 3.3) it was possible to estimate the binding constant:[37]

$$\Delta\lambda = \Delta\lambda_{max} \frac{K_a[\beta 2m]}{1 + K_a[\beta 2m]}$$

Equation 3.3

where $\Delta\lambda$ is the shift of the SPR band and K_a is the association constant. Each experiment was done in triplicate. A Jasco V-750 was used and the spectra were recorded at 20 °C, from 400 nm to 800 nm with a data pitch of 0.2 nm, a scan rate of 200 nm/min and a bandwidth of 2 nm.

Transmission electron microscopy

Transmission electron microscopy was used to assess the aggregating state of nanoparticles when they are incubated with β2m and to visualize the aspect of the samples by protein staining. To prepare the samples for the imaging, a small amount of the nanoparticle-β2m solution was dropped on a carbon TEM grid and left for 5 minutes. Filter paper was used to remove the excess of the solution. The solutions were stained with 2% uranyl acetate solution in water for 2 or 5 minutes. The size distribution was calculated by measuring a minimum of 200 particles using ImageJ software.

Fluorescence spectroscopy

The AuNP effect on tryptophan (Trp) fluorescence is a very convenient way to investigate their interaction with proteins bearing fluorescent Trp residues, in terms of binding affinity and Trp accessibility.[109] β2m intrinsic fluorescence is mainly due to a buried Trp residue, namely Trp95. The second Trp residue of the molecule, Trp60, contributes only marginally (20% approximatively) to the overall fluorescence because of its exposure on the protein surface and the consequent quenching effect of the solvent (Figure 3.9).[110]

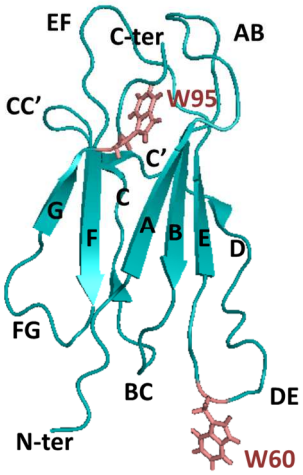

Figure 3.9. Cartoon of β2m structure showing the positions of Trp60 (W60) and Trp95 (W95) depicted in salmon pink. The β2m strand and loop naming is also indicated.

β2m intrinsic fluorescence was recorded in absence of AuNP and after the progressive addition of small amounts of nanoparticles using a Perkin Elmer LS-55 fluorimeter or a Cary Eclipse Fluorescence Spectrophotometer. For the measurement, fluorescence semi-micro cuvettes were used (5 mm x 5 mm). The samples were excited at 295 nm and the emission was recorded from 300 to 450 nm, using 5 nm slit for both excitation and emission. Each spectrum was the average of 5 consecutive measurements and three individual experiments were repeated for each sample. The measured fluorescence intensity (F_{meas}) was corrected for the inner filter effect using the following equation:[111]

$$F_{corr}=F_{meas}\ 10^{(A_{ex}+A_{em})/2}$$

Equation 3.4

where A_{ex} and A_{em} are the Cit-AuNP absorbances at excitation and emission frequencies, respectively.

Since Cit-AuNPs are able to quench completely β2m fluorescence and the quenching was found to be proportional to the NP concentration, the fluorescence data were fitted with the linear Stern-Volmer equation:[111]

$$\frac{F_0}{F} = 1 + K_{SV}[NP] = 1 + k_q \tau_0 [NP]$$

Equation 3.5

where F_0 and F are the fluorescence intensities of the protein in absence and in presence of Cit-AuNPs, respectively, and the Stern-Volmer constant, K_{SV}, is the product of the diffusion-limited bimolecular quenching constant, k_q, and the fluorophore fluorescence lifetime, τ_0. To estimate the order of magnitude of the binding constants, the Hill equation was applied.[23] The fluorescence quenching was expressed by the following relation:

$$Q = \frac{F_0 - F}{F_0}$$

Equation 3.6

The saturation value of Q is:

$$Q_{max} = \frac{F_0 - F_\infty}{F_0}$$

Equation 3.7

Since Cit-AuNPs are able to quench completely the protein fluorescence, F_∞ can be set to 0 and consequently $Q_{max} = 1$.[112] Following Lacerda *et al.*, Hill equation can be written as:[23]

$$\frac{Q}{Q_{max}} = \frac{[L]^n}{(K_d + [L]^n)}$$

Equation 3.8

where L stands for Cit-AuNP, K_d represents the apparent dissociation constant and n is the Hill coefficient, in this context related to the cooperativity of the binding. The standard error connected to the fit is expressed as $\sigma_i = (C_{ii}\,\chi^2)^{1/2}$ where C_{ii} is the diagonal element of the variance-covariance matrix and χ is the standard statistical correlation index.

Nuclear magnetic resonance

NMR experiments were performed on uniformly ^{15}N-labeled β2m dissolved in HEPES 50 mM pH 7. 5% of D_2O was added to each sample for lock purposes. The blank samples include the NP stabilizing agents i.e. citrate and/or alkanethiols.

Two-dimensional ^{15}N-^{1}H spectra

To probe protein structure perturbations and to identify protein perturbed patches in presence of nanoparticles, β2m ^{15}N-^{1}H HSQC[113] or SOFAST-HMQC[114] spectra were recorded in the absence and in the presence of AuNPs. The outcome of both kinds of two-dimensional experiments is the same, the only difference is that SOFAST experiments use an optimized pulse program sequence based on selective band excitation that allows recording of spectra in a faster way thereby improving signal to noise ratio per unit time.[115] These spectra present the H-N correlations of the backbone amides of each protein residue, along with the side chains of Asn, Gln and Trp. By analysing the changes in NMR signal characteristics i.e. chemical shift, intensity and (in principle) linewidth, it is possible to map the perturbations induced by NPs on the protein structure.

NMR experiments were collected on the Bruker Avance spectrometer at the Udine University Biophysics Laboratory, operating at 500 MHz (^{1}H) or, for the less concentrated samples, on the Bruker Avance III NMR spectrometer at the Core Technology Platform of New York University Abu Dhabi, operating at 600 MHz (^{1}H) and equipped with a cryoprobe.

2D ^{15}N-^{1}H spectra were recorded at 298 K over spectral widths of 30 ppm (^{15}N, t_1) and 14 ppm (^{1}H, t_2) with 128 and 1024 points, respectively. For each t_1 dimension point 32, 64 or 1600 scans were accumulated and quadrature in the same dimension was accomplished by gradient-assisted coherence selection (echo-antiecho).[116] Water suppression was achieved by using a flip-back pulse.[117] The data were processed with Topspin 2.1 or 3.5 and analysed with Sparky. The β2m assignment was based on the file deposited on the Biological Magnetic Resonance Data Bank (Accession Code: 17165). Chemical shift perturbations were calculated as $\Delta\delta$ (ppm) = $[(\Delta\delta_H)^2 + (\Delta\delta_N/6.5)^2]^{1/2}$ where $\Delta\delta_H$ and $\Delta\delta_N$ are the chemical shift variations for ^{1}H and ^{15}N, respectively,[118] and the relative intensities (RI) correspond to the ratio between the signal intensity in presence of NPs and in absence of NPs. The uncertainty related to the relative intensity ratio was calculated applying the propagation of the intensity error estimated from the signal-to-noise ratio.

Relaxation experiments

Protein dynamics in presence and in absence of Cit-AuNPs were analyzed by measuring ^{15}N longitudinal (R_1), transverse (R_2) and rotating frame ($R_{1\rho}$) relaxation rates, along with ^{1}H-^{15}N steady state Nuclear Overhauser Effect (NOE) values for 4 μM wild-type β2m samples.

Since molecular motions affect the two main mechanisms that drive relaxation processes for ^{1}H ^{15}N systems, namely dipole-dipole (DD) interactions and chemical shift anisotropy (CSA), any change in relaxation parameters is a probe of different internal motions.[119]

Relaxation rates describe the processes through which the populations of the nuclear magnetic dipole moment energy levels return to the equilibrium state after a perturbation. At the equilibrium, the magnetization is on the *z* axis. After the application of a suitable radiofrequency pulse, the magnetization in addition to a residual *z* component has a substantial component on the *xy* plane. The restoration of the *z*-magnetization

equilibrium through energy transfer between the spin system and the lattice is called longitudinal relaxation and occurs at rate R_1. The classical experiment to measure R_1 is the inversion recovery experiment which allows to measure the recovery of *z* magnetization after a pulse sequence made by a 180° pulse and a 90° pulse separated by a variable length relaxation delay.[120] Transverse relaxation describes the decay of magnetization in the *xy* plane by energy exchange within the spin system or with the lattice. The rate of the transverse magnetization loss, R_2, is determined through Carr-Purcell-Meiboom-Gill (CPMG) spin-echo pulse sequence.[121,122] CMPG experiments are made by a 90° pulse followed by a train of 180° pulse, each flanked by two equal variable delays. While R_1 is sensitive only to high frequency motions (picosecond to nanosecond range), R_2 provides also information about slower processes (micro-to-millisecond time scales) like some exchange processes.[123] Nuclear Overhauser Effect (NOE) is related to another relaxation process called cross-relaxation. It is based on the fact that the relaxation of a nucleus affects measurably the spin magnetization populations of adjacent nuclei, within a range of 0.5-0.6 nm. In particular, in steady-state heteronuclear ^{15}N $\{^1H\}$ NOE the change in ^{15}N signal is measured after the saturation of ^1H and compared with the intensity in the unsaturated spectrum. In this case the most relevant NOE arises from the perturbation of the dipolar interaction between nitrogen and the attached hydrogen nuclei separated by 0.11 nm. By measuring the relaxation rate in the rotating frame, $R_{1\rho}$, it is possible to estimate the R_2 exchange contributions (usually in the microsecond time scale). In rotating frame relaxation experiments the application of an additional magnetic field B_1 perpendicular to the external field B_0, causes the tilt of the effective magnetic field and the relaxation of a spin-locked magnetization in a tilted rotating frame is a function of the two different transverse relaxation contributions, i.e. the exchange-free and the one related to exchange.[124]

A detailed kinetic and thermodynamic description of μs to ms exchange processes is provided by relaxation dispersion experiments.[125] Exchange processes occurring on μs to ms time scale lead to a modulation of the chemical shift of the affected nuclei and to an increase in exchange contribution to the transverse relaxation rate and concurrent line-broadening.[126] Relaxation dispersion experiment is based on CPMG sequences and employs trains of 180° pulses with variable pulse spacing in a fixed time interval. This corresponds to a variation of the actual spin lock power. The fitting of the transverse relaxation rate as a function of the CMPG frequency allows the determination of the exchange rate constant (k_{ex}) of the relevant processes. Depending on the time scale of the exchange, also the populations of the two states involved in the exchange and their chemical shift difference (δ_ω) can be determined. By comparing k_{ex} and δ_ω values it is possible to define if the process is fast ($k_{ex} \gg \delta_\omega$), intermediate ($k_{ex} \approx \delta_\omega$) or slow ($k_{ex} \ll \delta_\omega$) on the NMR chemical shift time scale.

^{15}N longitudinal, transverse and rotating frame relaxation rates were extracted from experiments employing pulse sequences proposed by Kay and co-workers,[127] Stone and co-workers[120] and Dayie and Wagner,[128] respectively. ^{1}H-^{15}N steady state NOE experiments were performed following Kay and co-workers pulse sequence.[129] The saturated and unsaturated spectra were acquired in an interleaved manner. Two dimensional spectra were acquired over 64 x 1024 matrices of complex data points in t_1 and t_2 dimensions and with 96 scans per t_1 increment for relaxation rate measurements and over 56 x 2024 matrices and with 1536 scans for ^{1}H-^{15}N NOE experiments. In all cases a recovery time of 3 s was used. Eleven relaxation delays ranging from 20 to 1500 ms, ten delays from 16.9 to 203 ms and ten delays from 8 to 184 ms were used for R_1, R_2 and $R_{1\rho}$ experiments, respectively. In each series three repetitions were carried out to estimate the relaxation rate errors. A ^{15}N spin-lock continuous wave radiofrequency irradiation of 2.1 kHz was employed to perform rotating

frame relaxation experiments. The data were analyzed using Dynamics Center software by fitting peak intensities at different mixing times with the following exponential decay function

$$I(t) = I_0\, e^{-t/T}$$

Equation 3.9

where $I(t)$ is the peak intensity measured at the mixing time t, I_0 is the intensity at t = 0 and T is the decay time constant that is the inverse of the relaxation rate. As an example, the R_1 relaxation fitting curves for residue Asp98 in presence and in absence of Cit-AuNPs are reported in the figure below (Figure 3.10).

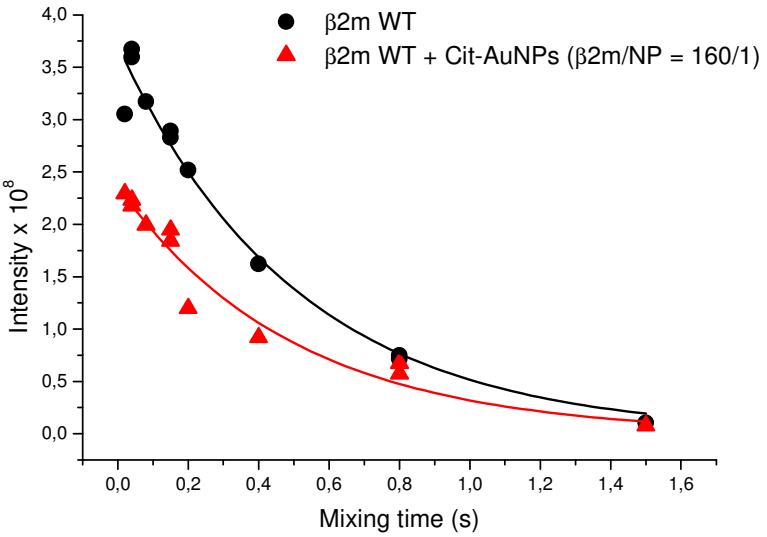

Figure 3.10. R_1 relaxation decay curves for Asp98 in presence (red) and in absence (black) of Cit-AuNPs.

Relaxation dispersion experiments were performed following the pulse sequence proposed by Tollinger *et al.*[130] A series of 12 2D data sets was collected with different CPMG field strengths corresponding to pulse application frequency (ν_{CP}) of 25, 50 (x3), 100, 250, 500 (x3), 750, 1000 Hz. By setting ν_{CP} to 0, the CPMG train was omitted in the pulse sequence and it was possible to obtain the reference spectrum. Each 2D spectrum was

recorded as a complex data matrix of 1kx64 points. 240 scans per FID were acquired. Data were processed with Topspin 3.2 and analyzed with the Rex module of Dynamics Center. Dynamics Center uses two different equations for the fitting. The first refers to the slow exchange limit:[130]

$$R(\tau_{CP}) = R_2 + k_{ex} - k_{ex}\frac{\sin(\delta_\omega \tau_{CP})}{\delta_\omega \tau_{CP}}$$

Equation 3.10

where R_2 is the transverse relaxation rate, k_{ex} is the exchange constant, δ_ω is the chemical shift difference between the two exchanging states and τ_{CP} is the time between the 180° pulses.

The second equation used by Dynamics Center to fit relaxation dispersion data refers to the fast exchange limit:[131]

$$R(\tau_{CP}) = \frac{p_A p_B \delta_\omega}{k_{ex}}\left[1 - \frac{2\tanh(k_{ex}\tau_{CP}/2)}{k_{ex}\tau_{CP}}\right]$$

Equation 3.11

where p_A and p_B are the fractional populations of the two exchanging states.

The evolution of the transverse magnetization of the protein in its free and NP-bound state can be described by dark state exchange saturation transfer (DEST).[132] When the protein is bound to the surface of large supramolecular structures, its transverse relaxation rate is very fast and consequently its NMR signal becomes very broad. This broadness, while preventing the direct observation of the bound species, allows their partial saturation without affecting the free species by applying weak radiofrequency fields at large offsets. When the molecules return in solution under the effect of the chemical exchange, they transfer the saturation to the free species leading to the attenuation of the cross-peaks in the NMR spectrum of the visible species. The R_2 variation and the relative intensity recorded as a function of the frequency offsets give information about the global dynamics and the exchange kinetics. However, to interpret properly

DEST data specific exchange models must be considered and *ad hoc* functions must be used for the fitting.

The sequence used to measure longitudinal relaxation rate was edited in order to add the DEST nitrogen saturation period. DEST measurements were performed employing a 0.6-0.8 kHz continuous wave radiofrequency for saturation at offsets from the carrier frequency going from -20 to -1 kHz. Series of 2D spectra were recorded in an interleaved manner, but very low quality spectra were obtained. Considering that the DEST experiment is really demanding both from an acquisition and an analysis point of view, it was decided to abandon this approach.

Diffusion ordered spectroscopy (DOSY) experiments

Diffusion coefficients were determined by means of 2D 1H DSTEBPP (Double Stimulated Echo BiPolar Pulse) experiments.[133] Protein concentration was 4 μM in 50 mM HEPES, pH = 7 in 95/5 H_2O/D_2O, either in absence and in presence of Cit-AuNPs. The z-axis gradient strength was varied with a squared increment ramp from 10 to 90 % of its maximum value (~ 60 G/cm) and matrices of 2048 by 40 points were collected by accumulating 512 scans per gradient increment. Water suppression was carefully adjusted by appending to the DSTEBPP sequence a pair of WATERGATE[134] elements in the excitation-sculpting mode.[135] The acquired data were processed using the Bruker software Dynamics Centre to extract the diffusion coefficients.

Quartz crystal microbalance with dissipation monitoring (QCMD)

A solution of 1 μM D76N β2m without or with 25 nM Cit-AuNPs and a solution of 25 nM Cit-AuNPs were flowed over an Au-coated QCMD sensor (Qsense-analyzer from Biolin Scientific) at the rate of 50 μL/min for 5000 seconds, approximately, after which a rinsing step with the buffer was accomplished.

Frequency changes (Δf) plots as a function of time were recorded. Data were analysed by Sauerbrey equation that establishes a direct proportionality between the experimental Δf and the mass density difference adsorbed on the sensor in ng/cm^2 (Δm):[48]

$$\Delta f = -nC\Delta m$$

Equation 3.12

where n is the vibrational overtone considered (the fifth) and C is a constant that depends on instrument characteristics (17.8 ng cm^{-2} Hz^{-1}).

The adsorption kinetic was analysed by Boltzmann fitting:

$$\Delta f = \frac{A_1 - A_2}{1 + e^{(t-t_0)dt}} + A_2$$

Equation 3.13

where A_1 and A_2 are initial and final asymptotes, respectively, t_0 is the sigmoid centre and dt is the time constant of the absorption process. A first attempt with exponential decay fitting was done, but the data coming from the protein alone adsorption could not be fitted.

The energy dissipation recorded during the absorption reflects the stiffness of the material that contacts the gold surface. To better compare the relative flexibility of the protein adsorbed layers in presence and in absence of Cit-AuNPs, the observed changes in dissipation (ΔD) were plotted as a function of Δf (D-f plots).[136,137]

3.3 Analysis of protein fibrillation in presence of Cit-AuNPs

Since wild-type and ΔN6 β2m fibrillate *in vitro* only under acidic conditions that are incompatible with AuNP stability, the more amyloidogenic D76N variant was used. In this mutant Asp76 is replaced by an Asn leading to a higher propensity towards fibrillation even if the global protein structure is maintained. The fibril formation was followed by different methods: thioflavin T (ThT) assay, TEM and soluble fraction analysis. This experiment was done only with Cit-AuNPs because AT-AuNPs revealed to be unstable in presence of the protein.

D76N β2m fibril formation

A solution of D76N β2m (2 mg/mL) in 50 mM HEPES pH 7 was centrifuged (14000 rpm, 10 minutes). The supernatant was collected as much as possible without the pellet and filtered with a filter of 0.22 μm. After the concentration measurement, the solution was diluted to 20 μM either with buffer containing 1.5 mM sodium citrate or with Cit-AuNP buffered solution. Sodium azide (1‰) was added as preservative. The solutions were incubated at 37 °C under vigorous stirring. Aliquots were taken at different time points to perform fibrillation analysis. The experiments were done in triplicate.

Thioflavin T assay

Thioflavin T is a dye whose fluorescence sharply increases upon binding with highly ordered amyloid structures and this fluorescence intensity is proportional to the fibril concentration.[67] A 10 μM ThT solution in 50 mM glycine buffer at pH 8.3 was prepared. 495 μL of this solution were added to 5 μL of the samples collected during the fibrillation and fluorescence was

recorded at 480 nm, after excitation at 445 nm on a Perkin Elmer EnSpire 2300 fluorimeter.

Transmission electron microscopy imaging of fibrils

Some drops of the solutions incubated under fibrillogenic conditions were deposited on a TEM grid and after 5 minutes the excess was soaked up with filter paper. The preparations were stained with some drops of 2% uranyl acetate solution in water for 2 or 5 minutes, the remaining solution was removed with filter paper and the grid was washed with water and dried for 10 minutes. The samples were observed using Philips EM 208 or Joel 1200EX transmission electron microscopes.

Native agarose gel electrophoresis

An aliquot of 10 μL of D76N β2m solution incubated under fibrillogenic conditions was centrifuged at 14000 rpm for 10 minutes. The supernatant was collected and frozen. The sample was loaded onto 1% agarose gel and the protein was stained with Coomassie Blue. The analysis of the gels were performed using ImageJ software.

4 RESULTS AND DISCUSSION

4.1 Cit-AuNP adduct formation with WT, ΔN6 and D76N β2m variants

The interaction between Cit-AuNPs and β2m was characterized using different complementary techniques. Along with the wild-type, also two more amyloidogenic variants, namely ΔN6 and D76N, were analysed.

4.1.1 Assessment of β2m adsorption on Cit-AuNPs

To prove the adsorption of β2m on synthesized Cit-AuNPs (see Section 3.1) DLS experiments were performed. The hydrodynamic diameter of Cit-AuNP was found to be 10.5 ± 2.0 nm (Figure 4.1), a value larger than the one showed by TEM (7.5 ± 1.0 nm). This difference can be explained considering that DLS is able to detect also the citrate layer (approximatively 1 nm thick[138]) and the hydration shell that are not accounted in TEM. Furthermore, DLS size distribution is weighted for the scattered light intensity which is proportional to the sixth power of particle diameter, meaning that a small fraction of larger particles that scatter more can dominate. Also β2m alone was tested giving a value of 6.3 ± 0.3 nm at a concentration of 20 μM (Figure 4.1). β2m is a globular protein whose three-dimensional structure can be assimilated to a cylindroid with longitudinal and transverse axes of 4.3-3.8 and 2.5-2.0 nm, respectively.[139] In the case of non-spherical objects like β2m, DLS results should be taken with proper care because DLS gives the diameter of a sphere that has the same average translational diffusion coefficient as the particle being measured. The discrepancy between crystallographic dimensions and hydrodynamic diameter could be also attributed to the presence of dimers or larger oligomers in solution. The occurrence of higher molecular weight species in equilibrium with β2m

monomers has been repeatedly observed in solution.[140,141] After the incubation with β2m, the hydrodynamic size of nanoparticles increased from 10.5 nm to 24.5 ± 6.1 nm (Figure 4.1). This increase is consistent with the formation of a single layer of adsorbed proteins around the gold core. The NP-protein adduct size emerging from DLS, however, is not necessarily a static one as the time scale that is probed by DLS is at least three orders of magnitude smaller than the one accessible by other techniques like NMR or time-resolved fluorescence. In addition, since DLS is an intensity-weighted technique, it accentuates the presence of larger objects even if they are low concentrated.

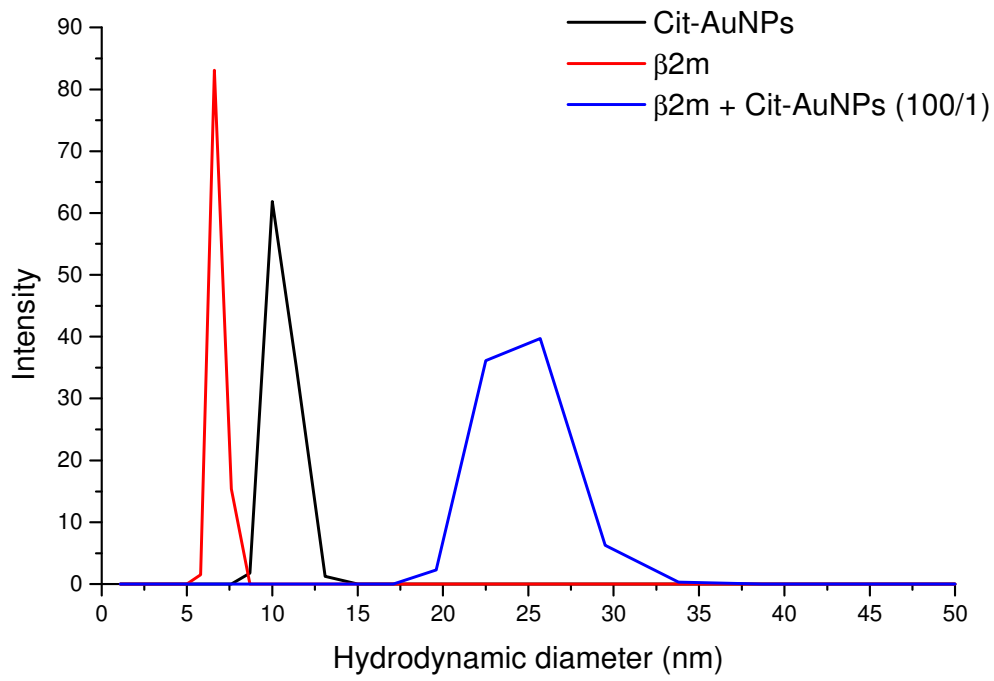

Figure 4.1. Size distribution of Cit-AuNPs (black), β2m (red) and their mixture (blue) obtained by DLS.

Through simple geometrical calculations, it is possible to estimate the number of proteins that can be adsorbed on the surface of a single nanoparticle. If the ratio between the volumes is considered as proposed by

Calzolai *et al.*,[38] it is possible to obtain the number of proteins (N) from this equation (Equation 4.1)

$$N = 0.65 \times \frac{(R_{complex}^3 - R_{NP}^3)}{R_{protein}^3}$$

Equation 4.1

where $R_{complex}$ is given by the sum of the NP radius and the diameter of β2m, R_{NP} is the radius of the nanoparticle and $R_{protein}$ is the radius of β2m. Using the hydrodynamic diameters of Cit-AuNPs and β2m obtained from DLS, a maximum number of 30 proteins per NP was calculated. If the ratio between the surface area of Cit-AuNP spheres and that of a circle with the same diameter of β2m is considered, the number of proteins per NP drops down to 11. However, for the reasons stated before, DLS size measurement is not reliable especially with polydisperse and not spherical molecules.

Considering the crystallographic cylindrical shape of β2m, the previous equation (Equation 4.1) becomes

$$N = 0.65 \times \frac{\frac{4}{3}(R_{complex}^3 - R_{NP}^3)}{h_{cyl} \times r_{cyl}^2}$$

Equation 4.2

where $R_{complex}$ is given by the sum of the NP radius and the height of the β2m cylindroid, R_{NP} is the radius of the nanoparticle and h_{cyl} and r_{cyl} are the height and the base radius of β2m cylindroid. Following this equation, a spherical Cit-AuNP with an average diameter of 7.5 nm, as indicated by TEM, can accommodate 55-95 β2m monomers. This estimation uses the maximum packing density factor possible for spherical proteins. Since the β2m cylindroid base dimension is a half with respect to height, considering symmetric tetramers instead of cylindroids can improve the geometrical model, leading to 15-30 tetramers per NP that means 60-120 monomers. Both spherical and tetrameric volume-based packing densities, however, appear unrealistic. Instead, the number of protein monomers per NP is reduced to 45-56 if the ratio of Cit-AuNP surface area and protein cylindroid base is

considered.[142] From all these considerations, beyond any critical evaluation, the number of β2m molecules that can be adsorbed on a Cit-AuNP goes from 50 to 100, approximately.

Another preliminary assessment of β2m adsorption on Cit-AuNPs was the red shift of the SPR band in the UV-Vis spectrum of the nanoparticles from 518 nm to 525 nm (Figure 4.2).

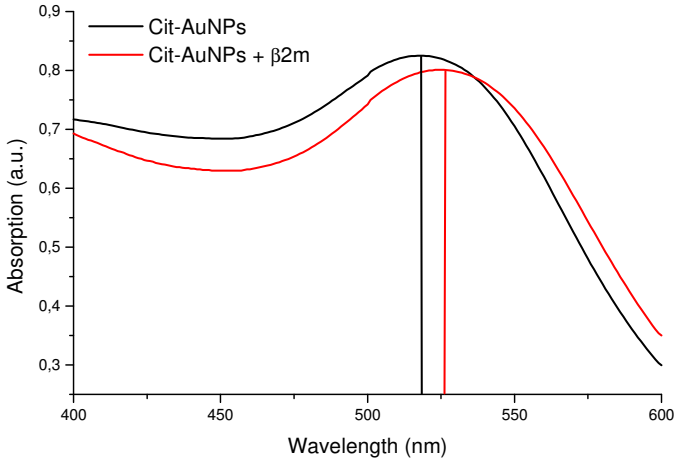

Figure 4.2. Absorption spectra of Cit-AuNPs alone (black line) and of Cit-AuNPs with 20 μM β2m (red line). The black and red vertical lines show the position of the absorbance maximum. The different intensity is due to NP dilution (by ~ 0.85).

This shift could be attributed mainly to two phenomena: the interaction with the protein that changes the dielectric environment felt by the NP plasmons and the aggregation of the NP induced by the presence of the protein.[25] From TEM images of the AuNPs incubated with β2m (Figure 4.3), an increase of the aggregation propensity does not appear to occur ruling out the second hypothesis.

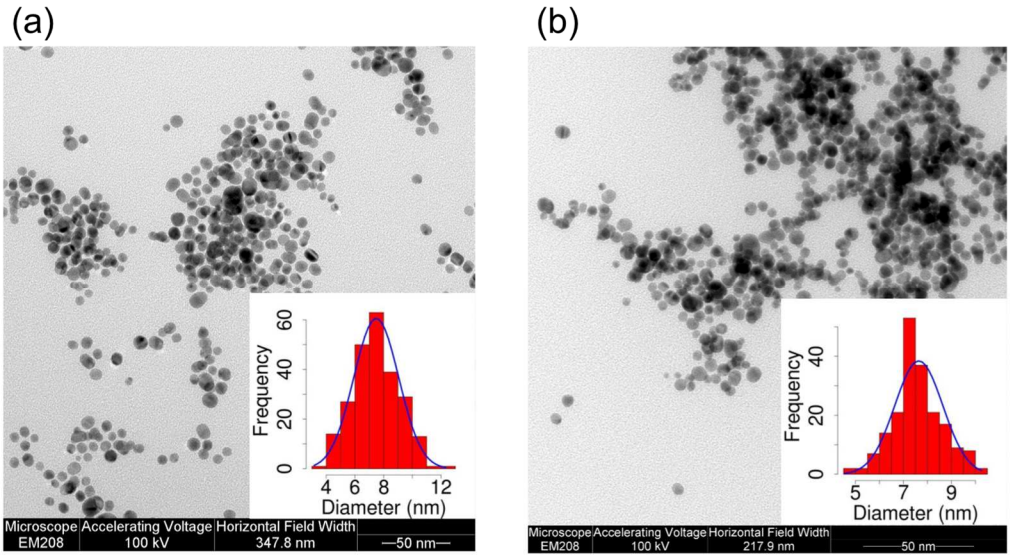

Figure 4.3. TEM micrographs of synthesized Cit-AuNPs a) alone and b) incubated with 20 μM β2m, along with the corresponding size histograms shown in the insets. The size distribution in presence of β2m rules out a possible protein-induced aggregation.

Furthermore, TEM carried on samples treated with protein staining revealed that nanoparticles are trapped in a protein network that surrounds them (Figure 4.4).

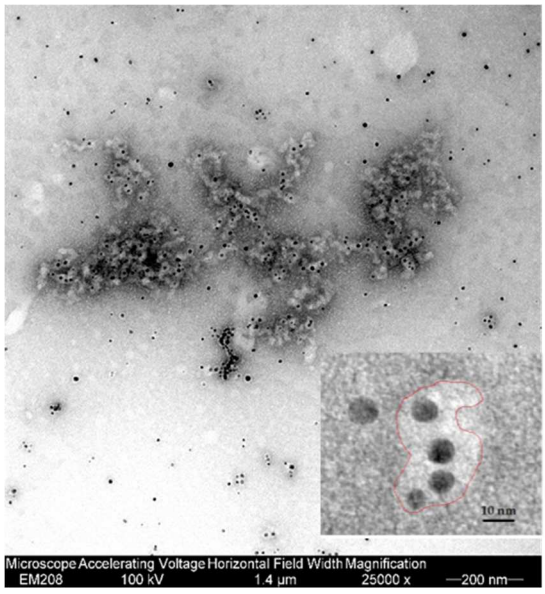

Figure 4.4. TEM micrograph of stained AuNP (20 nM) with 20 μM β2m: black dots are the nanoparticles and the white halo around them is the protein surrounded by the grey stain ring. The inset shows a magnification of some nanoparticles enclosed in a protein matrix with a red-highlighted halo.

4.1.2 Mapping the interaction of β2m variants with Cit-AuNPs

To discover which regions of the proteins, i.e. wild-type, D76N and ΔN6 β2m, are more involved in the interaction with Cit-AuNPs and/or undergo conformational rearrangements, two-dimensional ^{15}N-^{1}H HSQC NMR experiments were performed.

Two series of NMR spectra were recorded for the three β2m variants: one at a protein/NP ratio of 680 and one at 160.

As far as the higher protein/NP ratio is concerned, spectra were recorded on freshly prepared solutions and after one month.

For the wild-type no much relevant chemical shift variation (Δδ) in presence of Cit-AuNPs was found at both recording times (chemical shift variations were comparable with the chemical shift experimental uncertainty coming from spectra digitalization that is $\pm 9.8\times10^{-3}$ ppm[118]) but an unevenly distributed intensity attenuation was observed with an average relative intensity (RI_{av}) of 0.79 ± 0.057 soon after the preparation and of 0.76 ± 0.075 after one month (Figure 4.5 and 4.6).

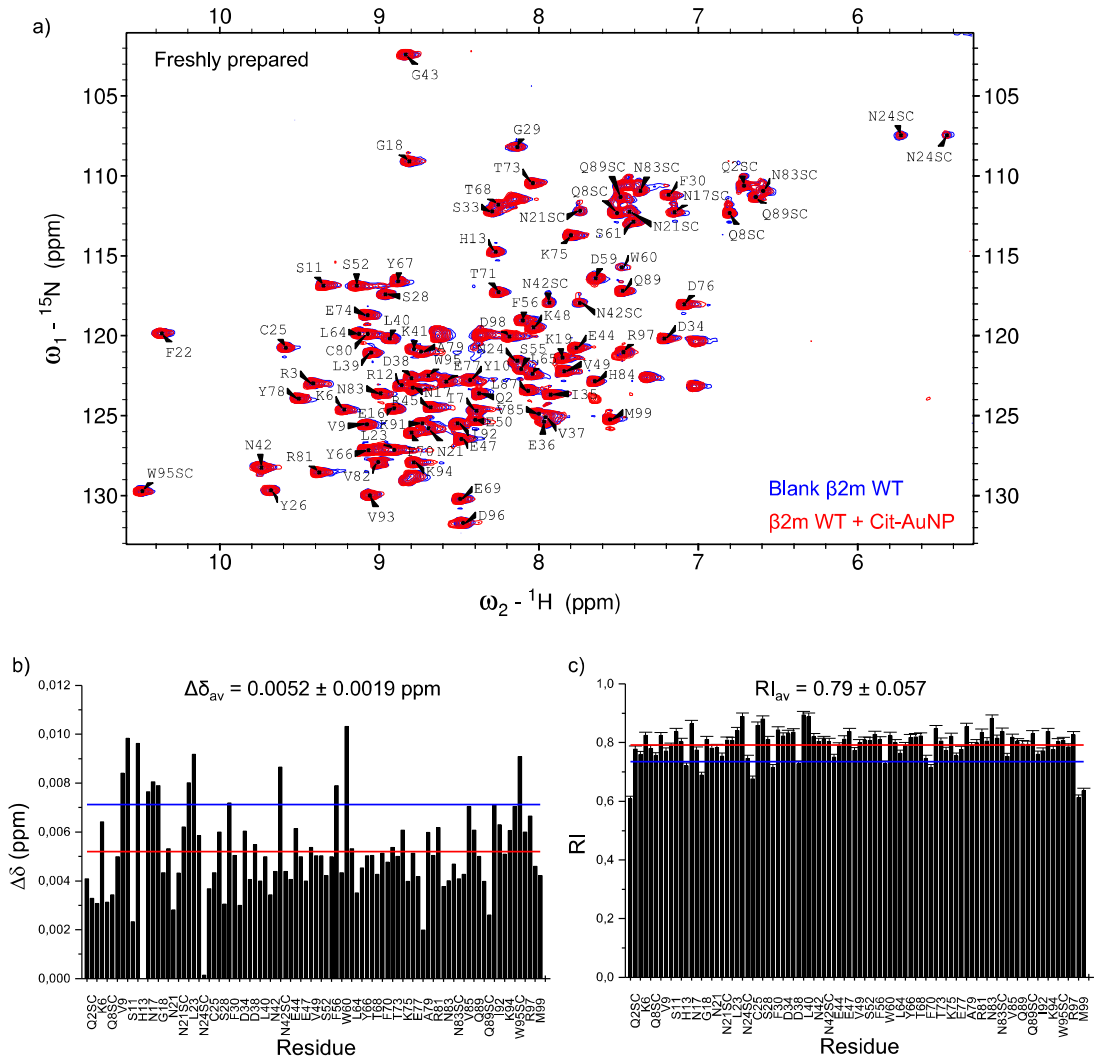

Figure 4.5. a) Superimposition of β2m WT ^{15}N-^{1}H HSQC spectra recorded at 500 MHz on the freshly prepared solution without (blue) and with (red) Cit-AuNP (protein/NP = 608). The corresponding backbone amide assignments are reported by single letter code and side chain amides are indicated with SC. b) and c) Bar plots of amide chemical shift perturbations (Δδ) and cross-peak attenuations (RI), respectively. The two horizontal lines indicate the average values (red) and the displacement of one standard deviation (blue) above and below the average, respectively. To avoid graphic crowding, the abscissa labels of both panels were reported only every other two signals. Besides the observed backbone amides, also the following detected side-chain (SC) NH resonances were included in the abscissa label list, according to the primary sequence order: Q2, Q8*, N17, N21*, N24*, N42*, N83*, Q89*, W95, where the asterisk indicates the inclusion of two separate resonances for asparagine and glutamine side-chain amides. The missing labels do not include the following unobserved or non-existing backbone NH connectivities: I1, T4, P5, Q8, P14, A15, S20, V27, H31, P32, H51, D53, L54, S57, K58, F62, Y63, P72, T86, S88, P90.

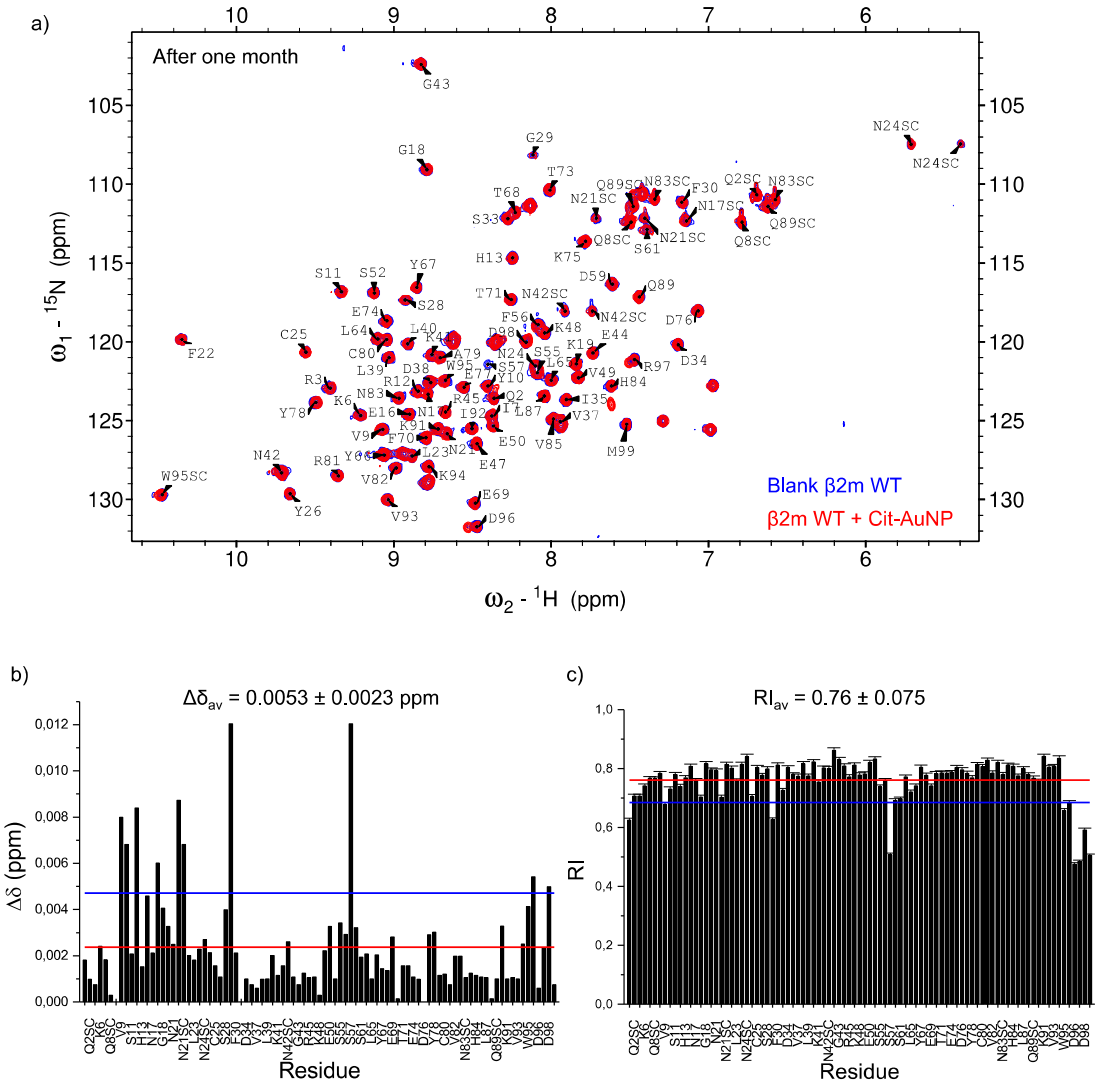

Figure 4.6. a) Superimposition of β2m WT ^{15}N-^{1}H HSQC spectra recorded at 500 MHz after one month without (blue) and with (red) Cit-AuNP (protein/NP = 608). The corresponding backbone amide assignments are reported by single letter code and side chain amides are indicated with SC. b) and c) Bar plots of amide chemical shift perturbations (Δδ) and cross-peak attenuations (RI), respectively. The two horizontal lines indicate the average values (red) and the displacement of one standard deviation (blue) above and below the average, respectively. To avoid graphic crowding, the abscissa labels of both panels were reported only every other two signals. Besides the observed backbone amides, also the following detected side-chain (SC) NH resonances were included in the abscissa label list, according to the primary sequence order: Q2, Q8*, N17, N21*, N24*, N42*, N83*, Q89*, W95, where the asterisk indicates the inclusion of two separate resonances for asparagine and glutamine side-chain amides. The missing labels do not include the following unobserved or non-existing backbone NH connectivities: I1, T4, P5, Q8, P14, A15, S20, V27, H31, P32, E36, H51, D53, L54, S57, K58, W60, F62, Y63, P72, T86, S88, P90.

Since the intensity attenuation was not uniformly distributed over the polypeptide sequence, it was not a consequence of protein precipitation induced by the nanoparticles. Moreover, the effect that we observed on the spectrum can not be attributed to a hard corona of proteins strongly and irreversibly bound to the nanoparticles. If a hard corona exists it could not be detectable due to the very low tumbling rate of the large complex which broadens the signal leading to its loss. However, considering that the protein was always in large excess with respect to the NP, the intensity decrease due to the disappearance of the hard-corona-forming proteins should be hardly appreciable. If we assume that 50-100 proteins can cover the NP surface, 7-15% of the total amount of protein should be involved in the hard corona formation leading to signal intensity loss. Since the average relative intensities are 0.79 and 0.76 in the first and second recording, respectively, the perturbations of the spectra collected in presence of Cit-AuNPs arose from the bulk protein that was involved in a reversible exchange process between a free and a transiently adsorbed state. The latter adsorption process could either involve the bare NP surface or the NP surface covered by a protein hard corona. In the first case, the effects of direct protein-NP interaction would have been observed, whereas in the alternative process the protein-protein interactions would have been responsible for the spectral feature perturbations.

All in all, the unevenly distributed intensity decrease came from the significant broadening of some signals belonging to residues whose transverse spin relaxation rate (R_2) was particularly affected by the interaction with the nanoparticles which induced changes to the local spectral density terms, in addition to the transient overall protein dynamics. The more attenuated peaks are reported in the table in Figure 4.7 along with their secondary and three-dimensional structure locations.

a)

Structure region	RI outliers t = 0	RI outliers t = one month
N-term, A strand	Q2	Q2, V9
AB loop	H13, N17SC	
B strand	N24SC	
BC loop	G29	G29
CC', C'D loops		
D strand		
DE loop	S55	S57
E strand	T68	
EF loop		
F strand		
FG loop		
G strand, C-term	D96, R97, D98, M99	W95, D96, R97, D98, M99

b)

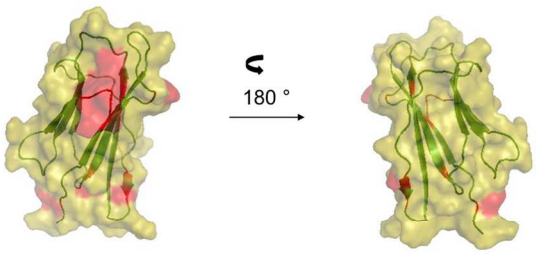

Figure 4.7. a) Synopsis of β2m WT positions that proved most affected, i.e. displaced more than one standard deviation from the average, by the presence of Cit-AuNPs and their secondary structure element location when protein/NP = 608. b) β2m WT cartoon highlighting in red the locations of the residues reported in a).

From these data, it was inferred that the most perturbed surface patch was localized at the exposed apical parts around both the N-terminal and the C-terminal fragments. The perturbation of the C-terminal segment was even more accentuated after one month when the intensity attenuation increased and the splitting of D96 and R97 peaks, that was only faint in the initial spectrum, became more evident. Furthermore, in the spectra recorded in presence of Cit-AuNPs a new signal appeared at 124 and 7.65 ppm, and in the one month aged sample also at 123 and 8.35 ppm between Y10 and Q2 peaks. The splitting and the appearance of new peaks might indicate that the nanoparticles were able to induce the formation of a different non-native local conformation or that some unfavourable local exchange dynamics preventing specific signal observation was removed by nanoparticle interaction. These possible explanations were no further investigated for the low sample concentrations.

The same kind and extent of spectral perturbations found for WT were observed also for D76N in the first recording (Figure 4.8), with an average

relative intensity of 0.80 ± 0.048 and an average chemical shift perturbation lower than 9.8×10^{-3} ppm.

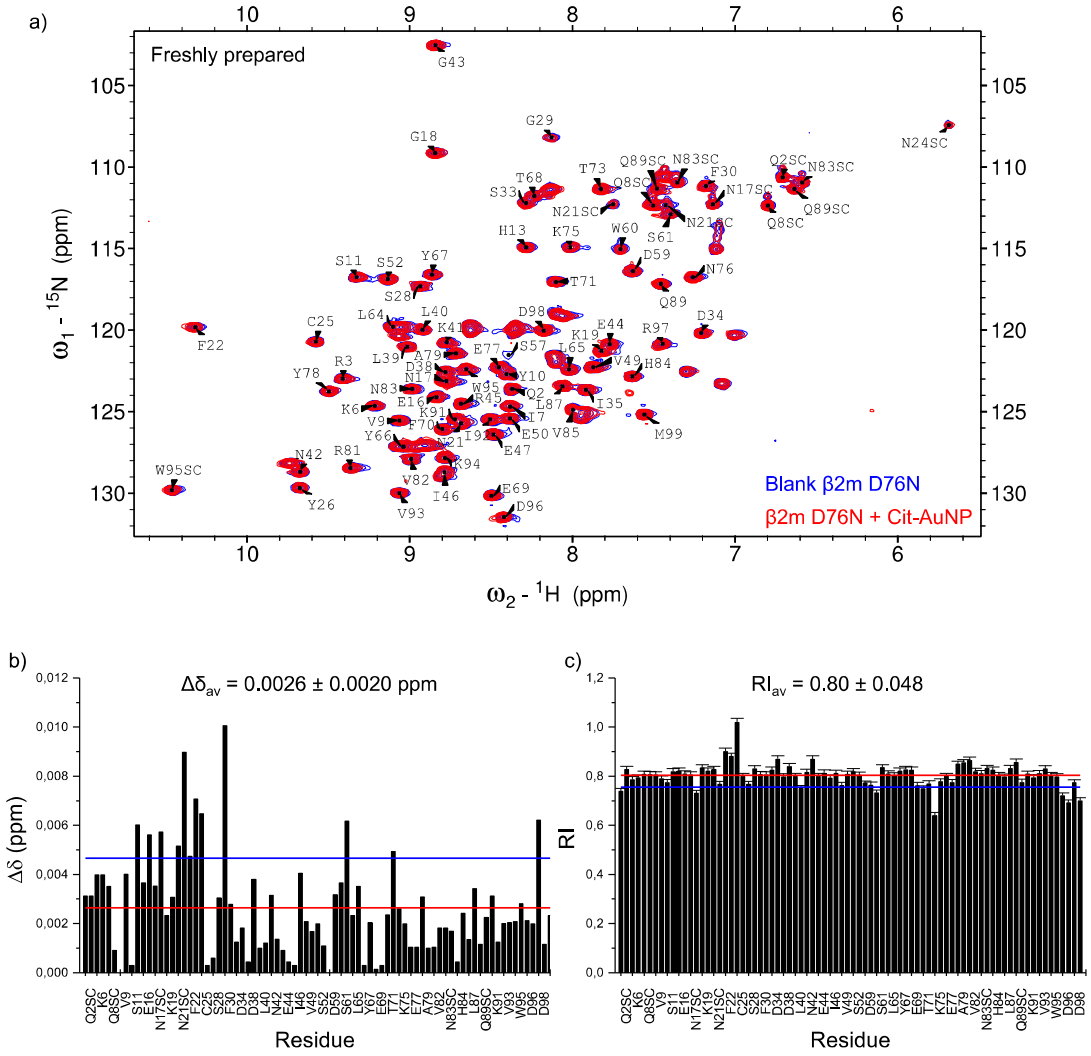

Figure 4.8. a) Superimposition of β2m D76N ^{15}N-^{1}H HSQC spectra recorded at 500 MHz on freshly prepared solutions without (blue) and with (red) Cit-AuNP (protein/NP = 608). The corresponding backbone amide assignments are reported by single letter code and side chain amides are indicated with SC. b) and c) Bar plots of amide chemical shift perturbations (Δδ) and cross-peak attenuations (RI), respectively. The two horizontal lines indicate the average values (red) and the displacement of one standard deviation (blue) above and below the average, respectively. To avoid graphic crowding, the abscissa labels of both panels were reported only every other two signals. Besides the observed backbone amides, also the following detected side-chain (SC) NH resonances were included in the abscissa label list, according to the primary sequence order: Q2, Q8*, N17, N21*, N24*, N42*, N83*, Q89*, W95, where the asterisk indicates the inclusion of two separate resonances for asparagine and glutamine side-chain amides. The missing labels do not include the following unobserved or non-existing backbone NH connectivities:

I1, T4, P5, Q8, R12, P14, A15, S20, L23, N24, V27, H31, P32, E36, V37, H51, D53, L54, F56, S57, K58, F62, Y63, P72, E74, C80, T86, S88, P90.

After one month, some peaks, namely F22, S57, N17, E16 and R97, started to move presenting a $\Delta\delta \geq 0.1$ (Figure 4.9).

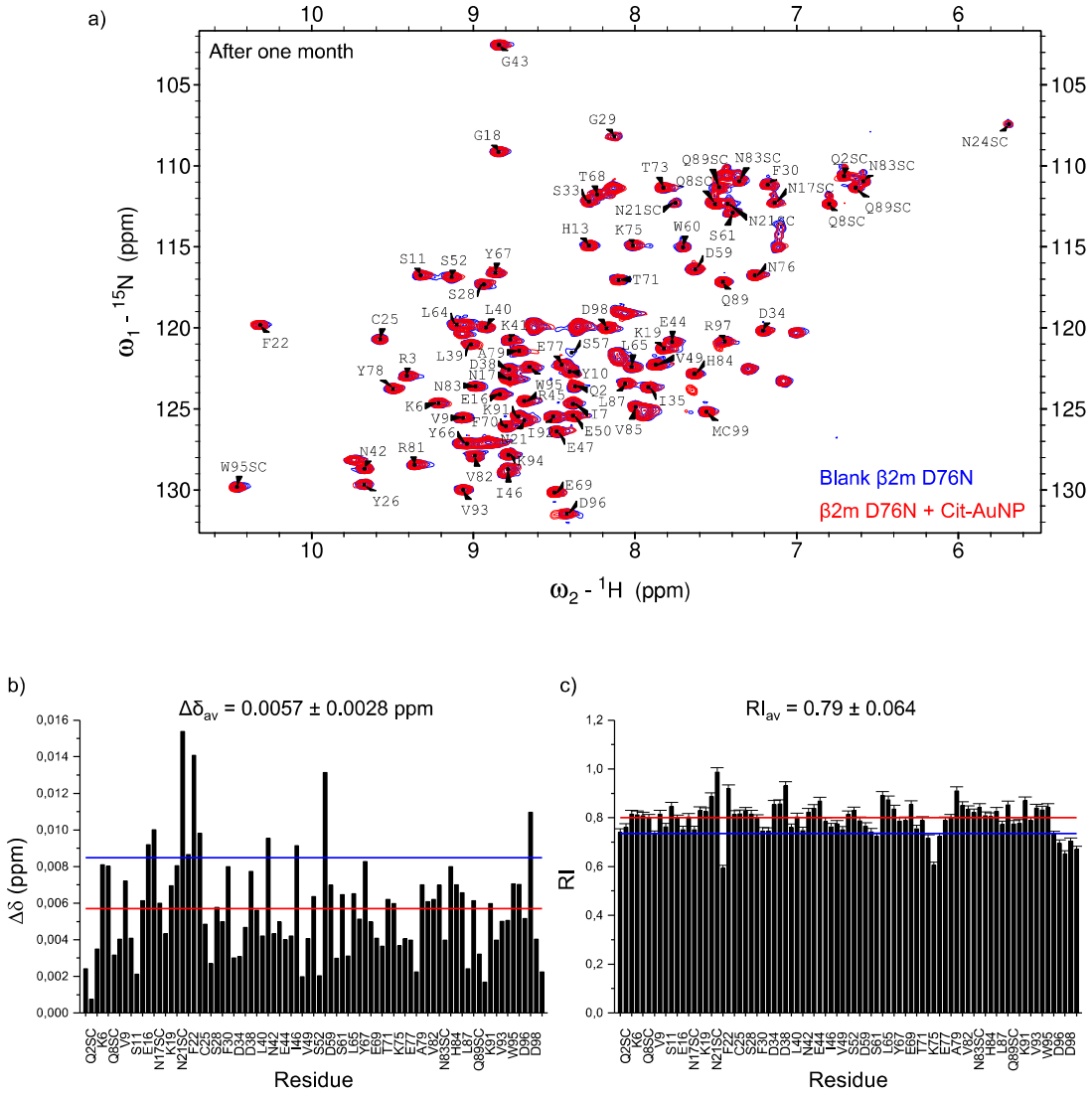

Figure 4.9. a) Superimposition of β2m D76N ^{15}N-^{1}H HSQC spectra recorded at 500 MHz after one month without (blue) and with (red) Cit-AuNP (protein/NP = 608). The corresponding backbone amide assignments are reported by single letter code and side chain amides are indicated with SC. b) and c) Bar plots of amide chemical shift perturbations (Δδ) and cross-peak attenuations (RI), respectively. The two horizontal lines indicate the average values (red) and the displacement of one standard deviation (blue) above and below the average, respectively. To avoid graphic crowding, the abscissa labels of both panels were reported only every other two signals. Besides the observed backbone amides, also the following detected side-chain (SC) NH resonances were included in the abscissa label list, according to the primary sequence order: Q2, Q8*, N17, N21*, N24*, N42*, N83*, Q89*, W95, where the asterisk indicates the inclusion of two separate resonances for asparagine

and glutamine side-chain amides. The missing labels do not include the following unobserved or non-existing backbone NH connectivities: I1, T4, P5, Q8, R12, P14, A15, S20, L23, N24, V27, H31, P32, E36, V37, H51, D53, L54, F56, S57, K58, F62, Y63, P72, E74, C80, T86, S88, P90.

From these data, it can be inferred that as for WT the C-terminal and the N-terminal domains are involved in the interaction with the NPs, but with D76N a new apical region near the C-terminal, made up mainly of the EF loop, proved to be affected. Furthermore, the chemical shift perturbation recorded on the older sample highlighted also another apical region represented by the AB loop (Figure 4.10).

a)

Structure region	RI outliers t = 0	RI outliers t = one month	Δδ outliers t = one month
N-term, A strand	Q2	Q8SC	
AB loop	N17SC		E16, N17, N21SC, F22
B strand			N24SC
BC loop			
CC', C'D loops	L40		
D strand			
DE loop	S57, S61	S61	
E strand			
EF loop	T71, K75	T73, K75, N76	
F strand			
FG loop			
G strand, C-term	D96, R97, M99	W95, D96, R97, D98	R97

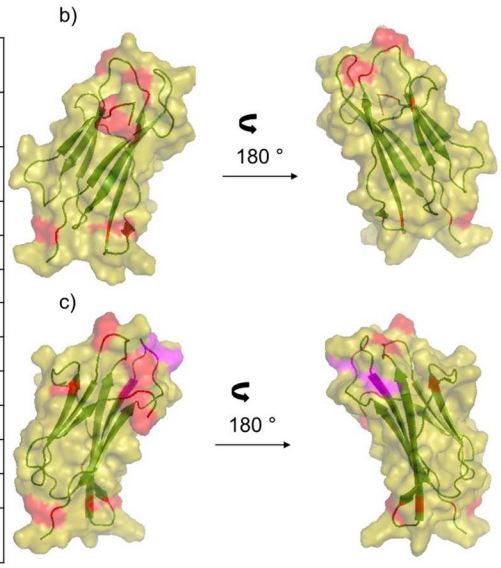

Figure 4.10. a) Synopsis of β2m D76N positions that proved most affected, i.e. displaced more than one standard deviation from the average by the presence of Cit-AuNPs and their secondary structure element location when protein/NP = 608. b) β2m D76N cartoon highlighting in red the locations of the residues reported in a) at t = 0. c) as in panel b) with the locations of the additional changes observed after one month coloured in magenta.

Most of the peaks in the spectrum of ΔN6 in presence of Cit-AuNPs did not move at all, but there were some signals that showed a significant chemical shift variation, i.e. higher than 0.02 ppm, which increased further after one month (Figure 4.11). The presence of chemical shift variations implies that some residues of ΔN6 experience a different local environment

in presence of the nanoparticle suggesting that the protein conformation is more perturbed than the one of the other two variants.

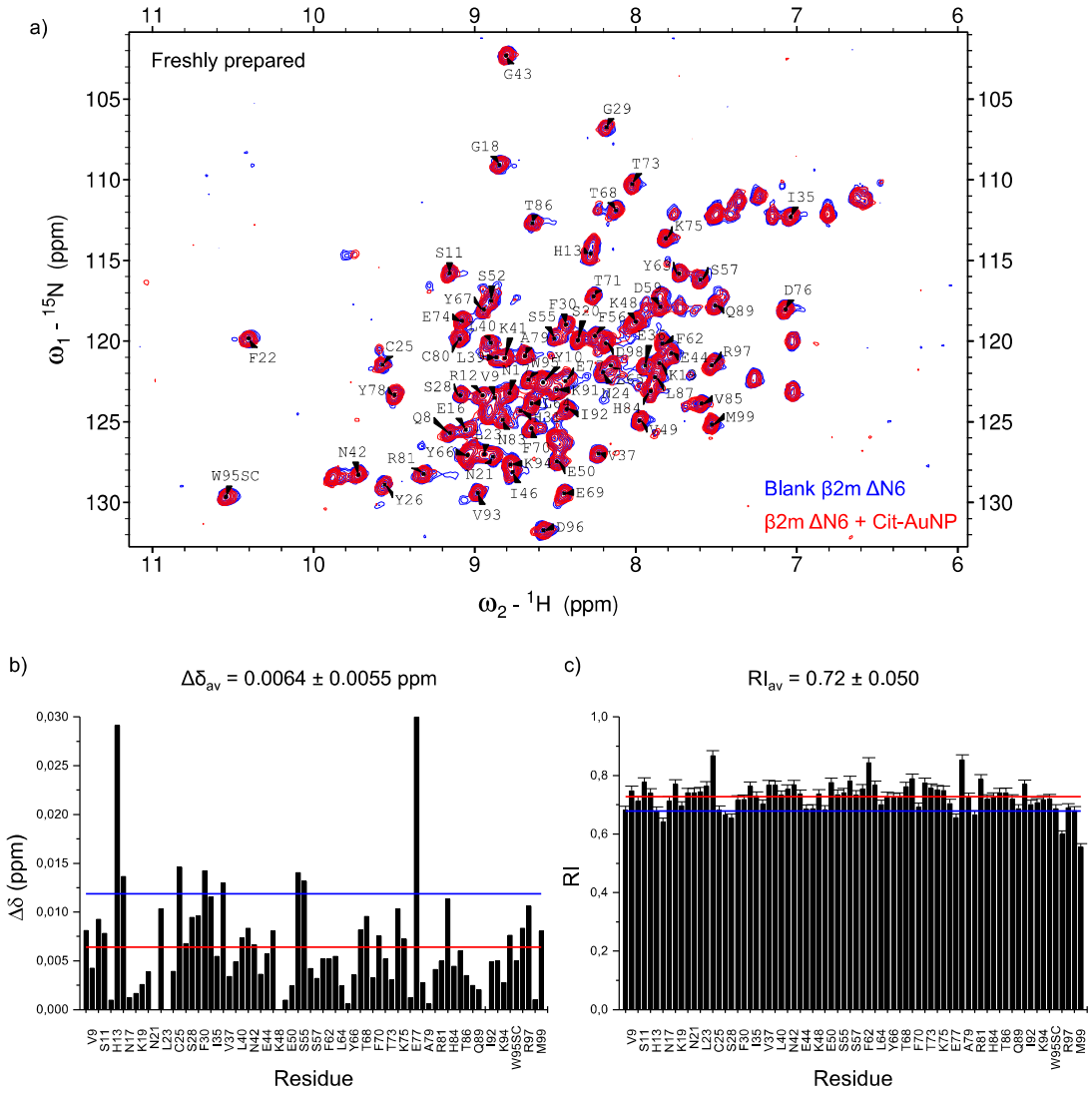

Figure 4.11. Superimposition of β2m ΔN6 ^{15}N-^{1}H HSQC spectra recorded at 500 MHz on freshly prepared samples without (blue) and with (red) Cit-AuNPs (protein/NP = 608). The corresponding backbone amide assignments are reported by single letter code and side chain amides are indicated with SC. b) and c) Bar plots of amide chemical shift perturbations (Δδ) and cross-peak attenuations (RI), respectively. The two horizontal lines indicate the average values (red) and the displacement of one standard deviation (blue) above and below the average, respectively. To avoid graphic crowding, the abscissa labels of both panels were reported only every other two signals. Besides the observed backbone amides, also W95 detected side-chain (SC) NH resonance was included in the abscissa label list. The missing labels do not include the following unobserved or non-existing

backbone NH connectivities: I7, P14, A15, V27, P32, S33, D34, D38, R45, E47, H51, D53, L54, K58, W60, S61, P72, V82, S88, P90.

Moreover, the protein region that is affected by the presence of the nanoparticle appeared to be more extended (Figure 4.12). In addition to almost all the apical loops, also some internal residues belonging to the strands (especially strand B) were affected. For example, the two cysteines, i.e. C25 and C80, responsible for the disulfide bridge that represents a structural determinant of the immunoglobulin domain, underwent intensity and chemical shift perturbations.

a)

Structure region	Δδ outliers t = 0	RI outliers t = 0	Δδ outliers t = one month	RI outliers t = one month
N-term, A strand				
AB loop	H13, E16	E16	E16	
B strand	C25	Y26, S28	C25, Y26, S28	N24, C25, S28
BC loop	F30		F30, D34	H31
CC', C'D loops	E36, S52		D38, S52	
D strand	S55		L54, S55	L54
DE loop				
E strand				
EF loop	E77	E77	E77	E77
F strand		C80		
FG loop			V85	
G strand, C-term		D96, M99	D98	D96, R97, D98, M99

b)

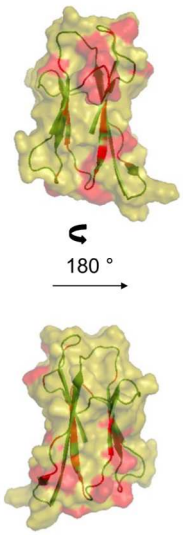

Figure 4.12. a) Synopsis of β2m ΔN6 positions that proved most affected, i.e. displaced more than one standard deviation from the average, by the presence of Cit-AuNPs and their secondary structure element location when protein/NP = 608. b) β2m ΔN6 cartoon highlighting in red the locations of the residues reported in a).

Concerning the peaks intensity, the average relative intensity of the spectrum recorded soon after the preparation of the solution was 0.72 ± 0.050 and increased after one month to 0.78 ± 0.13 due mainly to the intensity increase of three peaks, i.e. S55, V85 and D34 (Figure 4.13).

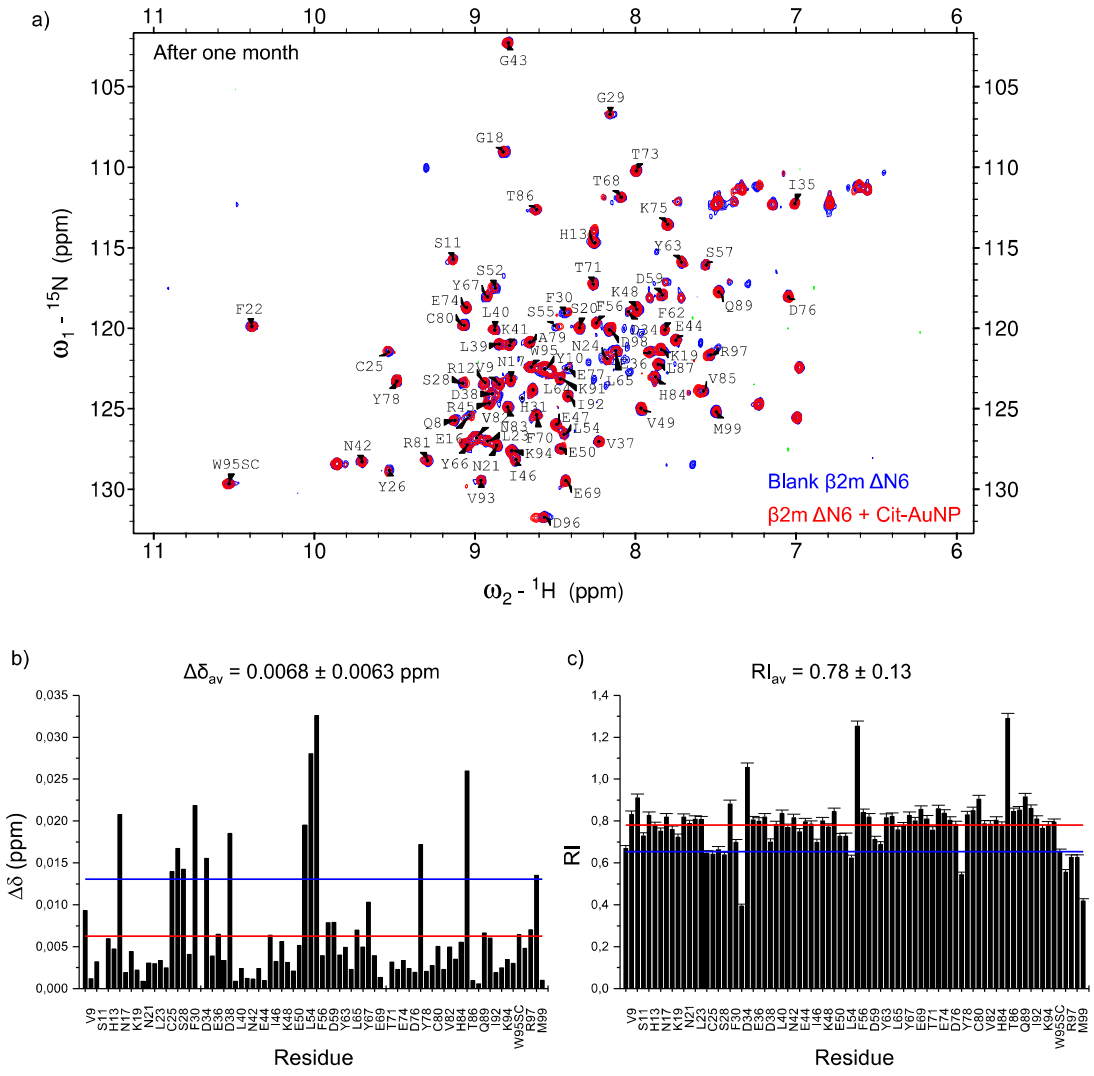

Figure 4.13. Superimposition of β2m ΔN6 ^{15}N-^{1}H HSQC spectra recorded at 500 MHz after one month without (blue) and with (red) Cit-AuNPs (protein/NP = 608). The corresponding backbone amide assignments are reported by single letter code and side chain amides are indicated with SC. b) and c) Bar plots of amide chemical shift perturbations (Δδ) and cross-peak attenuations (RI), respectively. The two horizontal lines indicate the average values (red) and the displacement of one standard deviation (blue) above and below the average, respectively. To avoid graphic crowding, the abscissa labels of both panels were reported only every other two signals. Besides the observed backbone amides, also W95 detected side-chain (SC) NH resonance was included in the abscissa label list. The missing labels do not include the following unobserved or non-existing backbone NH connectivities: I7, P14, A15, V27, P32, S33, H51, D53, K58, W60, S61, P72, S88, P90.

An intensity increase reflects a decrease in the transverse relaxation rate. This decrease can be connected to an increase in the local mobility of regions that are characterized by slow conformational exchange processes or to the

dynamics of resident water molecules. In this latter case, if a water molecule is strictly bound to a residue, the intensity of that residue signal is often affected by the efficiency of the selective flip-back pulse used in the HSQC sequence to suppress the solvent magnetization.[117] This efficiency, in turn, depends on experimental conditions (power missettings, radiofrequency inhomogeneity, specific selective pulse shape). β2m has several resident water molecules, among which the ones bound to H84 and L39 are the most important.[143] The intensity increases of V85 and of the spatially close D34 are likely to be associated with the reorganization of the water molecule bound to H84. The side chain of S55 forms probably hydrogen bonds with water, therefore its intensity can be modulated by water dynamics. Moreover, S55 is located within the DE loop which is known to undergo conformational exchange processes[144] whereas the whole D strand is surely involved in intermolecular association equilibria.[145] These processes can be surely affected in the presence of the nanoparticle. These possible explanations were no further investigated due to the low sample concentrations.

After one month, ΔN6 blank sample showed clear traces of unfolding with the appearance of new peaks in the random coil region (Figure 4.13 a). This destructuration did not happen in the sample in which the protein was incubated with Cit-AuNPs meaning that the NP presence was able to rescue ΔN6 from its intrinsic partial unfolding.

All the solutions were tested also after one year and they were found stable as the features observed after one month were maintained.

On decreasing the protein/NP ratio from 680 to 160, some chemical shift deviations were observed for all the three β2m variants, in addition to intensity attenuations. Considering the average relative intensity and the chemical shift variations, the perturbation extent sequence going from the least to the most perturbed was wild-type, D76N and ΔN6. The fact that the conformations of D76N and ΔN6 were more affected by the presence of the nanoparticles, can be justified considering that they are less stable than WT

of 2.7 and 2.5 kcal/mol, respectively.[61,63] In addition, the truncated structure of ΔN6 makes it less protected, meaning that any interaction can have a larger effect on the protein conformation, though the overall tertiary structure is still preserved.

By analysing the results obtained from the samples in which the protein/NP ratio was decreased, it was possible for WT to discover additional portions of the protein that were affected by the presence of the nanoparticles (Figures 4.14 and 4.15).

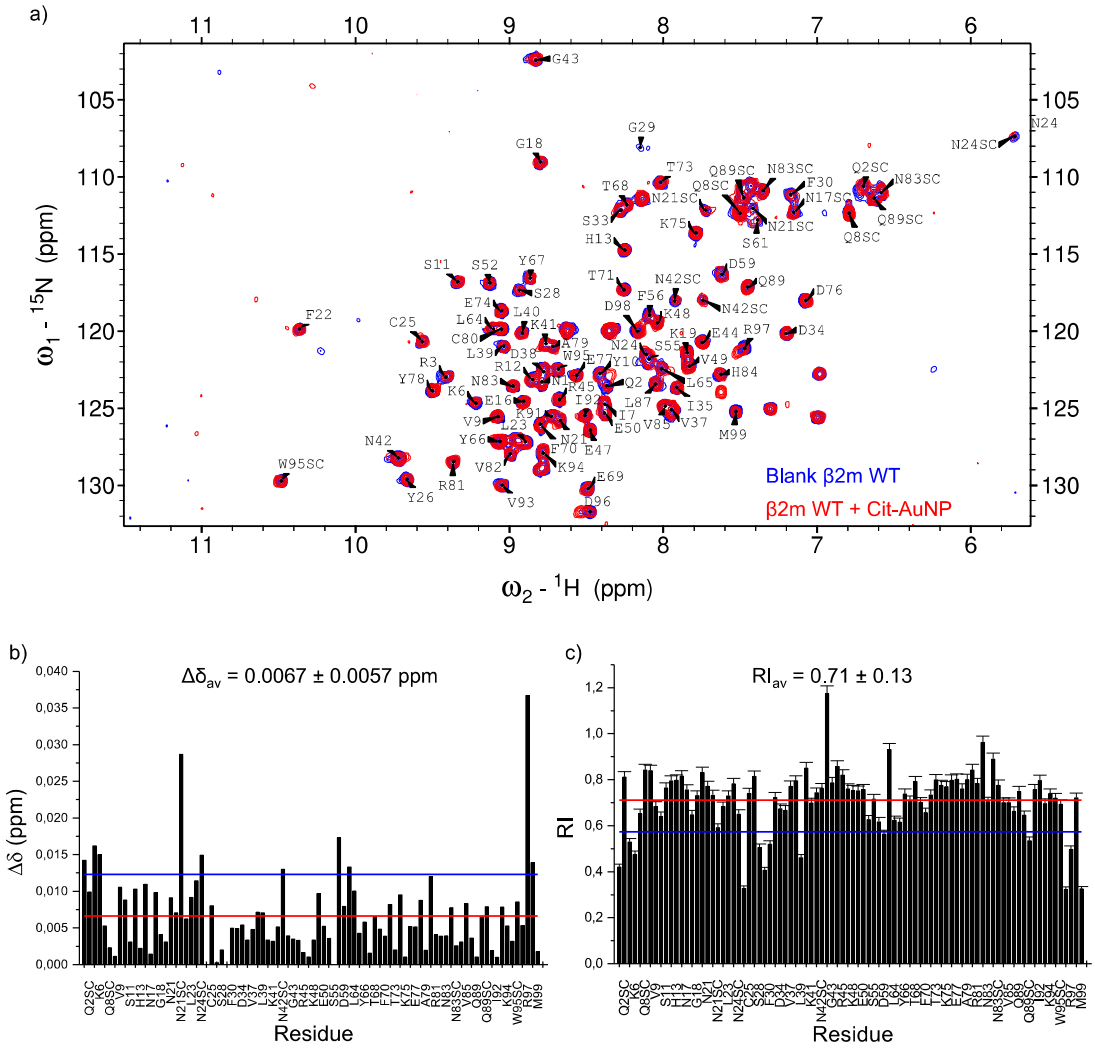

Figure 4.14. a) Superimposition of β2m WT ^{15}N-^{1}H HSQC spectra recorded at 600 MHz without (blue) and with (red) Cit-AuNPs (protein/NP = 160). The corresponding backbone amide assignments are reported by single letter code and side chain amides are indicated with SC. b) and c) Bar plots of amide chemical shift

perturbations (Δδ) and cross-peak attenuations (RI), respectively. The two horizontal lines indicate the average values (red) and the displacement of one standard deviation (blue) above and below the average, respectively. To avoid graphic crowding, the abscissa labels of both panels were reported only every other two signals. Besides the observed backbone amides, also the following detected side-chain (SC) NH resonances were included in the abscissa label list, according to the primary sequence order: Q2, Q8*, N17, N21*, N24*, N42*, N83*, Q89*, W95, where the asterisk indicates the inclusion of two separate resonances for asparagine and glutamine side-chain amides. The missing labels do not include the following unobserved or non-existing backbone NH connectivities: I1, T4, P5, Q8, P14, A15, S20, V27, H31, P32, E36, H51, D53, L54, S57, K58, W60, F62, Y63, P72, T86, S88, P90.

In particular, a more extended involvement of the region that surrounds the N-terminal top (N-terminal tail, BC loop and DE loop) was observed.

a)

Structure region	Δδ outliers	RI outliers
N-term, A strand	Q2, R3, K6	Q2, R3, K6
AB loop	N21SC	
B strand	N24SC	N24SC, S28
BC loop		G29, F30
CC', C'D loops	N42SC	L39
D strand		
DE loop	F56, S61	D59
E strand		
EF loop		
F strand		
FG loop		Q89SC
G strand, C-term	R97, D98	D96, R97, M99

b)

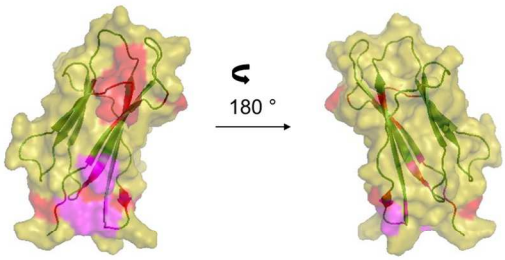

Figure 4.15. a) Synopsis of β2m WT positions that proved most affected, i.e. displaced more than one standard deviation from the average, by the presence of Cit-AuNPs and their secondary structure element location when protein/NP = 160. b) β2m WT cartoon highlighting in red the locations of the outlier residues already present when protein/NP = 608 and in magenta the additional ones revealed when protein/NP = 160.

The involvement of the AB loop for D76N, suggested by some chemical shift perturbations in the first older sample, was definitively confirmed in the second sample (Figures 4.16 and 4.17). It is worth noting that the D76N batch used to prepare these samples presented immediately after the dissolution some misfolding signals in both blank and NP-containing samples. It is quite

common finding instable D76N batches with a high tendency to spontaneous partial unfolding.

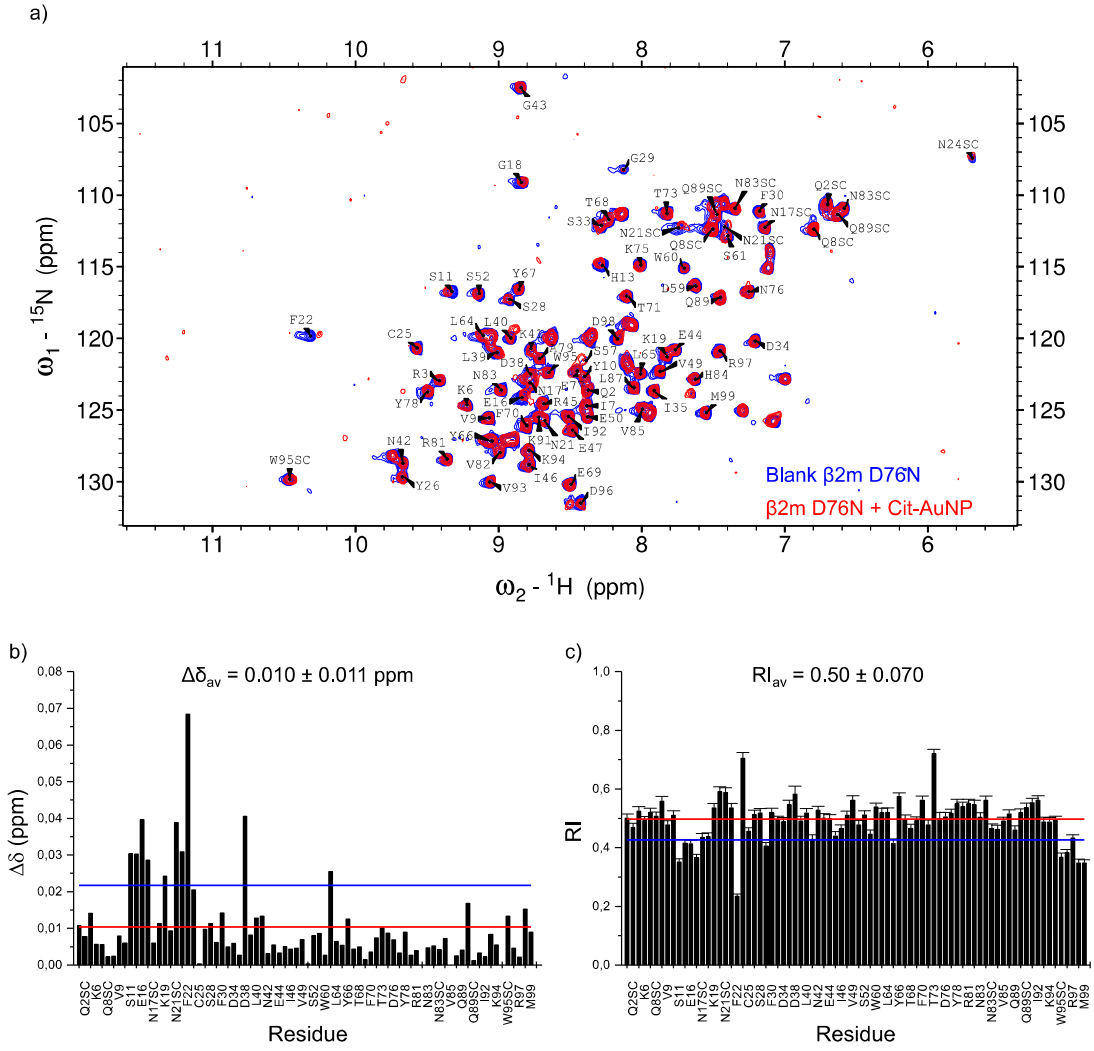

Figure 4.16. a) Superimposition of β2m D76N ^{15}N-^{1}H HSQC spectra recorded at 600 MHz without (blue) and with (red) Cit-AuNPs (protein/NP = 160). The corresponding backbone amide assignments are reported by single letter code and side chain amides are indicated with SC. b) and c) Bar plots of amide chemical shift perturbations (Δδ) and cross-peak attenuations (RI), respectively. The two horizontal lines indicate the average values (red) and the displacement of one standard deviation (blue) above and below the average, respectively. To avoid graphic crowding, the abscissa labels of both panels were reported only every other two signals. Besides the observed backbone amides, also the following detected side-chain (SC) NH resonances were included in the abscissa label list, according to the primary sequence order: Q2, Q8*, N17, N21*, N24*, N42*, N83*, Q89*, W95, where the asterisk indicates the inclusion of two separate resonances for asparagine and glutamine side-chain amides. The missing labels do not include the following unobserved or non-existing backbone NH connectivities: I1, T4, P5, Q8, R12, P14,

A15, S20, L23, N24, V27, H31, P32, E36, V37, H51, D53, L54, F56, S57, K58, F62, Y63, P72, E74, C80, T86, S88, P90.

a)

Structure region	Δδ outliers	RI outliers
N-term, A strand	S11	S11
AB loop	H13, E16, K19, F22	F22
B strand		
BC loop		
CC', C'D loops		
D strand		
DE loop	S61	
E strand		
EF loop		
F strand		
FG loop		
G strand, C-term		D96, R97, M99

b)

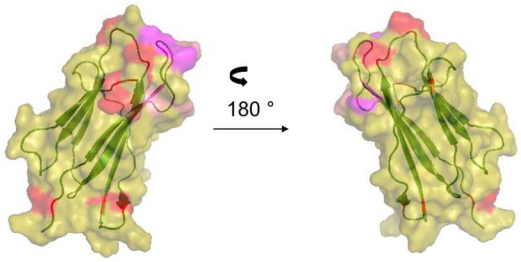

Figure 4.17. a) Synopsis of β2m D76N positions that proved most affected, i.e. displaced more than one standard deviation from the average, by the presence of Cit-AuNPs and their secondary structure element location when protein/NP = 160. b) β2m D76N cartoon highlighting in red the locations of the outlier residues already present when protein/NP = 608 and in magenta the additional ones revealed when protein/NP = 160.

The chemical shift perturbation in ΔN6 spectra considerably increased ($\Delta\delta_{av}$ = 0.032 ± 0.033 ppm), but did not involve other residues with respect to those observed at higher protein concentration. The intensity attenuation, instead, showed the involvement of other protein patches close to the ones highlighted before: the perturbation of the B strand propagated also to the neighbour strand A (Q8 and S11) and strand F (L65 and Y67) and the FG loop (V82 and N83), that is close to the BC loop, proved to be affected as well (Figures 4.18 and 4.19).

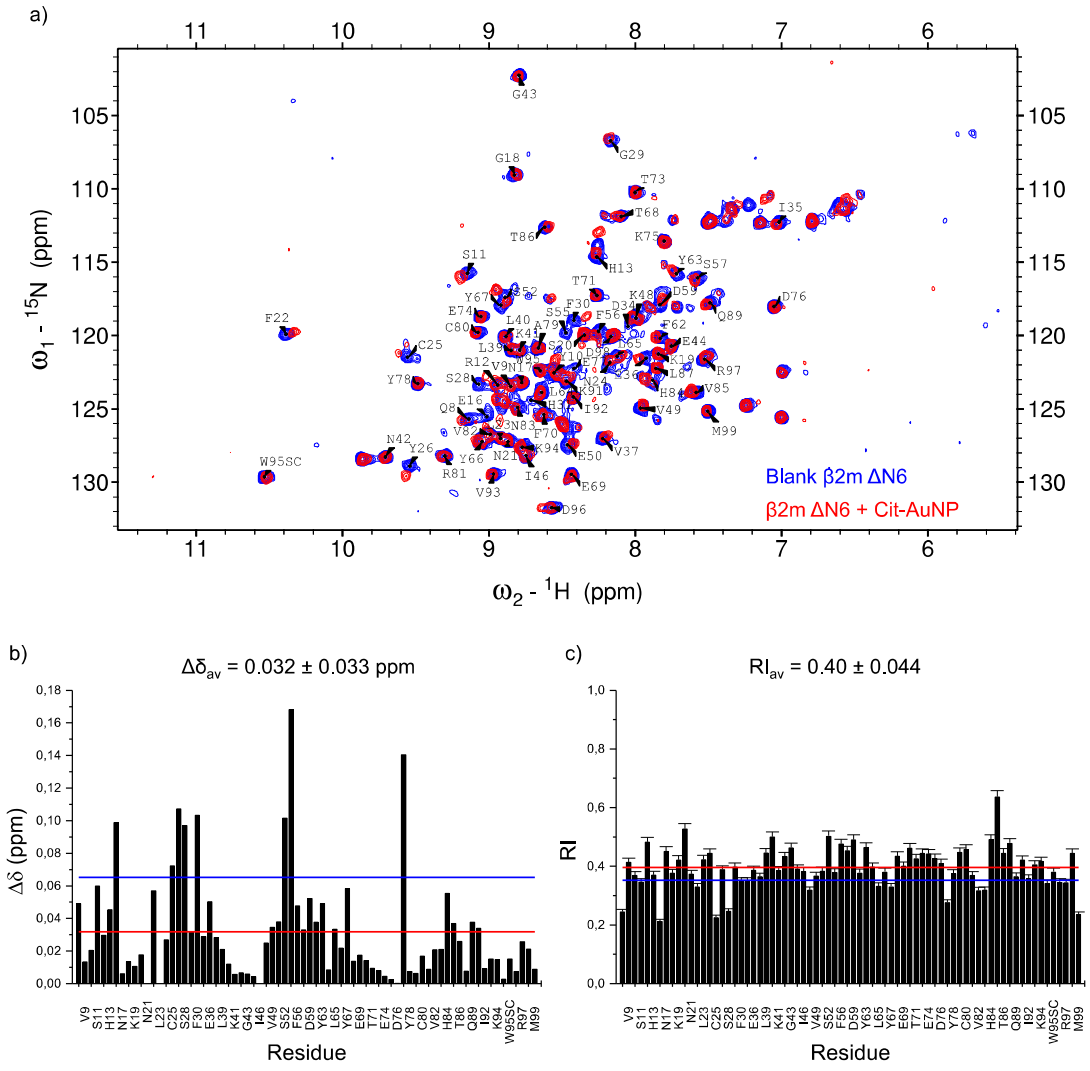

Figure 4.18. a) Superimposition of β2m ΔN6 ^{15}N-^{1}H HSQC spectra recorded at 600 MHz without (blue) and with (red) Cit-AuNPs (protein/NP ratio of 160). The corresponding backbone amide assignments are reported by single letter code and side chain amides are indicated with SC. b) and c) Bar plots of amide chemical shift perturbations (Δδ) and cross-peak relative intensity (RI), respectively. In c) the error was calculated from the signal-to-noise ratio. The two horizontal lines indicate the average values (red) and the displacement of one standard deviation (blue) above and below the average for Δδ and RI, respectively. To avoid graphic crowding, the abscissa labels of both panels were reported only every other two signals. Besides the observed backbone amides, also W95 detected side-chain (SC) NH resonance was included in the abscissa label list. The missing labels do not include the following unobserved or non-existing backbone NH connectivities: I7, P14, A15, V27, P32, S33, H51, D53, K58, W60, S61, P72, S88, P90.

a)

Structure region	Δδ outliers	RI outliers
N-term, A strand		Q8, S11
AB loop	E16	E16
B strand	C25, Y26, S28	C25, S28
BC loop	F30	H31
CC', C'D loops		
D strand	S55	L54
DE loop		
E strand		
EF loop	E77	E77
F strand		L65, Y67
FG loop		V82, N83
G strand, C-term		M99

b)

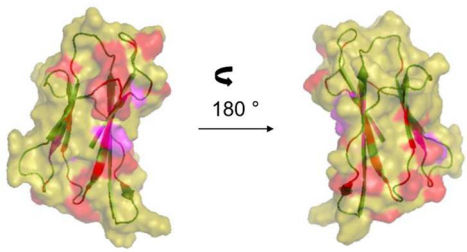

Figure 4.19. a) Synopsis of β2m ΔN6 positions that proved most affected, i.e. displaced more than one standard deviation from the average, by the presence of Cit-AuNPs and their secondary structure element location when protein/NP = 160. b) β2m ΔN6 cartoon highlighting in red the locations of the outlier residues already present when protein/NP = 608 and in magenta the additional ones revealed when protein/NP = 160.

The reported data suggest that when the protein is in high excess a longer equilibration time is required to propagate in the bulk solution the conformational effect induced by the NPs. When the protein excess is reduced, the equilibration time is faster and the effects of the interaction are more remarkable.

If the presence of a protein layer strongly bound in an irreversible manner to the NP is contemplated and the geometric maximum occupancy of the NP surface by the protein is considered, when the protein/NP ratio is 160 at least half of the protein should be permanently attached to the NP surface. Since the NMR signal of a protein firmly bound to a big object like a NP would be undetectable because of its broadness, all correlation peaks should show a relative intensity of at least 0.5. With all the three variants analysed, the presence of signals with relative intensity higher than 0.5 indicates that the existence of a hard corona tightly adsorbed on the NP surface and of a soft corona in exchange with the solution can be set aside.

What NMR actually showed is the effect on the protein upon its reversible and labile direct interaction with Cit-AuNPs. In all the recorded spectra only one signal for each amino acid was observed, except for D96 and R97. The occurrence of single resonances means that a slow exchange regime in which the exchange rate is much lower than the chemical shift difference between the free and NP-bound protein states can be ruled out. When there is a single peak whose position reflects the population-weighted averages of chemical shifts of the free and bound form, the exchange can be fast or intermediate with respect to the chemical shift scale. In intermediate regime, the exchange produces also an increase in the linewidth that can be as severe to determine the practical loss of the signal. However, the linewidth is not only affected by the rate of exchange, but also by the local dynamics and the overall rotational tumbling speed that determine both the dipolar (DD) and chemical shift anisotropy (CSA) contributions to relaxation. Therefore, the fact that there is only one intermediate signal whose intensity is usually decreased by linewidth broadening can account both for the onset of an intermediate exchange and/or for a fast exchange associated with a decrease in local mobility and/or a decrease in tumbling rate leading to DD/CSA broadening. The splitting of two signals (D96 and R97) is more likely to reflect an interconversion between two different, local conformations that occurs slowly with respect to the NMR time scale. So, the presence of 7.5-nm-diameter Cit-AuNPs favours the onset of a local conformational heterogeneity at the C-terminus of β2m that becomes detectable because of an inherently slow interconversion regime. This was observed for all the three variants tested.

The previous results[40,146] obtained with commercial, 5-nm-diameter Cit-AuNPs for WT and D76N β2m showed substantially no chemical shift variation, no clear hint of new conformations and no time dependence of the salient NMR parameters. In addition, the regions affected were restricted to smaller portions that however were found to be affected also in the present

work. This discrepancy should mainly be due to the different NP dimensions. The perturbation of β2m conformation was greater in presence of the bigger Cit-AuNPs used in this work. This can be explained simply considering that the lower surface curvature of bigger nanoparticles provides a larger surface area of contact that allows stronger interactions which result in greater perturbation of protein structure. Furthermore, AuNPs can have different superficial microstructure since they are produced with different methodologies. The relevance of curvature and microstructure for the affinity has been repeatedly pointed out.[23,147–149]

It is worth mentioning that the composition of the commercial and synthesized Cit-AuNP solutions was different. Commercial Cit-AuNPs showed ^{1}H NMR peaks assigned to unknown species that were declared to be present in the preparations (e.g. tartrate) while in-house-synthesized NPs displayed only citrate signals (Figure 4.20).

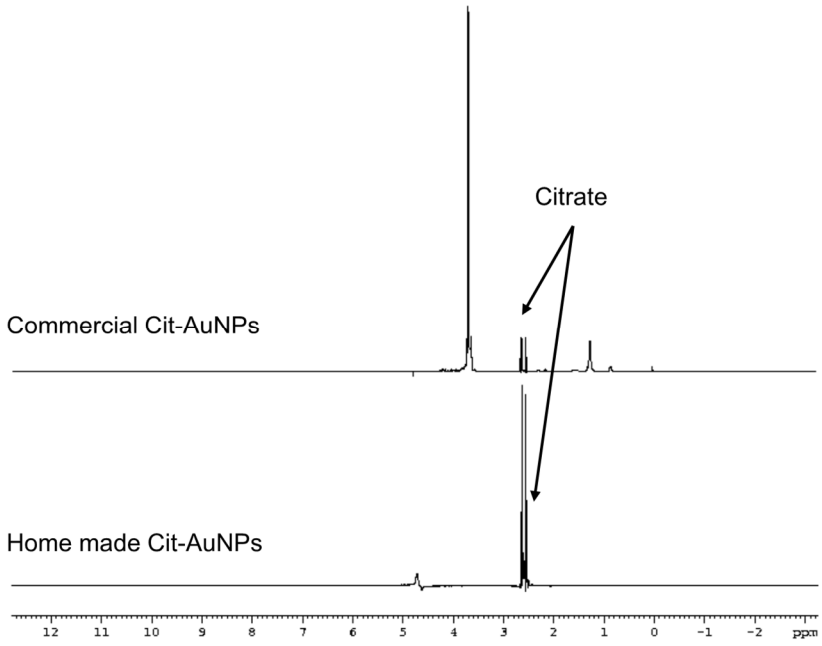

Figure 4.20. Stacked ^{1}H NMR spectra of commercial Cit-AuNPs (above) and in house synthesized Cit-AuNPs (below). The comparison between the two spectra reveals that while in the home made sample only citrate is present, in the purchased one other species are present in considerable amounts.

Moreover, the commercial products were always buffered with 25 mM sodium phosphate that was instead incompatible with the stability of the in-house-synthesized preparations.

4.1.3 β2m backbone dynamics and exchange processes in presence of Cit-AuNPs

^{15}N NMR relaxation experiments are powerful tools to gain information about the backbone dynamics of proteins. Longitudinal, transverse and rotating frame relaxation rates, along with ^{1}H-^{15}N NOE, are unique probes to investigate backbone internal motions at a single-residue level. In the attempt to understand the impact of Cit-AuNPs on β2m wild-type backbone internal motions, the measurement of these relaxation parameters was planned. The aim was to acquire information on possible differences in protein flexibility and to estimate the overall rotational correlation time by analysing relaxation parameters and NOE values in terms of reduced spectral density mapping.[150–154] Moreover, by comparing R_2 and $R_{1\rho}$, it would be possible to highlight chemical and/or conformational exchange contributions to the transverse relaxation. The attempt to perform this analysis failed because of the scarce quality of the spectra. Since the protein concentration was very low (4 μM), spectra had a low signal-to-noise ratio and the too large errors on relaxation rate values, i.e. between 15% and 30%, approximatively, made unreliable the analysis. R_1, R_2, $R_{1\rho}$ and NOE values and the corresponding errors are reported in the Appendix for β2m alone and in presence of Cit-AuNPs (Table A1 and A2). The large uncertainty prevented the significant identification of any variation in protein dynamics due to Cit-AuNPs presence. The impossibility to concentrate Cit-AuNPs without their aggregation restricts the operative protein concentration and consequently the accessibility to this quite demanding NMR experiments. On the other

hand, by increasing the protein concentration the large protein/NP ratio would dilute too much the NP-protein interaction effect.

To assess exchange contributions to transverse relaxation rates related to the interaction with nanoparticles, relaxation dispersion experiments were performed on both β2m alone and in presence of Cit-AuNPs. Even if the experiment and the fitting of relaxation dispersion curves was successful, again the low signal-to-noise ratio of the spectra did not allow to get reliable and definitive results. In Figure 4.21 the relaxation dispersion curves for some residues that have been found to be affected by exchange are shown and all the exchange rate constants obtained from the fitting are reported in Table 4.1.

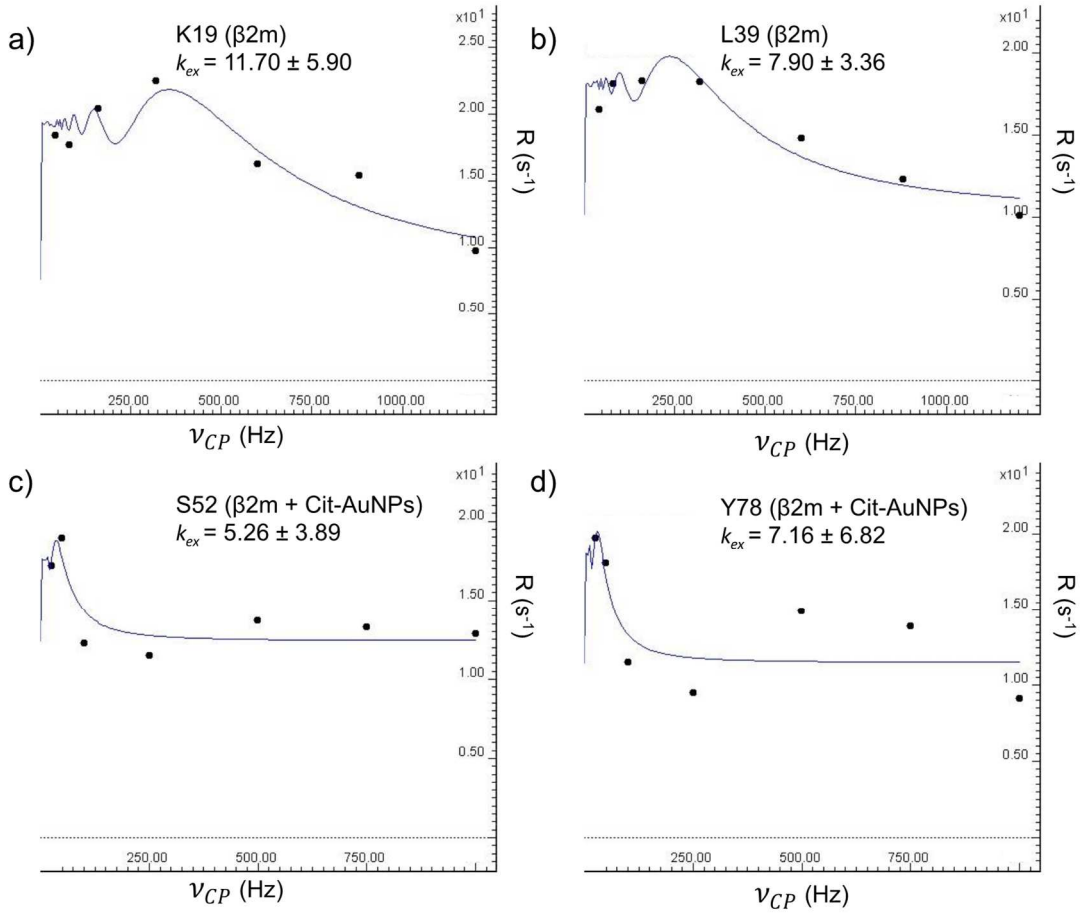

Figure 4.21. β2m relaxation dispersion curves for a) Lys19 and b) Leu39 in the control sample and of c) Ser52 and d) Tyr78 in the sample containing Cit-AuNPs. The blue lines correspond to the fitting with Equation 3.10.[130]

Table 4.1. Exchange constant values obtained by fitting relaxation dispersion data using Equation 3.10 (slow exchange limit) or Equation 3.11 (fast exchange limit).

β2m			
Residue	**Exchange limit**	**k_{ex} (s^{-1})**	**k_{ex} error (s^{-1})**
Gln2	Slow	13.9	21.40
Lys19	Slow	11.7	5.90
Leu39	Slow	7.90	3.36
Lys75	Slow	2.16	18.10
Glu77	Slow	2.54	17.74
Phe22	Fast	941	6129
Asp96	Fast	96.9	1729
β2m + Cit-AuNPs			
Arg12	Slow	8.00	9.12
Lys19	Slow	3.34	6.64
Leu23	Slow	3.89	5.23
Ser52	Slow	5.26	3.89
Ser61	Slow	20.5	428.8
Glu69	Slow	2.91	9.32
Phe70	Slow	10.4	11.70
Tyr78	Slow	7.16	6.82
His84	Slow	2.85	4.33
Gln2	Fast	475	1173
Arg81	Fast	1150	3101
Thr86	Fast	213	634.9

Additional work is still in progress in order to optimize relaxation experiments.

4.1.4 Binding of β2m variants to Cit-AuNPs

To characterize the binding of the three β2m variants selected, i.e. wild-type, D76N and ΔN6, with Cit-AuNPs, two different spectroscopic techniques were exploited. The effect of the interaction was studied both on β2m intrinsic fluorescence and on Cit-AuNP UV-Vis absorption.

Dissolving different concentrations of β2m going from 0.5 to 10 μM in 25 nM Cit-AuNP solutions caused the complete quenching of the protein. To follow this quenching phenomenon, small amounts of Cit-AuNPs were progressively added to 0.5 μM β2m solutions going from a protein/NP ratio

of 5000 to 500, approximately. During the titration, the shape and the position of the protein emission spectra were preserved for all the variants tested (Figure 4.22 a, b, c and d).

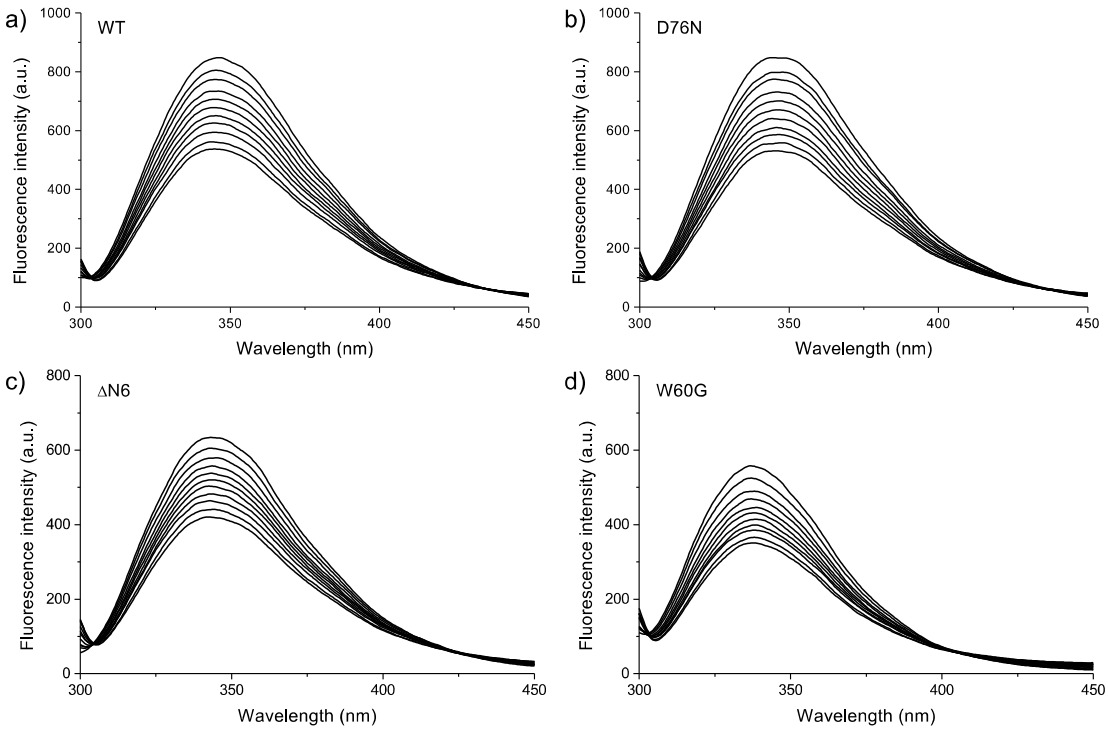

Figure 4.22. a), b), c) and d) Fluorescence quenching of 0.5 μM WT, D76N, ΔN6 and W60G β2m, respectively, with Cit-AuNP concentrations ranging from 0 to 0.8 nM.

This means that at the protein/NP ratios employed for the fluorescence analysis the native structure of all the three proteins was conserved without any perturbation of the core region in which Trp95, the main responsible of β2m fluorescence, is buried. The capability of Cit-AuNPs to quench not only the more exposed tryptophan residue (Trp60) but also the more protected one (Trp95) was confirmed by the complete quenching of the protein by higher NP concentrations and also by the fact that using W60G mutant, in which the outermost tryptophan is replaced by a glycine, the same quenching trend was found (Figure 4.22 d).

As predicted by the Stern-Volmer model,[111] on increasing the NP concentration the protein fluorescence intensity decreased following a linear

trend (Figure 4.23 a). Since on the surface of a nanoparticle there are multiple protein binding sites, the Hill equation[23] was applied to the fluorescence data (Figure 4.23 b) to estimate the apparent dissociation constants (K_d).

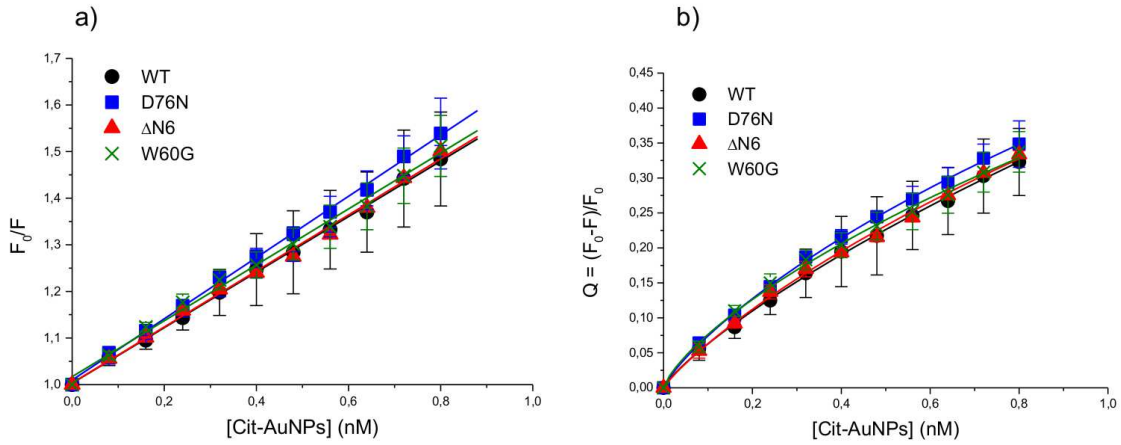

Figure 4.23. WT, D76N, ΔN6 and W60G β2m fluorescence quenching data fitted by a) the Stern-Volmer equation[111] and b) the Hill equation.[23] Data are presented as average of three independent experiments and the error is the standard deviation.

The values obtained from the Hill fitting are reported in Table 4.2.

Table 4.2. Parameters obtained from fluorescence quenching data fitted with Hill equation for WT, D76N, ΔN6 and W60G β2m. See Section 3.2 for error calculation.

β2m variant	K_d /10^{-9} M	Hill coefficient	R^2
WT	2.3 ± 0.50	0.91 ± 0.090	0.98
D76N	1.8 ± 0.48	0.88 ± 0.098	0.99
ΔN6	1.9 ± 0.29	0.92 ± 0.093	0.99
W60G	2.6 ± 0.54	0.79 ± 0.13	0.99

As can be seen from Table 4.2, the dissociation constants are in the range of 10^{-9} M and are the same within the experimental error for all the four variants. If a static quenching is assumed, these constants represent the strength of the complex between the proteins and Cit-AuNPs. A K_d in the nM range implies a very strong binding that should reach very quickly saturation. The NMR experimental evidence is inconsistent with this picture, because an important increase in the degree of protein signal perturbations was observed moving from a protein/NP ratio of 680/1 to 160/1. However,

the quenching process can not be purely collisional because considering that tryptophan fluorescence lifetimes (τ_0) in proteins range between 1 and 10 ns,[155] the bimolecular quenching constant (k_q) would be 10^{17}-10^{18} M^{-1} s^{-1}, which is unphysical. In addition to the formation of a complex between Cit-AuNPs and the proteins, there should be other mechanisms that contribute to quenching, i.e. RET (Resonance Energy Transfer) or photoinduced electron transfer.[155] Since the variant W60G β2m, bearing a single tryptophan residue at position 95, keeps exhibiting the same fluorescence quenching pattern as observed with the other β2m species containing two tryptophan residues, an intramolecular donor-acceptor transfer mechanism, i.e. FRET (Förster Resonant Energy Transfer), can be safely ruled out.

From a nanoparticle point of view, the interaction can be studied by analysing the effect of the protein adsorption on the SPR band of AuNPs in the UV-Vis spectrum. The addition of increasing amounts of the selected β2m variants to Cit-AuNP solution induced a progressive red shift of the plasmon absorption peak along with its broadening and intensity increase (Figure 4.24).

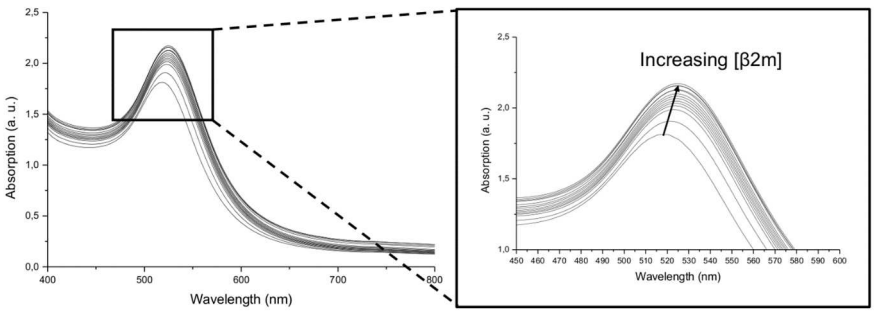

Figure 4.24. UV-Vis spectra of 30 nM Cit-AuNP after the progressive addition of WT β2m (0-20 μM). The enlargement highlights the spectral changes. The same outcome was obtained also for D76N and ΔN6.

To estimate if the binding affinity of the different variants for Cit-AuNPs is of the same extent, the shift of the SPR peak as the protein concentration increases was fitted to a Langmuir adsorption isotherm[37] (Figure 4.25).

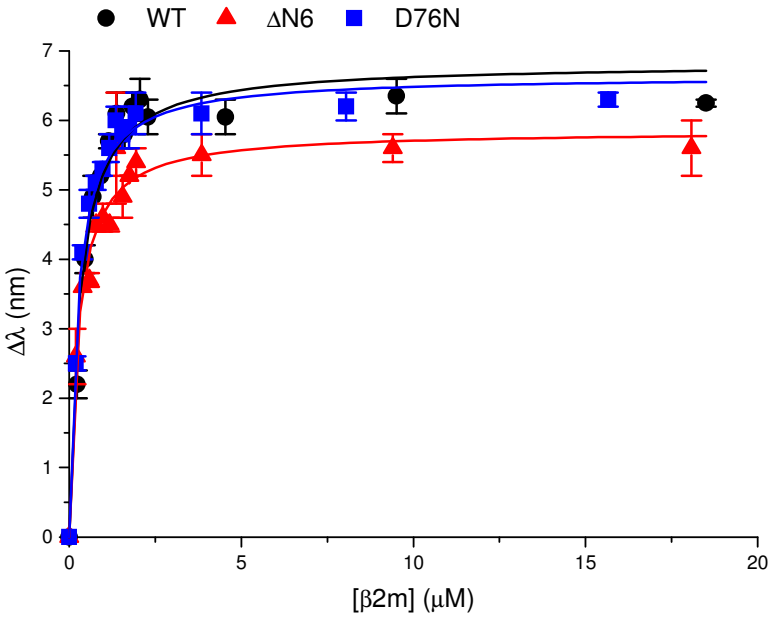

Figure 4.25. Plot of the variation of the plasmon band maximum as a function of β2m concentration for WT (black dots), ΔN6 (red triangles) and D76N (blue squares). The straight lines correspond to the Langmuir fitting.[37] The experiment was done in triplicate for each variant and the error is the standard deviation.

The saturation level was reached when the protein/NP ratio was around 60-100, in good agreement with geometrical calculations and with a single protein layer formation. The values obtained from the fitting are reported in Table 4.3. The binding constants of the three β2m variants are in the same range, considering the statistical error, meaning that the extent of the interaction with Cit-AuNPs is the same.

Table 4.3. Parameters obtained from UV-Vis data fitted with Langmuir equation for WT, D76N and ΔN6 β2m.

β2m variant	K_a (M^{-1})	$\Delta\lambda_{max}$ (nm)
WT	(3.33 ± 0.53) x 10^6	6.82 ± 0.20
D76N	(4.12± 0.40) x 10^6	6.64 ± 0.12
ΔN6	(3.96 ± 0.52) x 10^6	5.85 ± 0.14

The same experiment was done only with WT on purchased Cit-AuNPs of 20 nm. To compare the strength of the interaction with Cit-AuNPs of different sizes, a solution of synthesized 7.5 nm AuNPs was diluted to a

value in which the gold surface area was the same as in the purchased 0.8 nM 20 nm NPs. With the bigger NPs the association constant was found to be (14.62 ± 0.98) x 10^6 and with 7.5 nm NPs it was (8.20 ± 0.87) x 10^6. The stronger association of the protein on the 20 nm NPs can be explained considering that there is a flatter surface for the interaction, i.e. the affinity increases on lowering the curvature.[23] Another interesting feature worth being considered is the increase of the apparent association constant with dilution of 7.5-nm NPs. This behaviour reflects a stoichiometry other than 1:1.

It is worth noting that the application of the Langmuir model is a very simple way to describe the absorption of molecules to a surface, but is not completely suited to protein-NP systems mainly because it assumes that on the surface there is only one type of binding site, though it is well known that gold clusters have different surface defects like corners and edges with different binding affinities.[156]

Although the constant values obtained from fluorescence and UV-Vis data can not be considered actual values for the reasons stated before, these experiments provided useful information. Both experiments revealed that the extent of the interaction is the same for the three variants despite the conformational perturbation of ΔN6 proved to be more extended in the NMR experiments. Furthermore, fluorescence results rule out an overall native structure loss in presence of Cit-AuNPs for all the three mutants, as inferred from NMR experiments.

4.1.5 Effect of Cit-AuNPs on β2m aggregation and association equilibria

The frequency shift (Δf) and the dissipation change (ΔD) were recorded when D76N β2m alone, Cit-AuNPs alone and the mixture with a protein/NP

ratio of 35 flowed on the Au-coated QCMD sensor (Figure 4.26). D76N variant was chosen because it displays in solution more pronounced inter-monomer interactions, consistently with enhanced amyloidogenicity. The saturation Δf (Δf_{sat}) and ΔD (ΔD_{sat}) values are reported in Table 4.4. The differences in Δf_{sat} and ΔD_{sat} observed for D76N β2m in presence and in absence of Cit-AuNPs are significative, since the error correlated with frequency and dissipation changes are ±0.1 Hz and 1×10^{-7} dissipation units, respectively.[157]

The frequency shift was fitted with the Sauerbrey equation[48] to calculate the mass density expressed in ng · cm^{-2} (Figure 4.27 d). From the mass density, it was possible to calculate the surface coverage density in terms of particle/cm^2 (Table 4.4). For the protein alone a higher surface coverage was calculated (14.5×10^{12}) with respect to the protein in presence of Cit-AuNPs (12.7×10^{12}). If the crystallographic dimensions of β2m[139] are considered, a surface coverage of 11.4×10^{12} proteins/cm^2 and 26.3×10^{12} proteins/cm^2 can be estimated for lying and standing β2m cylindroids, respectively. Thus, it can be inferred that D76N β2m formed mainly a single protein layer on the sensor substrate approaching the surface preferentially through the β-sheet domains and that the packing density was reduced in presence of Cit-AuNPs. As far as Cit-AuNPs are concerned, the experimental surface coverage (0.053×10^{12} NPs/cm^2) was far from the one calculated from the NP diameter obtained by TEM considering a filling factor of 0.65[38] (1.47×10^{12} NP/cm^2).

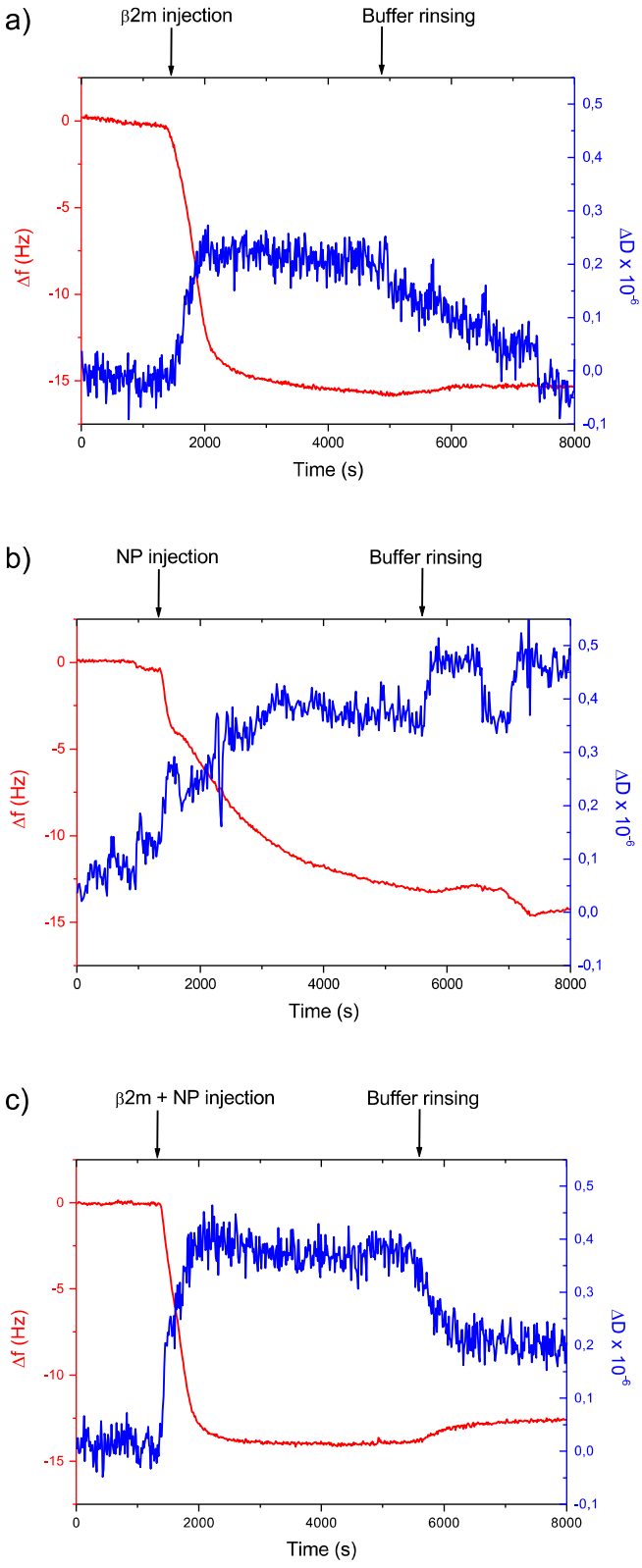

Figure 4.26. QCMD frequency (red) and dissipation (blue) plots for a) D76N β2m, b) Cit-AuNPs and c) D76N β2m in presence of Cit-AuNPs.

Table 4.4. QCMD adsorption data at saturation, their percentage variation after rinsing and the particle (protein or nanoparticle) density calculated from Sauerbrey fitting[48] of frequency data for D76N β2m, Cit-AuNPs and D76N β2m in presence of Cit-AuNPs.

Sample	Δf_{sat} (Hz)	$\Delta D_{sat}/10^{-6}$	$\Delta f_{rinsing}$ (%)	particles/cm^2
D76N β2m	-15.7	0.16	2.5 %	14.5 x 10^{12}
Cit-AuNPs	-12.2	0.36	-8.5 %	0.053 x 10^{12}
D76N β2m + Cit-AuNPs	-13.9	0.39	9.3 %	12.7 x 10^{12}

To evaluate the adsorption kinetics, the Boltzmann fitting of the Δf plot was performed (Figure 4.27 a, b and c). The values of the adsorption time constants (dt) (Table 4.5) revealed that the protein rate of adsorption was higher in presence than in absence of Cit-AuNPs. This faster behaviour of the protein when incubated with NPs can be explained considering the occurrence of a lower extent of oligomeric association.

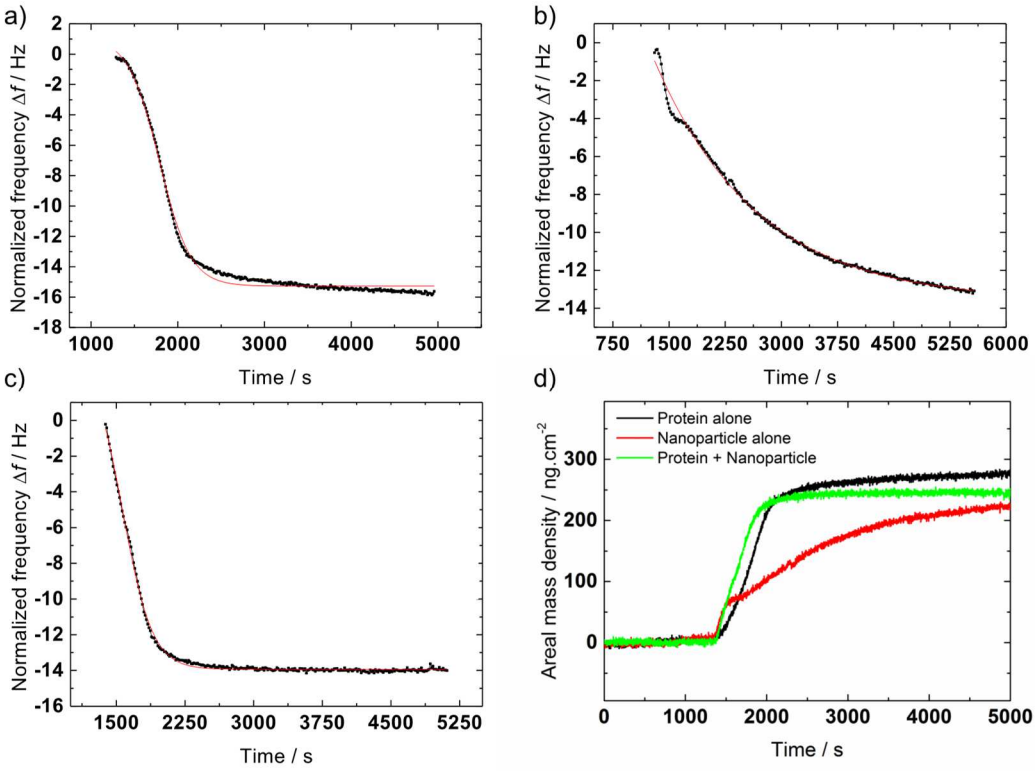

Figure 4.27. Plots showing QCMD frequency changes as a function of time when a) β2m, b) Cit-AuNPs and d) β2m/Cit-AuNPs mixture (35/1) were injected. The red lines indicate the Boltzmann sigmoid fitting. In d) the corresponding mass density plot obtained from Sauerbrey equation[48] is reported.

Table 4.5. Parameters obtained from QCMD frequency data fitted with Boltzmann sigmoid.

Sample	A_1 (Hz)	A_2 (Hz)	t_0 (s)	dt (s^{-1})	χ^2	R^2
D76N β2m	1.14±0.16	-15.27±0.02	1788.20±5.36	180.55±3.58	0.098	0.99
Cit-AuNPs	1949.27±24044.73	-13.63±0.10	-5588.50±17263.4	1369.13±81.02	0.048	0.99
D76N β2m + Cit-AuNPs	3.83±0.29	-13.93±0.01	1568.17±6.04	163.13±2.32	0.017	0.99

From the frequency plots another important information can be drawn. After the buffer rinsing step, for both the protein alone and in presence of Cit-AuNPs, a small frequency increase was recorded reflecting a fractional desorption and washing away of the protein. Probably, while most of the proteins were bound to the gold surface in an irreversible way, a small fraction was only physisorbed and could be easily removed by rinsing. The percentage of frequency variation induced by rinsing was higher in presence of Cit-AuNPs (Table 4.4) probing that more proteins were loosely bound.

During the adsorption process, the frequency shift was associated with a dissipation change (Figure 4.26). The energy dissipation is related to the viscoelastic properties of the adsorbed layer. D76N β2m showed a very low dissipation increase typical of rigid systems.[157] This behaviour reflects β2m small dimensions and its compact structure. In presence of Cit-AuNPs, a larger dissipation change was observed indicating the presence of a more flexible protein layer. To relate dissipation changes to frequency changes as they occurred during time, ΔD was plotted versus -Δf (D-f plot) (Figure 4.28).

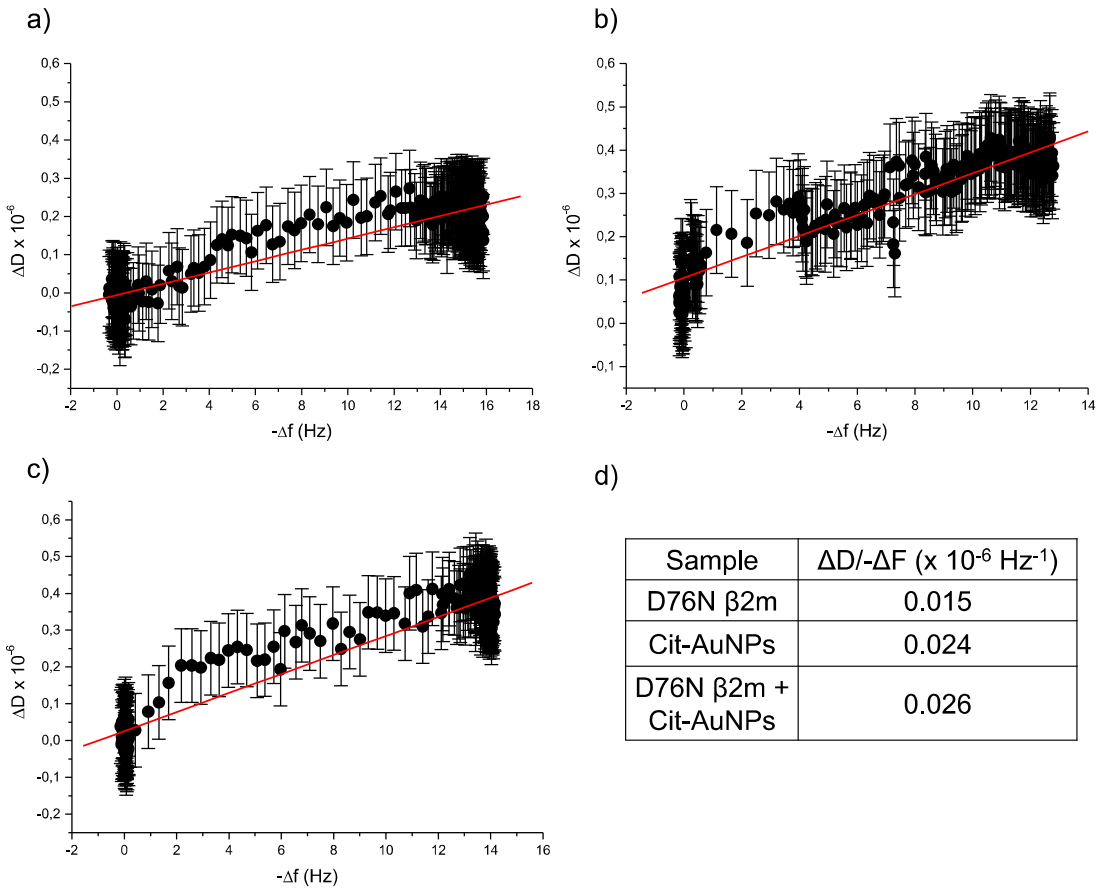

Sample	ΔD/-ΔF (x 10^{-6} Hz^{-1})
D76N β2m	0.015
Cit-AuNPs	0.024
D76N β2m + Cit-AuNPs	0.026

Figure 4.28. D-f plots for a) D76N β2m, b) Cit-AuNPs and c) D76N β2m in presence of Cit-AuNPs. The error bar corresponds to 1 × 10^{-7}.[157] The red lines represent the linear fittings. The table in d) reports the slope of the linear fittings.

The density of the points in D-f plots depends on the adsorption kinetics, the faster the kinetics the farther the points. The lower density of the points in the D-f plot that corresponds to the protein incubated with Cit-AuNPs (Figure 4.28 c) confirmed the faster adsorption kinetics already found with Boltzmann fitting of frequency variation data. Moreover, the presence of a single slope in each plot assured that there was only one kinetic process during adsorption.[136,137] The possibility of recognizing two slopes, albeit beyond the experimental error confidence, appears consistent with an adsorption mechanism proposed by Glomm *et al.*[137] The presence of a second distinct slower adsorption regime is explained by Gloom and co-workers with an initial adsorption where protein-surface interactions prevail and

then, as the surface coverage increases, also protein-protein interactions become important slowing down the adsorption process. Beyond kinetic information, the slope of D-f plots is related to the viscoelastic properties of the adsorbed layer.[137] As can be seen in Figure 4.28 d, a higher slope was extracted for the sample in which the protein was incubated with Cit-AuNPs.

The larger dissipation and dissipation derivative with respect to mass deposition of protein with NP should be due to intermolecular (interstitial) hydration increase. The intermolecular hydration decreases the compactness of the protein layer and thereby increasing its dissipative ability and reflects also the lower Δf. The increase of interstitial water in presence of AuNPs can be again attributed to a lower degree of protein association.

To further prove that QCMD results can be correlated to Cit-AuNPs ability to affect D76N β2m association equilibria, the translational diffusion coefficients of β2m species in the absence and in the presence of Cit-AuNPs were measured by recording DOSY experiments.[133] It has been already shown that in solution β2m monomers exist in equilibrium with aggregated oligomers of variable stoichiometry among which the dimer is the most abundant one.[140,141] This means that the diffusion coefficient measured by DOSY is an average of these species with different molecular weight. It was found that Cit-AuNPs increased systematically the diffusion coefficients of all the β2m variants considered (Figure 4.29). The difference was more evident with the more amyloidogenic variants but is definitely assessed also for wild-type β2m. The increase in the diffusion coefficient recorded in presence of Cit-AuNPs is consistent with a shift of β2m association equilibria towards the lower molecular weight oligomers, i.e. closer to the monomer.

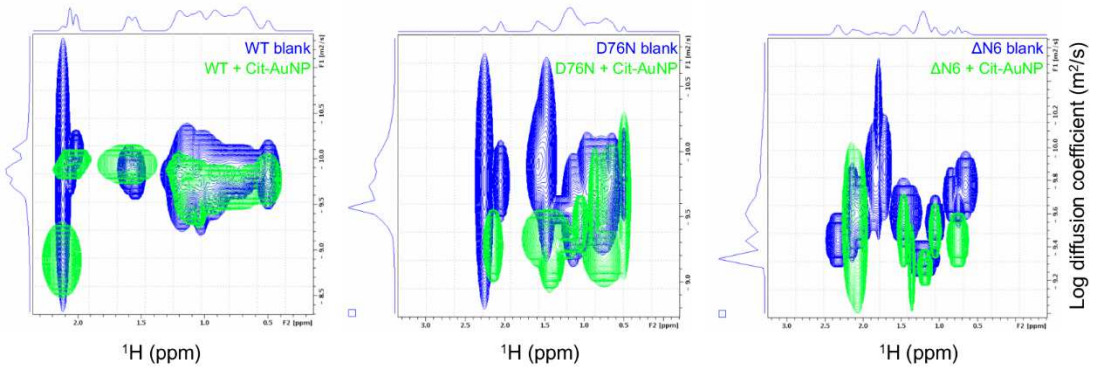

Figure 4.29. Overlap of aliphatic region of WT, D76N and ΔN6 DOSY spectra recorded without (blue) and with (green) Cit-AuNPs.

This result is in agreement with QCMD results and also with molecular dynamics simulations in which D76N dimers revealed to be disrupted in presence of Cit-AuNPs.[146]

4.2 Cit-AuNP effect on D76N β2m fibrillogenesis

Cit-AuNPs proved to be able to interfere with β2m self-assembly and with ΔN6 variant partial unfolding. The association of β2m monomers and the presence of partially unfolded intermediates are both considered key steps in β2m fibrillation process,[54] therefore, Cit-AuNPs direct effect on β2m *in vitro* fibrillogenesis was studied.

Among the β2m variants, D76N is the only one that requires fibrillogenic conditions compatible with Cit-AuNP stability. Typically, β2m fibrillogenesis is triggered *in vitro* by acidic conditions, whereas D76N variant forms fibrils at neutral pH by incubation at 37 °C and agitation.

To follow D76N fibril formation, three different methods were employed: thioflavin T (ThT) fluorescence, TEM and native agarose gel electrophoresis. The ThT assay (Figure 4.30) showed that, when the fibrillogenesis was done in presence of Cit-AuNPs, the fluorescence recorded was lower compared to the control sample.

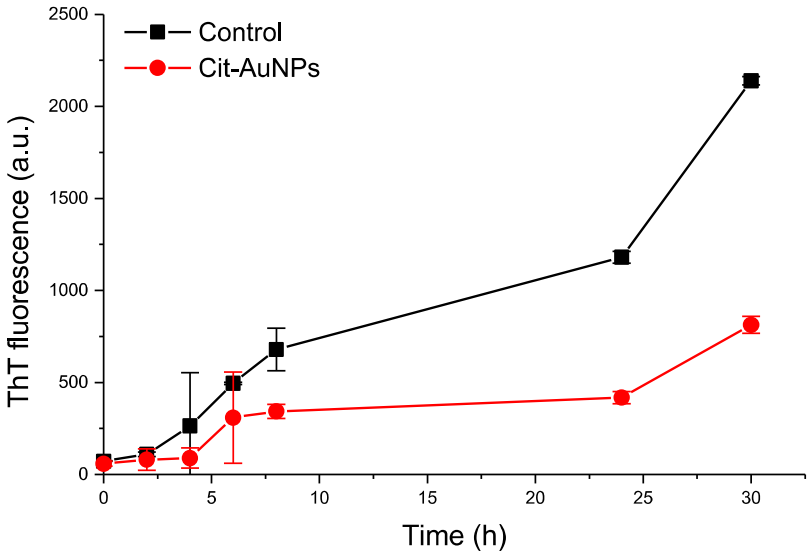

Figure 4.30. Fibrillogenesis of 20 μM D76N β2m monitored by means of ThT fluorescence intensity in the control sample (black line) and in the presence of Cit-AuNPs (red line). Measurements were always performed in triplicate.

The possibility of ThT fluorescence quenching by the nanoparticles was ruled out by observing that the ThT fluorescence intensity of D76N β2m mature fibrils in the absence and in the presence of Cit-AuNPs was the same. This led to the conclusion that the ThT assay result shown in Figure 4.30 reflected a partial inhibition of fibrillogenesis in presence of Cit-AuNP. This result was further confirmed by TEM images. The control sample showed a huge amount of fibrils, instead, when D76N β2m was incubated with Cit-AuNPs, fibres could hardly be detected (Figure 4.31).

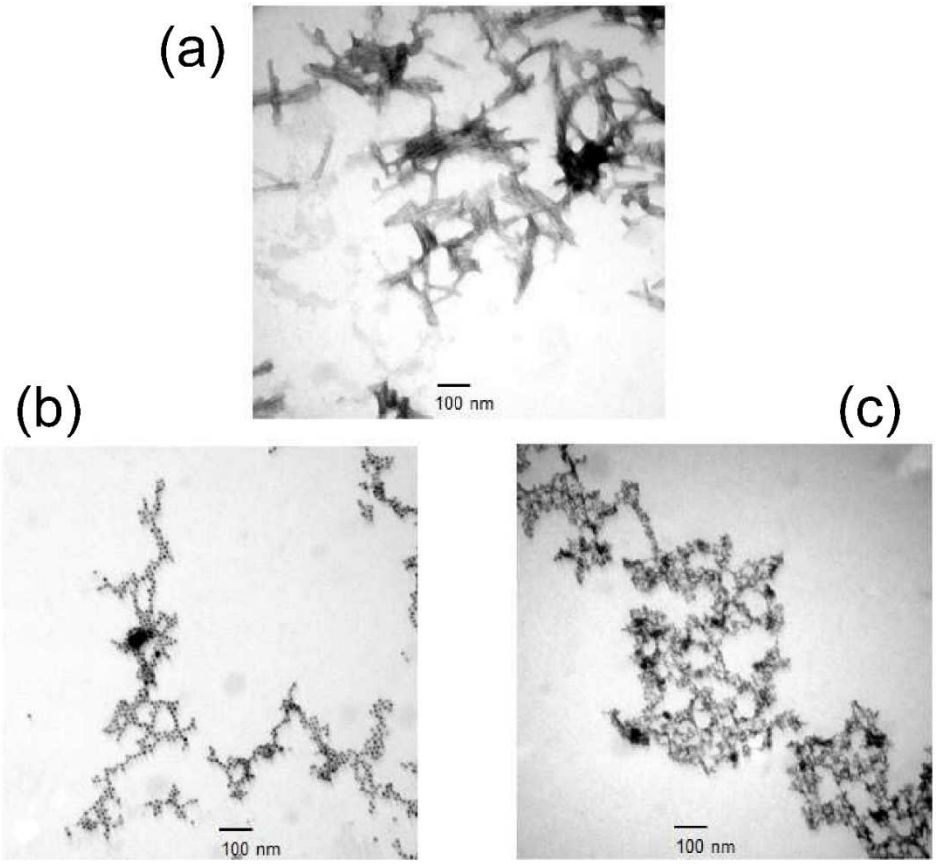

Figure 4.31. TEM micrographs of 20 μM D76N β2m incubated under fibrillogenic conditions a) in the absence of Cit-AuNPs, b) and c) in presence of Cit-AuNPs. Fibres are massively present in a), totally absent in b) and c). The aggregate observed in c) was not fibrillar although it may be ThT positive.

In presence of Cit-AuNPs, within the nanoparticle patches, there seems to be an amorphous protein agglomerate (Figure 4.31 c) whose nature escapes direct determinations.

In order to clarify the observed inhibition phenomenon, a soluble fraction analysis by native agarose gel electrophoresis was undertaken. (Figure 4.32).

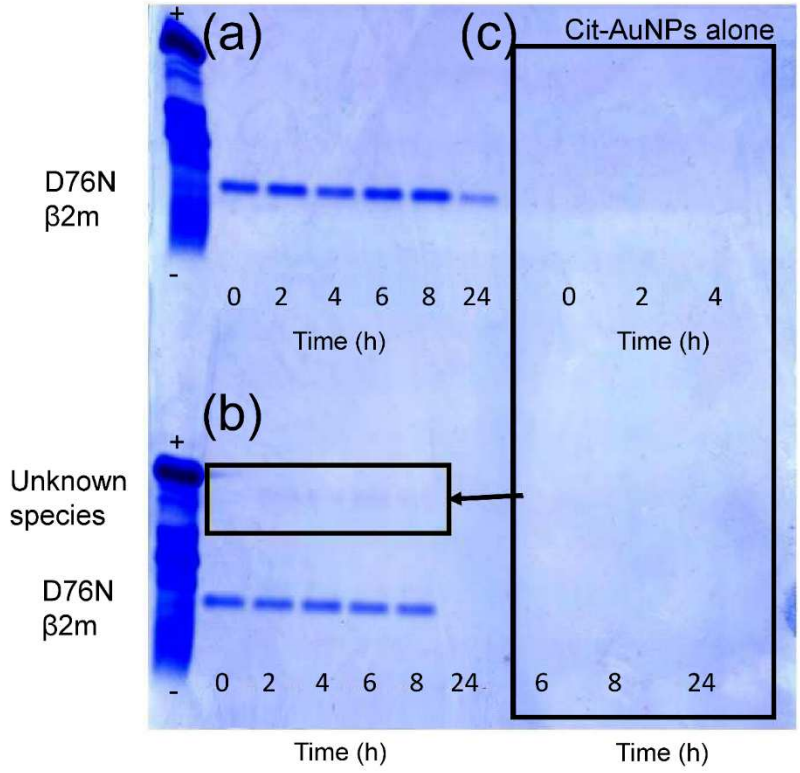

Figure 4.32. Native agarose gel electrophoresis of 20 μM D76N β2m exposed to fibrillogenic conditions a) without Cit-AuNPs and b) with Cit-AuNPs, at different incubation times. Gels were stained with Coomassie blue. The band corresponding to the second species appearing in the presence of Cit-AuNPs is highlighted by a black box. c) Native agarose gel electrophoresis of Cit-AuNPs alone.

A lower amount of soluble protein can be noticed from the very beginning in presence of Cit-AuNPs, when no aggregation had yet occurred according to Figure 4.30. Electrophoresis analysis was preceded by a centrifugation step during which most of the NPs precipitated out of the solution, dragging out also protein material, as confirmed also by UV control of the supernatant. This happened even under static, i.e. non-fibrillogenic, conditions with the loss of 40-50% of the initially incubated protein, in comparison with the same sample without Cit-AuNPs when submitted to

centrifugation, as determined both from band intensity of native agarose gel electrophoresis (Figure 4.33 b) and UV assay on supernatant.

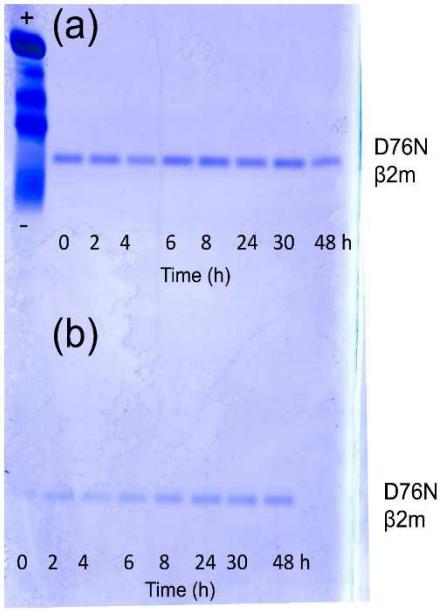

Figure 4.33. Native agarose gel electrophoresis of 20 μM D76N β2m under non-fibrillogenic conditions, i.e. no agitation, a) without Cit-AuNPs and b) with Cit-AuNPs, at different incubation times. The loss of protein in presence of Cit-AuNPs can be observed also in non-fibrillogenic conditions: the amount of free protein is lower if it is incubated with Cit-AuNPs (b) with respect to the control (a). In addition, the second species detected in presence of Cit-AuNPs when the protein is exposed to fibrillogenic conditions (see Figure 4.32 b) is absent.

In both samples, a progressive reduction of monomeric D76N β2m band density suggests protein aggregation (Figure 4.32 a and b). Moreover, native gel electrophoresis showed in presence of Cit-AuNPs the appearance after two hours of another species with different electrophoretic mobility in comparison with the monomer (Figure 4.32 b). The existence of this species was linked both to fibrillogenic conditions, i.e. agitation at neutral pH of D76N β2m, and Cit-AuNP presence. However, it invariably disappeared in conjunction with the monomeric species (Figure 4.32 b). The corresponding electrophoretic band can not be ascribed to electrophoretic migration of Cit-

AuNPs because these NPs are negative to Coomassie staining (Figure 4.32 c). In addition, the unknown species with low electrophoretic mobility were present even after the complete precipitation of Cit-AuNPs by prolonged centrifugation (Figure 4.34 d), as confirmed by UV-Vis.

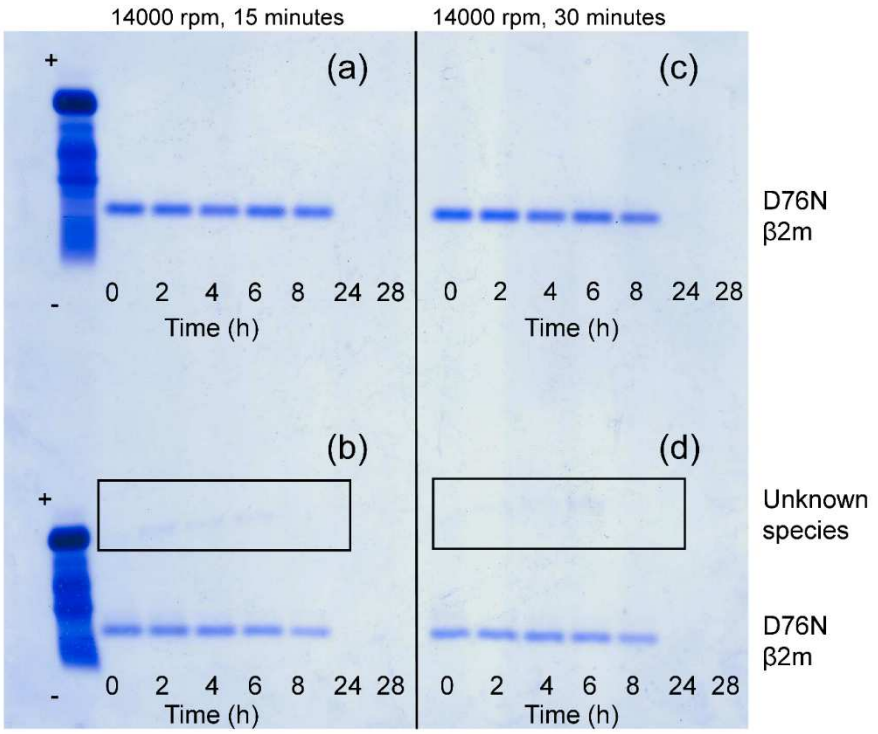

Figure 4.34. Native agarose gel electrophoresis of 20 μM D76N β2m incubated under fibrillogenic conditions: a) and c) without Cit-AuNPs and b) and d) with Cit-AuNP. The gels reported in c) and d) were run after long centrifugation (14000 rpm, 30 minutes) that ensures complete precipitation of Cit-AuNPs, as checked by UV-Vis. Even in d) the presence of the unknown species (boxed in black) can be appreciated, confirming the absence of nanoparticles in this species.

All the evidence then pointed to an oligomeric/aggregated protein species that was stabilized by the presence of Cit-AuNPs and did not affect the fibrillogenesis pattern.

By expressing the protein precipitation kinetics as complementary loss percentage, it was found that the rate of monomeric protein disappearance was independent of the presence of Cit-AuNPs (Figure 4.35).

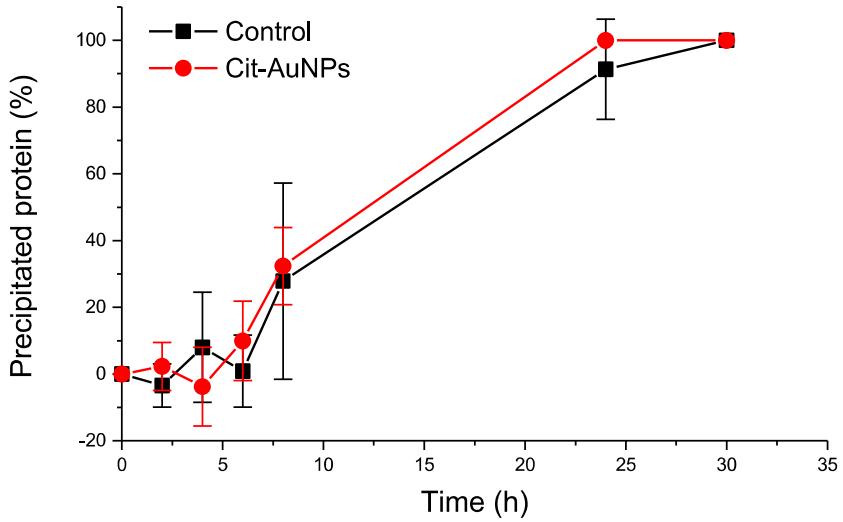

Figure 4.35. Precipitation kinetics measured by densitometric analysis of the bands in native agarose gel electrophoresis of the control (black) and the sample incubated with the Cit-AuNPs (red). The reported values were normalized by considering the respective band density at Time = 0. The experiment was done in triplicate and the errors are the standard deviations.

The substantial identity of the kinetic profiles suggests that the inhibition of D76N β2m fibrillation, supported by ThT assay and TEM, arose from the competition of the Cit-AuNPs interaction with the protein fibrillation pathway. Furthermore, it was found that the extent of inhibition depended on the protein/NP ratio (Figure 4.36). On increasing the protein concentration with a fixed concentration of Cit-AuNPs, the amount of protein that underwent fibrillogenesis raised. This can be explained considering the progressive saturation of the interaction sites onto the Cit-AuNP surface. At increasing protein concentration, only a progressively smaller percentage of the protein can interact with Cit-AuNPs thereby avoiding the fibrillation, whereas a progressively larger percentage remains available for fibrillogenesis. However, the percentage of the protein that does not fibrillate (e.g. 50% for 20 μM D76N) is higher than the percentage of the protein that would be tightly bound in a layer surrounding a Cit-AuNP (e.g. 5-10% for 20 μM D76N), confirming that protein molecules rapidly exchange on NP surface and that Cit-AuNPs are able to spread their effect also to a

significative amount of the bulk proteins, as observed from NMR and QCMD experiments too.

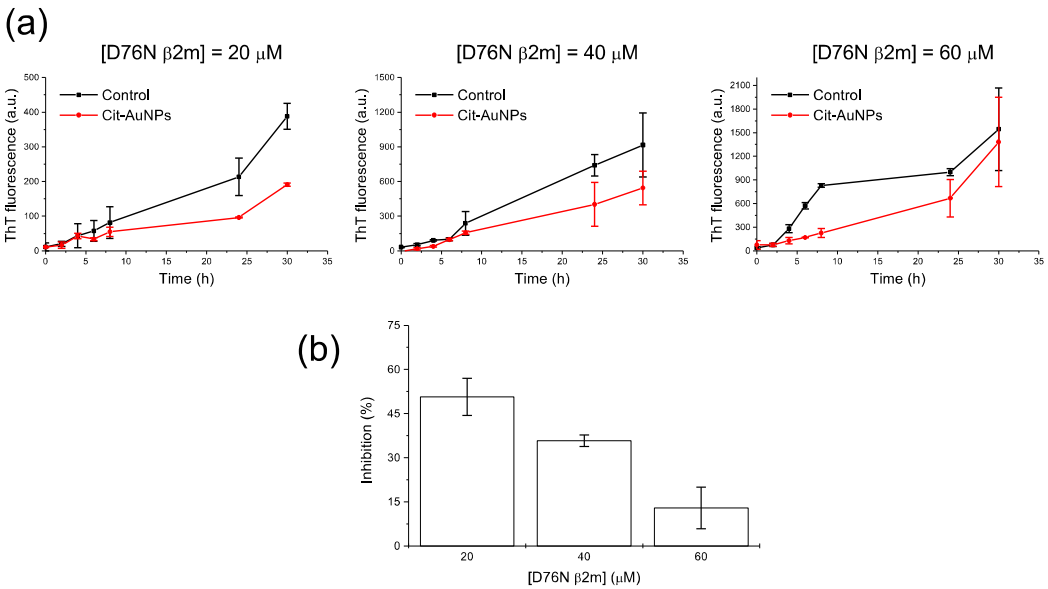

Figure 4.36. a) ThT-based monitoring of D76N β2m fibrillogenesis at varying protein concentrations in the absence (black) and presence of ~ 25 nM Cit-AuNPs (red) and b) bar plot representing the inhibitory capability of Cit-AuNPs at different protein concentrations measured considering the ThT assays results. All measurements were always performed in triplicate.

4.3 β2m wild-type interaction pattern with differently capped AuNPs

The capability of hampering β2m fibrillation exhibited by Cit-AuNPs contrasts with previous findings in which other nanoparticles such as polymeric, acrylamide-based nanoparticles, cerium oxide nanoparticles, quantum dots and carbon nanotubes were found to promote β2m fibrillogenesis.[85] The contrasting results obtained with different nanoparticles on β2m amyloid formation suggest that by fine tuning the physico-chemical properties of nanoparticles it is possible to achieve different, if not opposite, effects. As a proof of concept, the effect of different AuNP properties on β2m wild-type interaction pattern was investigated. To this aim negatively charged with different dimensions and positively charged alkanethiolate coated-AuNPs (AT-AuNP) were synthesized. 6-mercaptohexanoic acid (MHA) was used to produce 7.5 nm AuNPs covered by a negative alkanethiol, whereas 3-mercaptopropionic acid (MPA) was employed to synthesize smaller (3.6 nm diameter) negatively charged AuNPs. To synthesize positively charged AuNPs, (11-mercaptoundecyl)-N,N,N-trimethylammonium bromide (MUTAB) was used as ligand. For the considerations about the AuNP synthesis and related procedures see Section 3.1. MHA-AuNPs and MUTAB-AuNPs do not differ only because of the charge, but also the alkyl chain length is different, i.e. 6 and 11 carbon atoms, respectively. Unfortunately, at the moment in which these experiments were undertaken, no longer ω-carboxy alkanethiols or shorter ω-trimethylammonium alkanethiols were commercially available.

4.3.1 Alkanethiolate-AuNPs stability in presence of β2m

AT-AuNP solutions were found to be stable, but β2m addition decreased their colloidal stability leading to precipitation.

When MHA-AuNPs were mixed with the protein solution (protein/NP = 600), during the first days no apparent agglomeration was observed. It was possible to titrate AuNPs with the protein and to follow the SPR red shift, as for Cit-AuNPs (Figure 4.37).

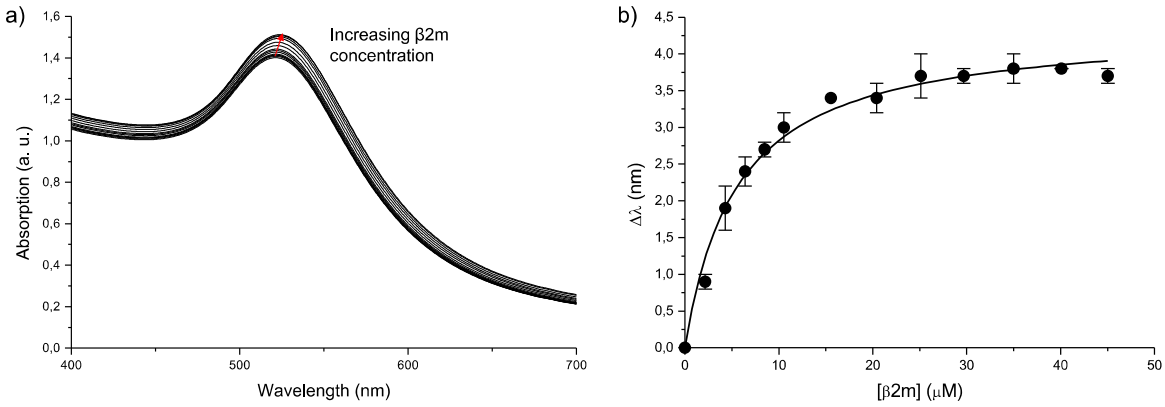

Figure 4.37. a) MHA-AuNP absorption spectra after the progressive addition of β2m (0 - 45 μM) and b) the corresponding SPR red shift as a function of the protein concentration fitted with Langmuir equation (black line).

The fitting of the SPR shift with the Langmuir adsorption isotherm gave an association constant (K_a) value of (0.18 ± 0.018) x 10^6. This value is lower than the one obtained with Cit-AuNPs, i.e. (3.33 ± 0.53) x 10^6. It is worth stressing that we are dealing with a different AuNP system in which the distance between the protein and the gold surface is higher due to the presence of the alkanathiolate shell. Gold plasmon response to protein adsorption is probably affected by the alkanethiolate layer and the direct comparison of the association constant values could not be considered a proper way to compare the strength of the interaction.

After one month, a black precipitate was found on the bottom of the flask. The nearly complete precipitation of MHA-AuNPs was confirmed by

UV-Vis spectroscopy (Figure 4.38 a). This phenomenon was attenuated in the sample in which the protein concentration was kept the same, but the NP concentration was two-fold. In this latter solution, AuNPs did not precipitate completely, but slowly settled (Figure 4.38 b).

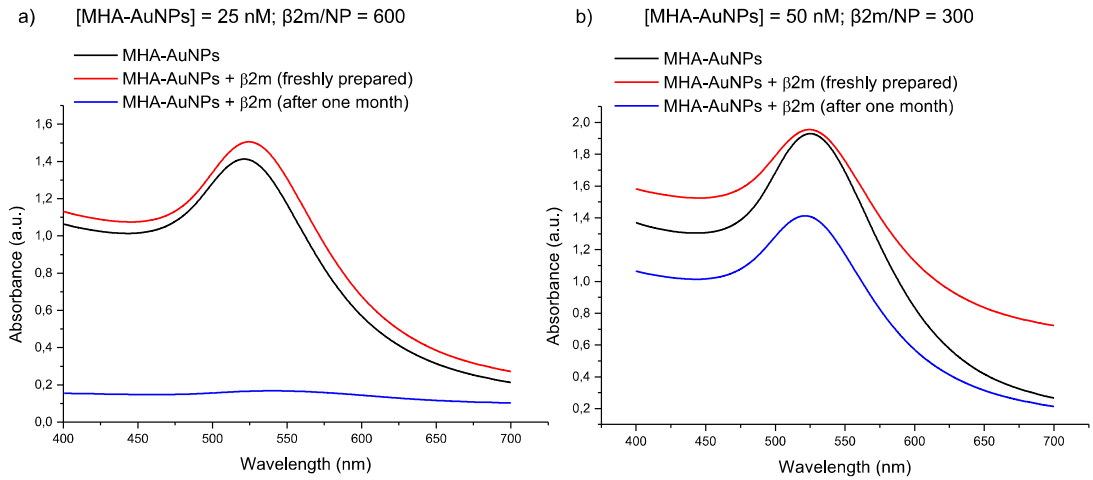

Figure 4.38. a) Absorption spectra of 25 nM MHA-AuNPs alone (black) and in the presence of 15 μM β2m soon after the solution preparation (red) and after one month (blue). b) Absorption spectra of 50 nM MHA-AuNPs alone (black) and in the presence of 15 μM β2m soon after the solution preparation (red) and after one month (blue).

The MHA-AuNP precipitate formed after one month in presence of β2m was briefly sonicated and deposited on a TEM grid for imaging. TEM micrographs showed an agglomerated state of nanoparticles clearly embedded in a protein matrix represented by a grey halo (Figure 4.39 a and b). With the lower protein/NP ratio sample, this protein matrix was less evident, but big NP aggregates could still be observed (Figure 4.39 c).

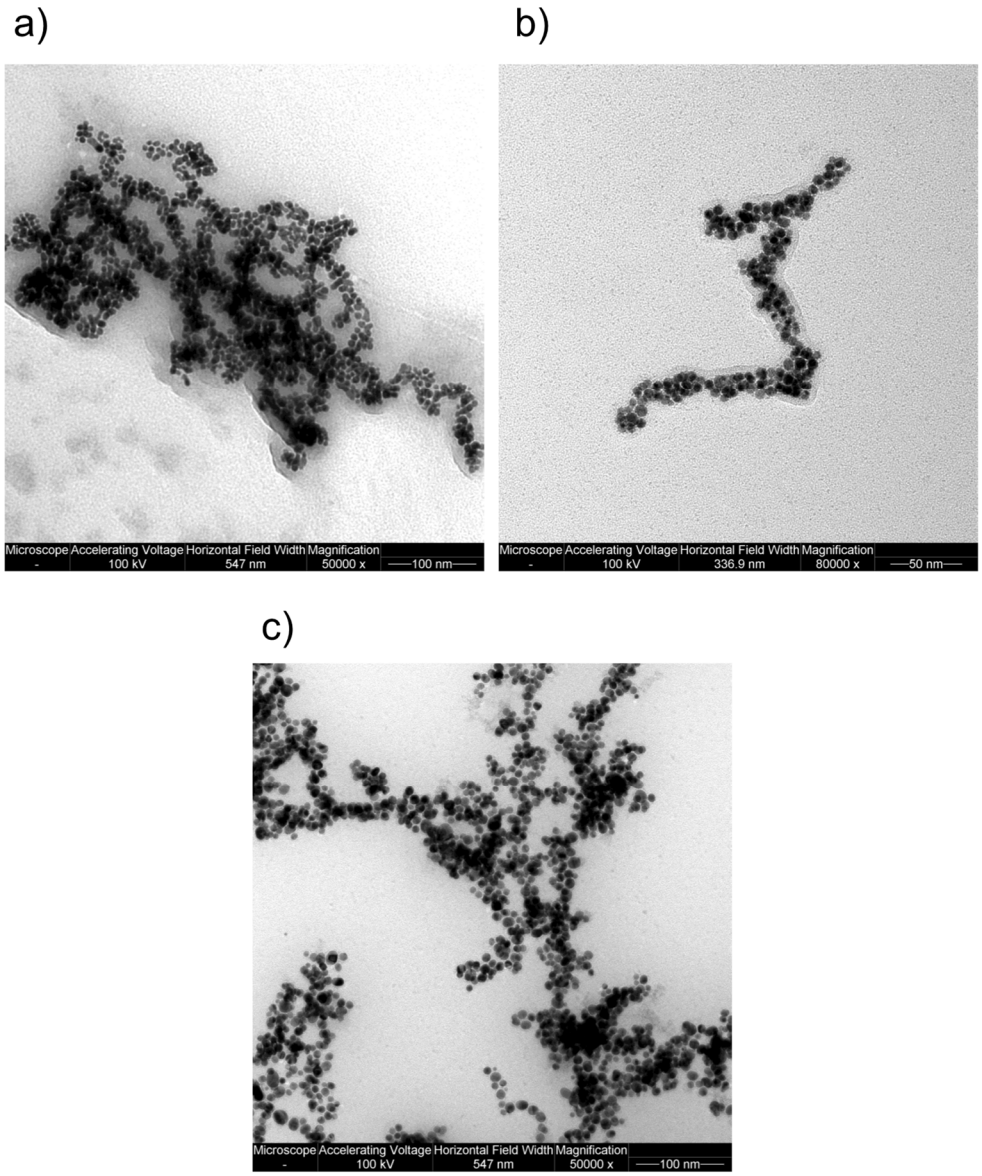

Figure 4.39. a) TEM micrograph of sonicated precipitate made by 25 nM MHA-AuNPs and 15 μM β2m; b) TEM micrograph of sonicated precipitate made by 25 nM MHA-AuNPs and 15 μM β2m stained with uranyl acetate and c) TEM micrograph of 50 nM MHA-AuNPs in the presence of 15 μM β2m.

The same NP destabilising effect of the protein was observed with MUTAB-AuNPs, but in a more accentuated extent. Soon after the preparation of protein-NP solutions, the MUTAB-AuNP less concentrated solution started to aggregate and the more concentrated solution started to settle as can be seen in the UV-Vis spectra (Figure 4.40).

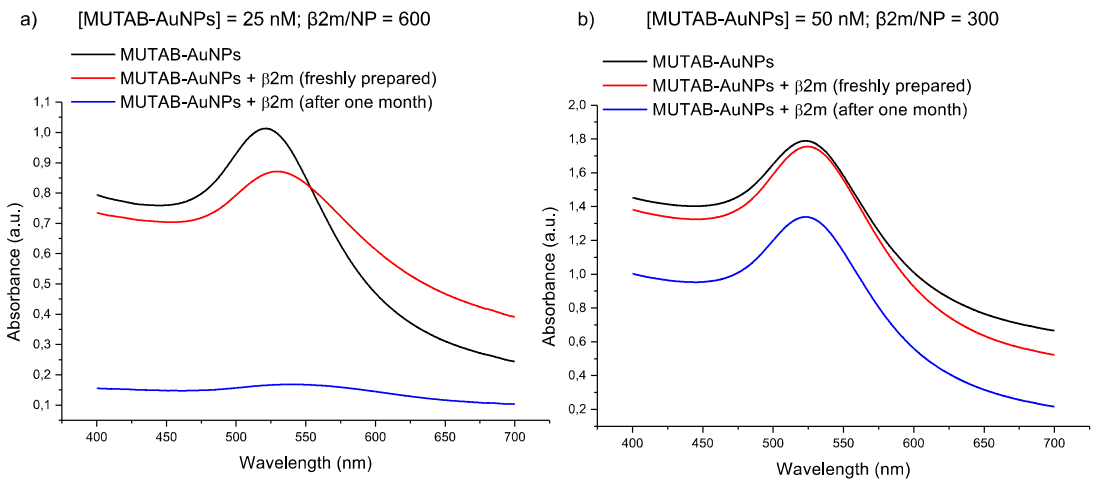

Figure 4.40. a) Absorption spectra of 25 nM MUTAB-AuNPs alone (black) and in the presence of 15 µM β2m soon after the solution preparation (red) and after one month (blue). b) Absorption spectra of 50 nM MHA-AuNPs alone (black) and in the presence of 15 µM β2m soon after the solution preparation (red) and after one month (blue).

The sudden nanoparticle agglomeration can be easily followed with UV-Vis by titrating AuNPs with the protein. The subsequent addition of protein led to progressive broadening reflecting the aggregation that occurred in solution (Figure 4.41).

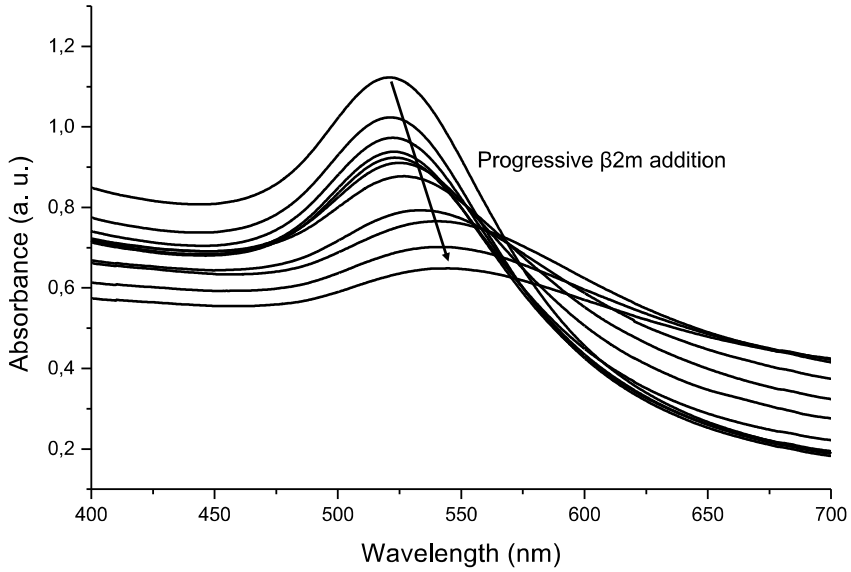

Figure 4.41. MUTAB-AuNP UV-Vis spectra after the progressive addition of β2m from 0 to 40 µM.

TEM images of sonicated precipitate made by 25 nM MUTAB-AuNPs and 15 μM β2m showed nanoparticle agglomerates, but even if the sample was stained with uranyl acetate, no distinctive evidence of protein presence inside these agglomerates could be detected (Figure 4.42 a). In the more concentrated sample the scenario is very similar to the one found with MHA-AuNPs. In this case a grey halo that is usually attributed to the protein can be noticed among the nanoparticles (Figure 4.42 b).

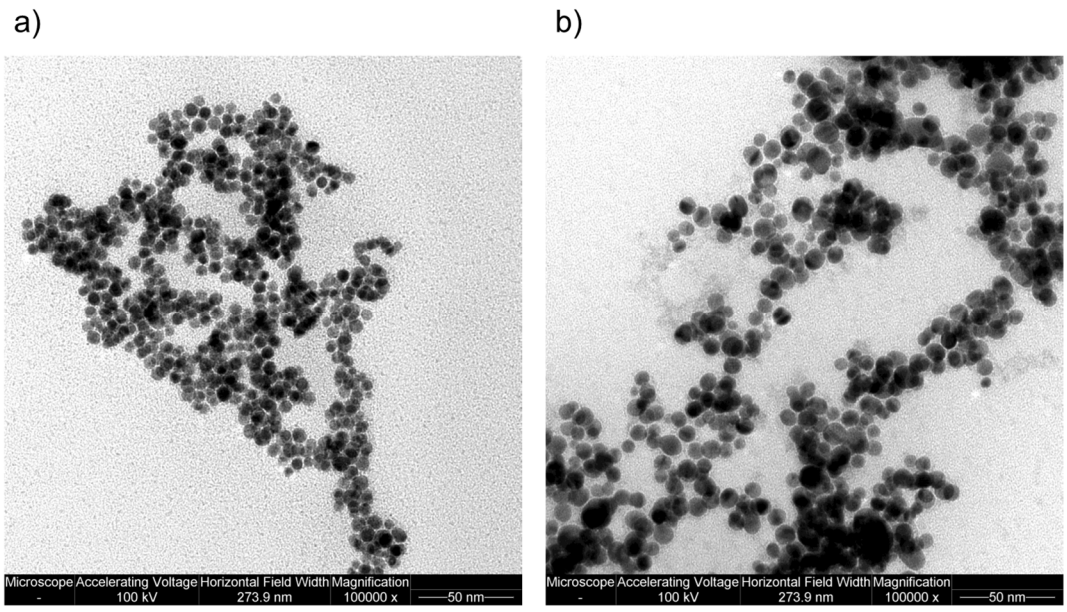

Figure 4.42. a) TEM micrograph of sonicated precipitate made by 25 nM MUTAB-AuNPs and 15 μM β2m stained with uranyl acetate and b) TEM micrograph of 50 nM MHA-AuNPs in the presence of 15 μM β2m.

While MHA-AuNPs and MUTAB-AuNPs underwent an irreversible precipitation into black pellets upon protein addition, MPA-AuNPs precipitated within few hours, but the brownish precipitate could be easily dispersed again. The small size of MPA-AuNPs did not allow to follow NP-protein interaction by UV-Vis spectroscopy. TEM images of the sonicated MPA-AuNP precipitate did not show nanoparticle aggregation, indeed the sample appeared well dispersed (Figure 4.43).

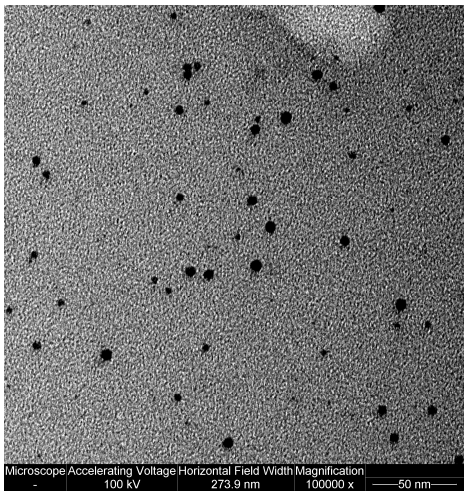

Figure 4.43. a) TEM micrograph of 2,5 μM MPA-AuNPs and 25 μM β2m.

4.3.2 β2m characterization in presence of AT-AuNPs

To understand what happened to β2m in presence of AT-AuNPs, UV-Vis spectroscopy could not be used. AuNPs are known to absorb strongly at 280 nm and even if they are almost all precipitated there can be still a NP contribution that is very hard to remove. Moreover, during incubation with β2m NP, agglomerate and the absorbance of the aggregates could be different from the one of the solution without the protein.

The fate of β2m was investigated by two-dimensional NMR without any AuNP interference. The ^{1}H ^{15}N SOFAST HMQC spectrum of β2m recorded in presence of MHA-AuNPs (protein/NP = 600) showed a decrease of intensity when compared to the control (RI_{av} = 0.81 ± 0.13) (Figure 4.44 c) and the loss of the whole ensemble of protein ^{15}N-^{1}H correlations after one month (Figure 4.45 a). It is worth highlighting that SOFAST experiments are very convenient to screen quickly the appearance of the two-dimensional NMR spectra, but they have a lower signal-to-noise ratio compared to HSQC which leads to a higher uncertainty on the intensity measurement. The quite high uncertainty on intensity measurement (8,1%) of the spectrum recorded in presence of MHA-AuNPs limits the confidence threshold for some of the observed changes, e.g. all the values above unit.

The intensity decrease dropped to 0.46 ± 0.092 at higher MHA-AuNP concentration (protein/NP = 300) (Figure 4.44 e).

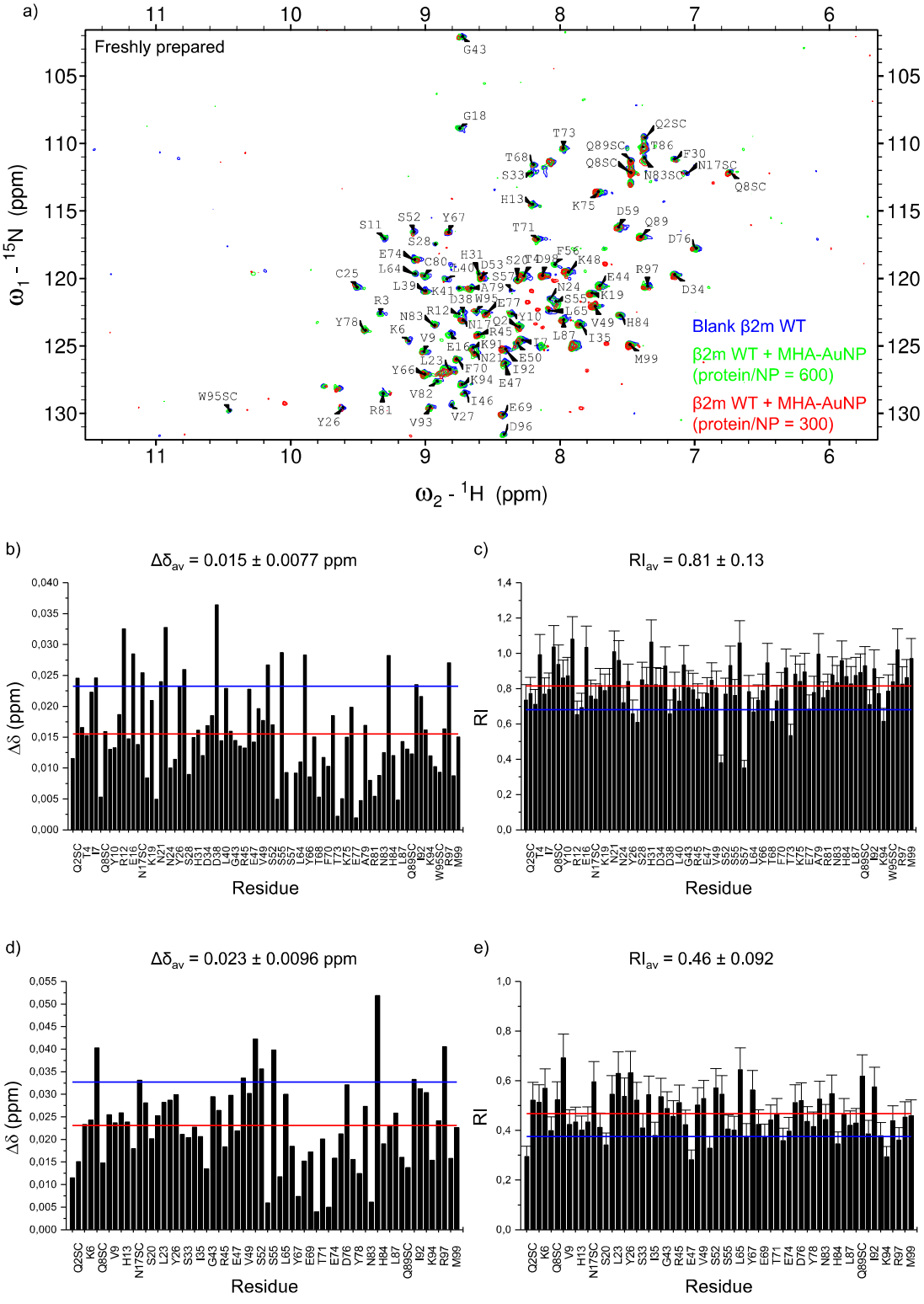

Figure 4.44. a) Superimposition of β2m WT ^{15}N-^{1}H HSQC spectra recorded at 500 MHz without (blue) and with MHA-AuNP (protein/NP = 600 in green and protein/NP = 300 in red). The corresponding backbone amide assignments are reported by single letter code and side chain amides are indicated with SC. b) and c) Bar plots of amide chemical shift perturbations (Δδ) and cross-peak attenuations (RI), respectively, when protein/NP = 600. d) and e) Bar plots of amide chemical shift perturbations (Δδ) and cross-peak attenuations (RI), respectively, when protein/NP = 300. The horizontal lines indicate the average values (red) and the displacement of one standard deviation (blue) above and below the average, respectively. To avoid graphic crowding, the abscissa labels of the panels were reported only every other three signals. Besides the observed backbone amides, also the following detected side-chain (SC) NH resonances were included in the abscissa label list, according to the primary sequence order: Q2, Q8*, N17, N83, Q89, W95, where the asterisk indicates the inclusion of two separate resonances for asparagine and glutamine side-chain amides. The missing labels do not include the following unobserved or non-existing backbone NH connectivities: I1, P5, Q8, P14, A15, F22, G29, P32, E36, V37, N42, H51, L54, K58, W60, S61, F62, Y63, P72, V85, S88, P90. In addition to the listed residues, in the spectrum of the solution with a higher NP concentration also R3, S11, R12, N24, V27, S28, H31, D38, L40, K41, F56, S57, L64, C80, R81, V82 and D96 were unobservable.

In the sample in which MHA-AuNPs were more concentrated, 24% of the signals disappeared and new peaks in the random coil region appeared suggesting a partial loss of tertiary structure due to local unfolding (Figure 4.44 a). This denaturation effect extended essentially over the whole molecule after one month (Figure 4.45 b).

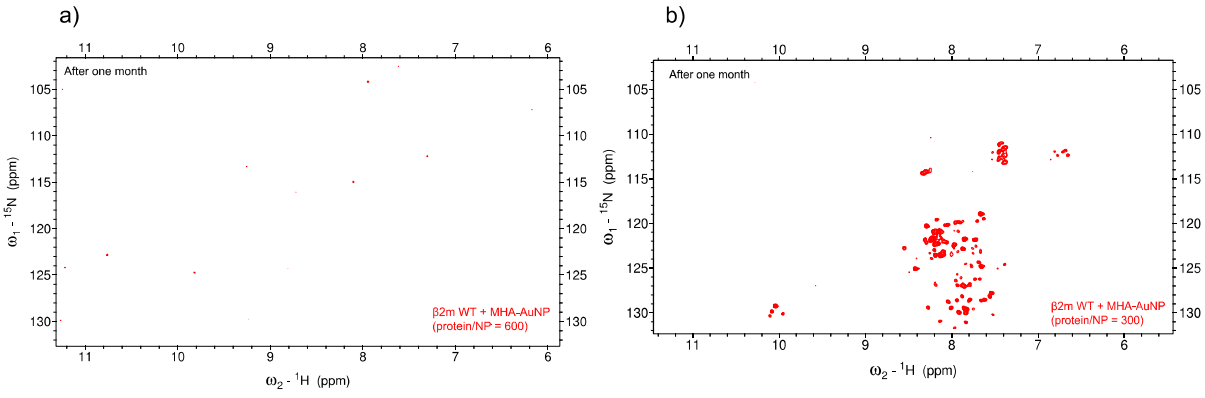

Figure 4.45. SOFAST HMQC spectrum recorded at 500 MHz of β2m WT incubated for one month with MHA-AuNP at a) protein/NP = 600 and b) protein/NP = 300.

At both protein/NP ratios, the intensity decrease was not uniformly distributed along the protein backbone, but there were some signals that

proved more affected by the NP presence (Figure 4.44 c and e). In addition to this attenuation pattern, a significant average chemical shift variation ($\Delta\delta_{av}$ = 0.015 ± 0.0077 ppm for protein/NP = 600 and $\Delta\delta_{av}$ = 0.023 ± 0.0096 ppm for protein/NP = 300) was observed (Figure 4.44 b and d). The most perturbed signals, i.e. relative intensity and chemical shift perturbation outliers, did not belong to residues clustering in restricted regions, but to locations rather spread over the protein structure, involving strands on both β-sheets and AB loop apical region (Figure 4.46).

a)

Structure region	Δδ outliers β2m/NP = 600	RI outliers β2m/NP = 600	Δδ outliers β2m/NP = 300	RI outliers β2m/NP = 300
N-term, A strand	I7		I7	
AB loop	R12, E16, N17SC	R12	N17SC	S20
B strand	N21SC, L23, V27	Y26, V27	L23	Y26
BC loop				
CC', C'D loops	D38	D38	K48	E47
D strand	E50	E50	E50, S52	E50
DE loop	S55	S57	S55	
E strand	L65	L64, T68	L65	T68
EF loop		T73		T73, E69
F strand	H84		N83SC, H84	H84
FG loop				
G strand, C-term	K91, R97	K94	K91	K94

b)

c)

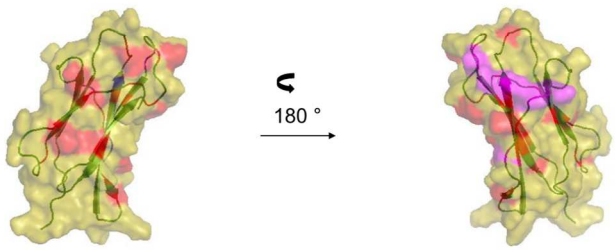

Figure 4.46. a) Synopsis of β2m WT positions that proved most affected, i.e. displaced more than one standard deviation from the average, by the presence of MHA-AuNP and their secondary structure element location. b) and c) β2m WT cartoon highlighting in red the locations of the outlier residues already present when protein/NP = 600 and in magenta the additional ones revealed when protein/NP = 300.

When MUTAB-AuNPs were mixed with β2m in a ratio of 1 to 600, the two-dimensional spectrum did not show overall significant intensity variations (RI_{av} = 1.01 ± 0.093) and only small chemical shift deviations ($\Delta\delta_{av}$ = 0.0047 ± 0.029 ppm) could be detected (Figure 4.47 b and c). Although the average intensity and chemical shift variations were small, there were residues that resulted more affected by the presence of MUTAB-AuNPs. In addition to the apical loops (AB, BC, DE and EF), also some residues belonging to B, D and E β-strands presented significant perturbations (Figure 4.48 a and b). These values do not change significantly after one month.

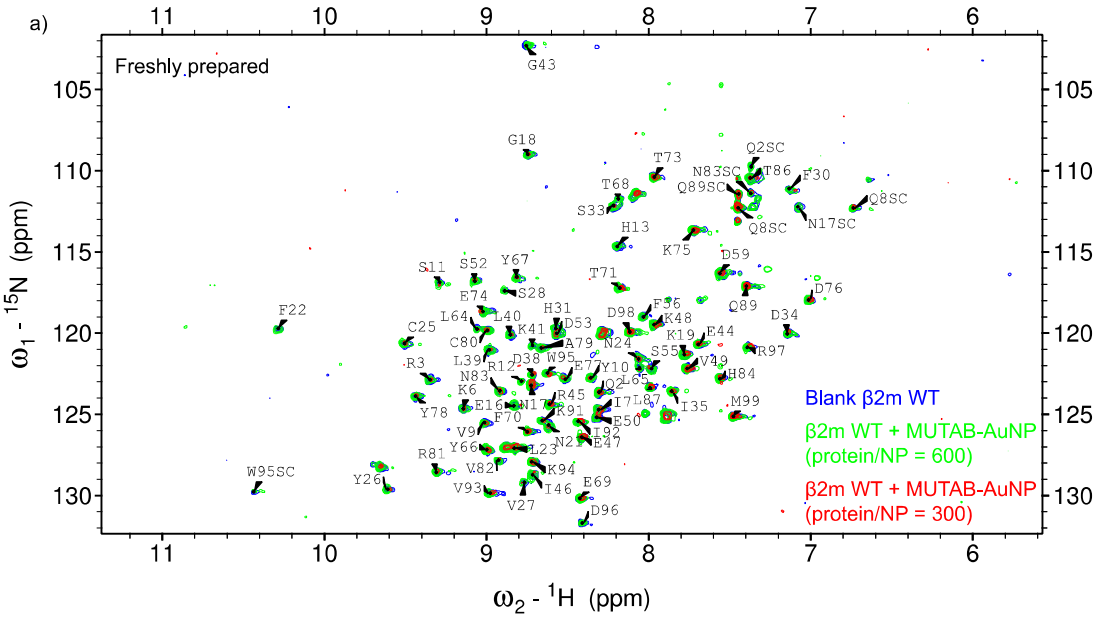

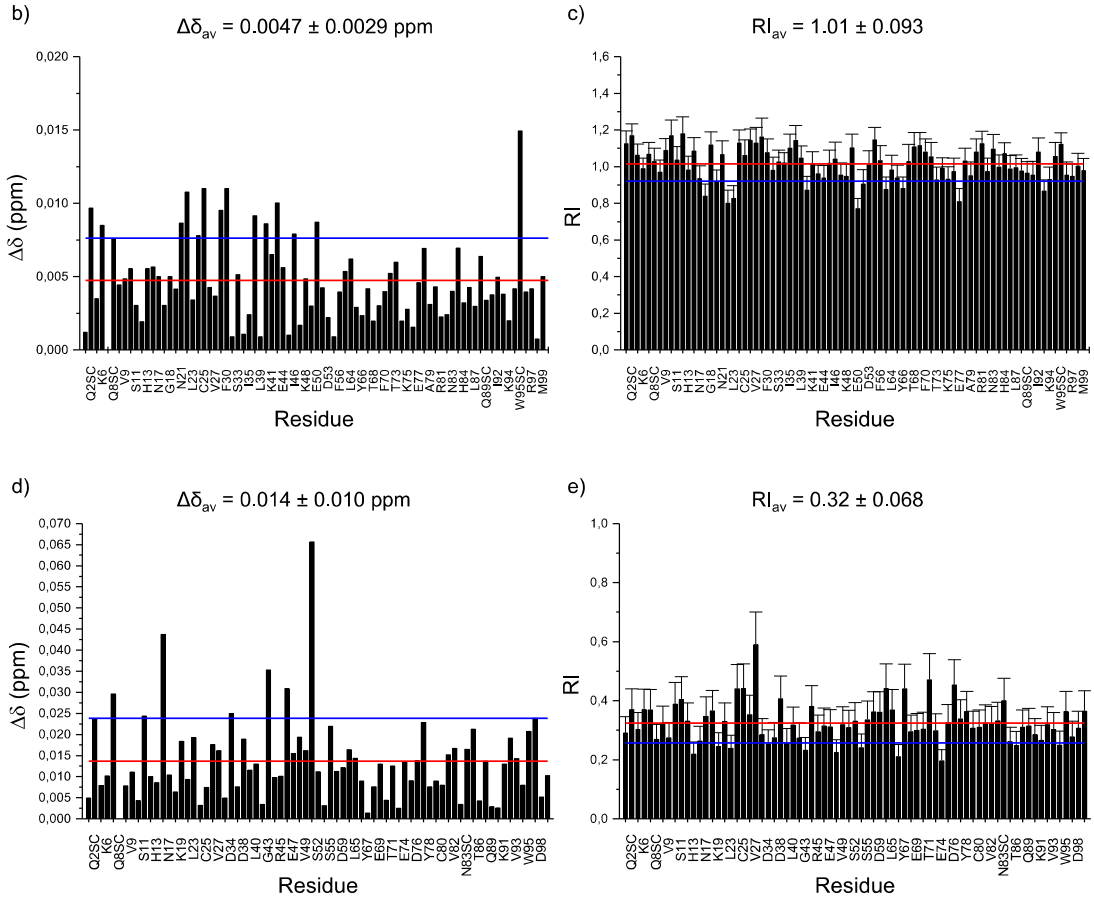

Figure 4.47. a) Superimposition of β2m WT ^{15}N-^{1}H HSQC spectra recorded at 500 MHz without (blue) and with MUTAB-AuNP (protein/NP = 600 in green and protein/NP = 300 in red). The corresponding backbone amide assignments are reported by single letter code and side chain amides are indicated with SC. b) and c) Bar plots of amide chemical shift perturbations (Δδ) and cross-peak attenuations (RI), respectively, when protein/NP = 600. d) and e) Bar plots of amide chemical shift perturbations (Δδ) and cross-peak attenuations (RI), respectively, when protein/NP = 300. The horizontal lines indicate the average values (red) and the displacement of one standard deviation (blue) above and below the average, respectively. To avoid graphic crowding, the abscissa labels of the panels were reported only every other three signals. Besides the observed backbone amides, also the following detected side-chain (SC) NH resonances were included in the abscissa label list, according to the primary sequence order: Q2, Q8*, N17, N83, Q89, W95, where the asterisk indicates the inclusion of two separate resonances for asparagine and glutamine side-chain amides. The missing labels do not include the following unobserved or non-existing backbone NH connectivities: I1, T4, P5, Q8, P14, A15, S20, G29, P32, E36, V37, N42, H51, L54, S57, K58, W60, S61, F62, Y63, P72, V85, S88, P90. In addition to the listed residues, in the spectrum of the solution with a higher NP concentration also F22, S28, F30, H31 and D96 were unobservable.

When the protein/NP ratio was decreased, the average relative intensity decreased to 0.32 ± 0.068 and the average chemical shift perturbation raised to 0.014 ± 0.010 ppm (Figure 4.47 d and e). As the nanoparticle concentration increased, the protein spectrum revealed a quite strong interaction affecting mainly the apical region including the C-terminal portion (C-terminal tail, AB and EF loops) and the C-C'-D loop (Figure 4.48 a and c).

a)

Structure region	Δδ outliers β2m/NP = 600	RI outliers β2m/NP = 600	Δδ outliers β2m/NP = 300	RI outliers β2m/NP = 300
N-term, A strand			I7, S11	
AB loop		N17SC, K19	E16	H13, K19
B strand	F22, C25	F22, L23		L23
BC loop	F30		D34	D34
CC', C'D loops		L40	G43, I46	G43
D strand		E50	E50	K48
DE loop		S52, D59		D53
E strand		Y66		
EF loop		E77		E74
F strand				
FG loop				T86
G strand, C-term	W95SC	V93	R97	K94

b)

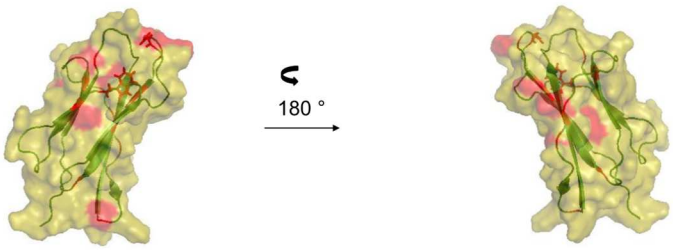

c)

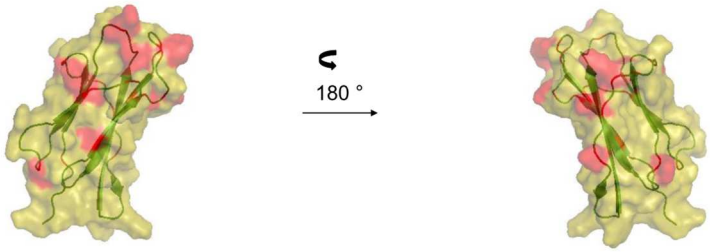

Figure 4.48. a) Synopsis of β2m WT positions that proved most affected, i.e. displaced more than one standard deviation from the average, by the presence of

MUTAB-AuNP and their secondary structure element location. b) and c) β2m WT cartoon highlighting in red the locations of the outlier residues reported in a) for protein/NP = 600 and protein/NP =300, respectively.

Differently with respect to the other AuNPs examined in this work, MPA-AuNPs could be dried and dispersed without any aggregation onset, thereby allowing for very high NP concentrations. Five different protein/NP ratios were examined going from 100 to 10. If the same geometrical considerations done for Cit-AuNPs in Section 4.1.1 are applied to 3.6 nm MPA-AuNPs, a minimum of 14 and a maximum of 50 proteins, approximately, can be adsorbed on their surface. In the HMQC spectra, in addition to a preferential intensity decrease, there was also an overall attenuation (Figure 4.49 c) reflecting the increase of protein recruitment by the increasing number of available interaction sites on NPs.

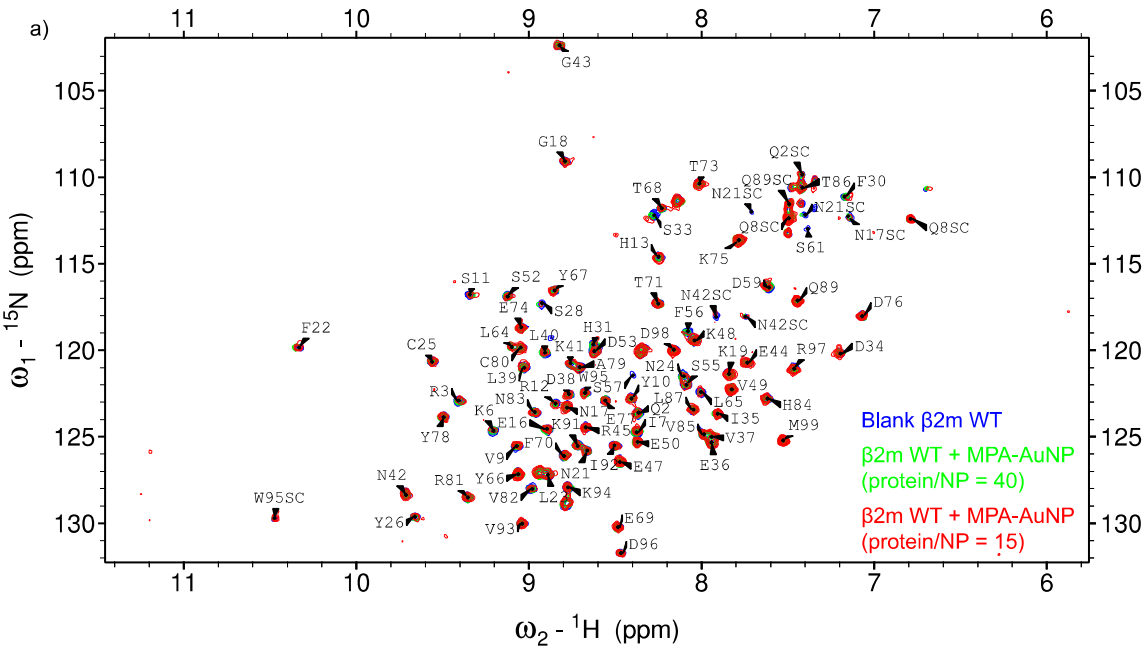

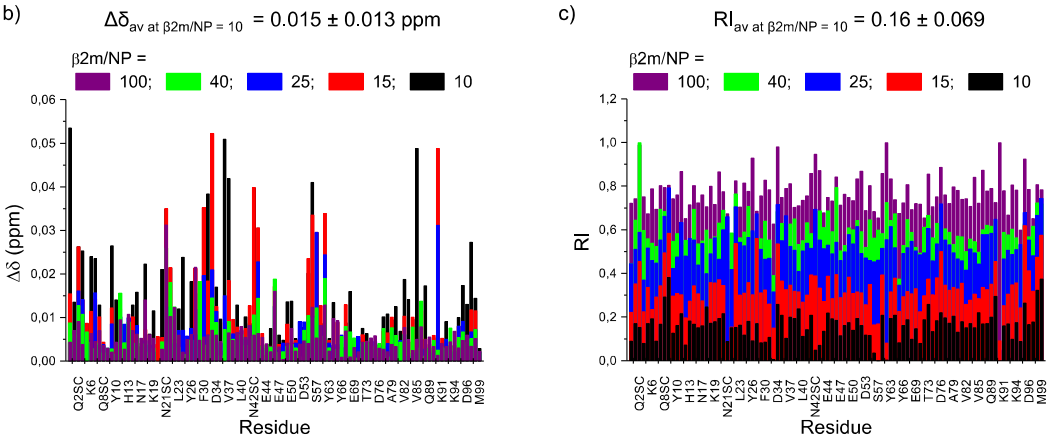

Figure 4.49. a) Superimposition of β2m WT ^{15}N-^{1}H HSQC spectra recorded at 500 MHz without (blue) and with MPA-AuNP (protein/NP = 40 in green and protein/NP = 15 in red). The corresponding backbone amide assignments are reported by single letter code and side chain amides are indicated with SC. b) and c) Bar plots of amide chemical shift perturbations (Δδ) and cross-peak attenuations (RI), respectively. Refer to color legend for the protein/NP ratios. To avoid graphic crowding, the abscissa labels of the panels were reported only every other three signals. Besides the observed backbone amides, also the following detected side-chain (SC) NH resonances were included in the abscissa label list, according to the primary sequence order: Q2, Q8*, N17, N21*, N24*, N42*, N83*, Q89*, W95, where the asterisk indicates the inclusion of two separate resonances for asparagine and glutamine side-chain amides. The missing labels do not include the following unobserved or non-existing backbone NH connectivities: I1, P5, P14, G29, P32, L54, K58, D59, W60, F62, P72, S88, and P90.

The gradual intensity attenuation was associated with progressive chemical shift variation (Figure 4.49 b).

With these small negatively charged NP, a much more specific and localized region was found to be perturbed (Figure 4.50). The patch involved two loops, namely BC loop (F30, H31, S33) and DE loop (S55, F56, S55, D59/W60 and S61) and the spatially close N-terminal tail (Q2 and R3). It was not possible to fit chemical shift perturbation data with a binding isotherm because the signals that showed the highest deviations were also the ones undergoing extensive attenuation up to complete cancellation in the first titration points.

a)

Structure region	Δδ outliers	RI outliers
N-term, A strand	R3	R3
AB loop		
B strand		S28
BC loop	F30, H31, S33	F30, H31, S33
CC', C'D loops	E36, V37	
D strand		
DE loop	S55, F56, S57, S61	F56, S57, S61
E strand		L65
EF loop		
F strand		
FG loop		
G strand, C-term		

b)

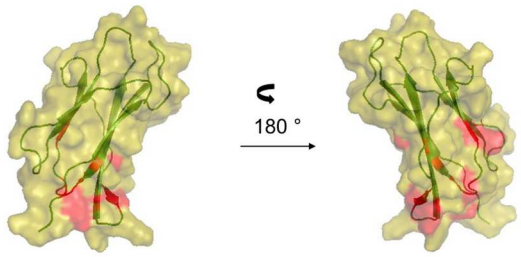

Figure 4.50. a) Synopsis of β2m WT positions that proved most affected, i.e. displaced more than one standard deviation from the average, by the presence of MPA-AuNPs and their secondary structure element location. b) β2m WT cartoon highlighting in red the locations of the residues reported in a).

4.3.3 Fluorescence study of β2m in presence of AT-AuNPs

From NMR results it can be inferred that, at least at the higher protein/NP ratios, while the negatively charged MHA-AuNPs are able to considerably affect β2m conformation, the positively charged MUTAB-AuNPs leave the protein almost unperturbed. To further verify this conclusion, fluorescence experiments were performed. First of all, β2m intrinsic fluorescence trend with AT-AuNP concentration was different from that observed with Cit-AuNPs. With MHA-AuNPs, after an initial decrease (around 20%), the fluorescence intensity increased and the emission peak shifted (Figure 4.51 a).

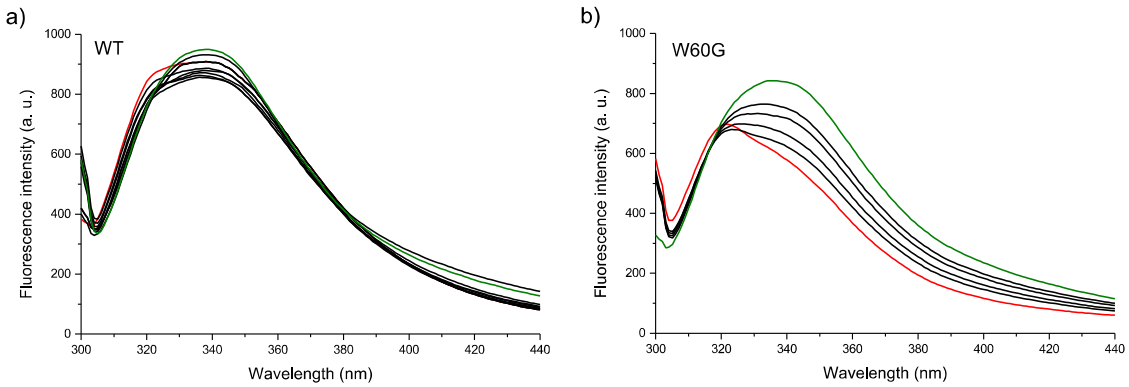

Figure 4.51. a) and b) Fluorescence quenching of 0.5 μM WT and W60G β2m, respectively, with MHA-AuNP (protein/NP from 5000 to 500). The control sample spectrum is coloured in red, while the last titration point in green.

This uncommon behaviour can be explained by considering two phenomena. The initial intensity decrease is likely to be due to the quenching of the limited Trp60 emission contribution to the whole fluorescence. Since Trp60 is exposed on the surface, it becomes accessible to the nanoparticle direct contact. The fluorescence of W60G variant is, indeed, approximately 20% lower than the WT value as showed in Figure 4.54. Differently from Cit-AuNPs, the gold core appeared to be unable to quench also the emission from Trp95 that is buried inside the protein structure, probably because of the interference of the alkanethiolate monolayer. After the initial quenching, the fluorescence pattern suggests a protein conformation perturbation induced by the nanoparticles that entails the intensity increase of Trp95 fluorescence and the shift of the emission spectrum. This interpretation is supported by the result observed with W60G β2m variant that exhibited only the intensity increase and the shift of the emission band (Figure 4.51 b). With MPA-AuNPs the same trend was observed, but while with MHA-AuNPs a conformational rearrangement effect was observable within the NP concentration range from 0.08 to 0.8 nM, to reach the same effect, MPA-AuNP concentration had to vary from 0.5 to 50 nM (Figure 4.52 a and b). Even considering that the surface of MPA-AuNPs is approximately one

fourth of MHA-AuNP surface, the perturbation induced by MPA-AuNPs proved to be weaker. This is consistent with previously established evidence of reduced interaction for NP with lower curvature radii.[23,147–149]

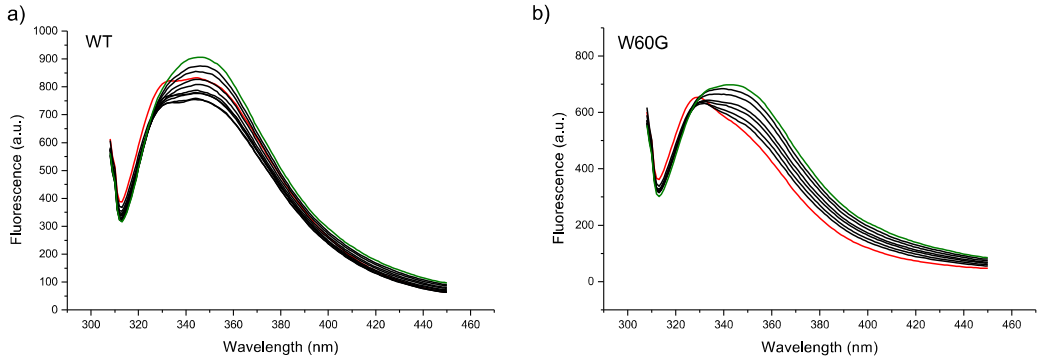

Figure 4.52. a) and b) Fluorescence quenching of 0.5 μM WT and W60G β2m, respectively, with MPA-AuNP concentrations ranging from 0 to 50 nM. The control spectrum is coloured in red, while the last titration point in green.

β2m titration with MUTAB-AuNPs showed an initial loss of intrinsic fluorescence, after which, nevertheless, the emission remained stable even on further NP addition (Figure 4.53 a).

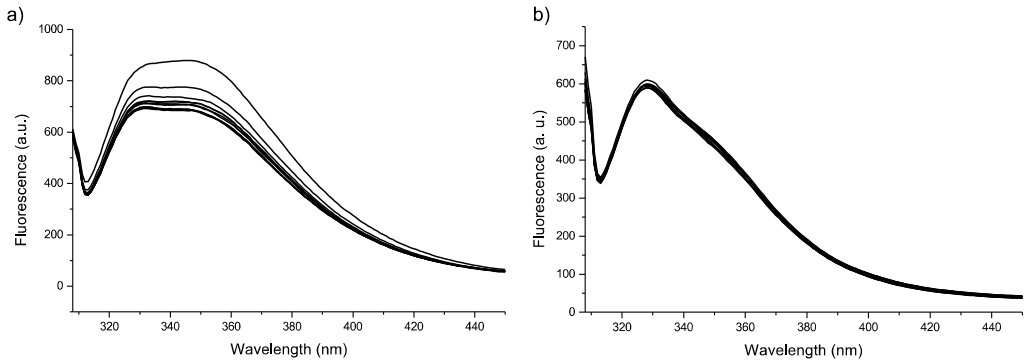

Figure 4.53. a) and b) Fluorescence quenching of 0.5 μM WT and W60G β 2m, respectively, with MUTAB-AuNPs concentrations ranging from 0 to 0.8 nM.

This result supports a weak interaction, as inferred from NMR experiments, that was not able to propagate into the core of the protein in which Trp95 is located. This result was confirmed by the substantial constancy of W60G fluorescence spectra in presence of increasing amounts of MUTAB-AuNPs (Figure 4.53 b).

To understand the nature of the initial quenching, the bimolecular quenching constants were calculated from apparent Stern-Volmer constants[111] and as a control β2m WT was titrated with MHA alkanethiol. Figure 4.54 shows that the addition of the alkanethiol alone was able to quench the fluorescence coming from Trp60.

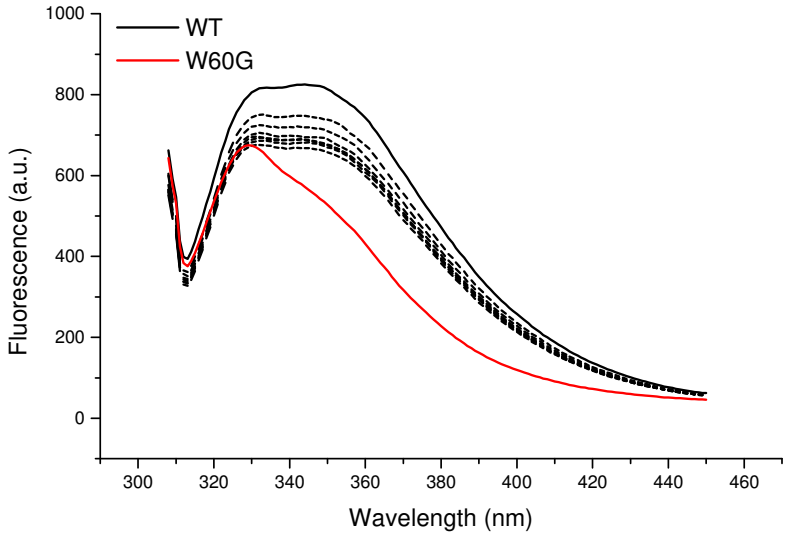

Figure 4.54. Fluorescence spectra of 0.5 μM WT (black solid line) and W60G (red line) β2m. The segmented lines correspond to the progressive addition of MHA thiol to WT β2m.

Since the bimolecular quenching constants calculated from the apparent Stern-Volmer constant (Table 4.6) (assuming a fluorescence lifetime of 1-10 ns for the indole chromophore[155]) were higher than the collisional rate limit, i.e. 2×10^{10} $M^{-1}s^{-1}$,[155] the quenching of the external tryptophan resulted not purely collisional even with the alkanethiol. The results obtained are likely to be affected by inherent inaccuracies originating from the limited number of experimental points. With an allowance of a couple of orders of magnitude, while the isolated alkanethiol pattern could be reconciled with a collisional mechanism, the values of the bimolecular quenching constant remain still far from diffusional collision rate maximum with AT-AuNPs.

Table 4.6. Parameters obtained from fluorescence quenching data fitted with Stern-Volmer equation[111] for MHA-AuNPs, MUTAB-AuNPs, MPA-AuNPs and MHA. Only the initial points of the titration in which the fluorescence decreases increasing the titrant concentration were used for the Stern-Volmer fitting.

Quencher	K_{SV} (M^{-1})	R^2	k_q ($M^{-1}s^{-1}$)
MHA-AuNPs	5×10^8	0.92	5×10^{17} - 5×10^{16}
MUTAB-AuNPs	1×10^9	0.95	1×10^{18} - 1×10^{17}
MPA-AuNPs	1×10^7	0.89	1×10^{16} - 1×10^{15}
MHA	$9{,}8 \times 10^3$	0.80	$9{,}8 \times 10^{12}$ – $9{,}8 \times 10^{11}$

4.3.4 AT-AuNPs/β2m interaction mechanism

It has been reported that proteins can stabilize AuNPs[158] or trigger their aggregation by reducing NP surface charge[159] and/or by bridging them through multiple interactions[160] leading in both cases to large agglomerates formation. The protein can then be released free in solution with or without conformational perturbations or it can be trapped in the agglomerate.

As far as MHA-AuNPs are concerned, the interaction with β2m had a destabilizing effect and led within one month to complete precipitation. TEM showed that the precipitate was made of agglomerates embedded in a protein matrix. The presence of the protein inside these aggregates could be inferred also from NMR results, i.e. the scattered positions of the residues perturbed by the NP presence and the loss of protein NMR signals after one month. Moreover, the appearance of new peaks in the random coil region in the NMR spectra revealed that MHA-AuNPs induced β2m unfolding. The capability of MHA-AuNPs to alter considerably β2m structure was proved also by fluorescence experiments which showed an increase in Trp95 fluorescence and a shift of the emission peak.

Another mechanism seems to take place in presence of MUTAB-AuNPs. From the substantial invariance of β2m NMR spectra in presence of MUTAB-AuNPs, at least when the protein was in large excess, it could be inferred that after the protein-induced agglomeration and subsequent precipitation of

NPs, β2m was mainly released to the bulk solution with only mild conformational changes. This last conclusion was assessed also by fluorescence titration experiments which did not exhibit any emission increase or shift. An additional proof of the protein exclusion from NP agglomerates came from TEM: even if the samples were stained with uranyl acetate, no clear evidences of the protein presence into NP aggregates could be found. Since β2m is slightly negative at physiological pH, the agglomeration of MUTAB-AuNPs is likely to be due to the reduction of NP positive surface charge when the protein is present in solution as a consequence of electrostatic screening. The relevance of electrostatic interactions was further confirmed by the location of the protein interaction patch. As all macromolecular polyelectrolytes, β2m has a dipolar nature with the negatively charged portion located at the C-terminal region, that in fact proved to be more involved in the interaction with MUTAB-AuNPs.

With the small negatively charged MPA-AuNPs a localized region of the protein was found to be affected by the NP presence, i.e. the N-terminal apical part. As stated before, β2m has an overall molecular dipole whose positive end corresponds to the N-terminal domain through which the protein approaches the negatively charged MPA-AuNP surface. Compared with the other considered AuNPs, the more restricted protein region involved and the lower extent of the interaction, as confirmed also by fluorescence, are mainly due to the small size of MPA-AuNPs. As already reported,[23,147–149] when the NP size decreases, the flat surface available for an extended interaction diminishes. The characteristics of β2m/MPA-AuNPs interaction did not drive NP agglomeration, as displayed by TEM images. The MPA-AuNP precipitates, indeed, were not irreversible and could be easily redispersed by sonication.

5 CONCLUSIONS

The investigation of complex protein-NP systems is a target of increasing interest because by mastering these interactions high impact results can be achieved. However, the effort to understand the molecular mechanisms of protein-NP adsorption processes has proven to be considerably challenging.

In this thesis the detailed description of the interaction between a widely employed nanoparticle, citrate-stabilized AuNP (Cit-AuNP), and a paradigmatic amyloidogenic protein, β2m, is presented. Different techniques were employed to fully characterize the system in order to obtain a clear picture of it. However, each technique used to fully characterize the protein-NP system along with its advantages, brings also some drawbacks and the data must be carefully interpreted. Basic characterization of the system was done employing DLS, TEM and UV-Vis which assessed the protein adsorption on gold nanoparticles without NP aggregation. More specific information about the locations of protein conformational perturbations in presence of Cit-AuNPs was obtained through NMR. This technique revealed that the protein undergoes some minimal structural variations that do not compromise the overall protein native conformation suggesting a labile and transient interaction. The same conclusions could be drawn not only for the wild-type form, but also for two more amyloidogenic variants, namely D76N and ΔN6, though ΔN6 structure proved to be slightly more affected by NP presence. ^{15}N relaxation NMR was employed also to gain deeper insights into the protein dynamics and the exchange process kinetic, but the protein concentration limits imposed by Cit-AuNPs concentration did not allow to reach reliable conclusion so far. Work is still going on to optimize these experiments. To have a thermodynamic characterization of the system, protein intrinsic fluorescence quenching and AuNP SPR band shift were exploited. By fitting the data obtained with the corresponding functions reported in literature, nM and μM dissociation constants were calculated

from fluorescence and UV-Vis experiments, respectively. These dissociation constants values, beyond differing by three orders of magnitude, are totally inconsistent with NMR results. It should be stated that the models on which the fitting equations rely are much different from protein-NP systems. As far as fluorescence is concerned, mechanisms other than static quenching, e.g. energy and electron transfer, are highly probable considering the plasmonic nature of nanoparticles. The Langmuir adsorption model used with UV-Vis data refers to the adsorption of a ordered monolayer of molecules on a surface composed of series of identical binding sites. AuNPs are known to present on their surface many defects such as edges and corners that exhibit different binding affinities. Despite being unsuitable for a quantitative thermodynamic characterization of protein-NP systems, these two spectroscopic techniques offered important proofs about the protein structural preservation (fluorescence), the nanoparticle absorption capacity (UV-Vis) and the similar extent of interaction of the three β2m variants tested (fluorescence and UV-Vis). QCMD experiments revealed that in presence of Cit-AuNPs D76N β2m presents a faster adsorption kinetics and different viscoelastic properties, particularly it forms less compact layers. Both these features suggest that Cit-AuNPs are able to reduce the association extent of the protein in solution. By measuring through NMR the β2m diffusion coefficient in presence and in absence of Cit-AuNPs, it was discovered that Cit-AuNPs actually interfere with the protein association by shifting the equilibrium towards lower molecular weight oligomers. Moreover, NMR showed that in presence of Cit-AuNPs the intrinsic local unfolding of a particular β2m variant, i.e. ΔN6, is hindered. The overall evidence of Cit-AuNPs ability to interfere with β2m association and aggregation behaviour found conclusive proof in the demonstration that Cit-AuNPs are able to hamper D76N fibrillogenesis *in vitro*. Thioflavin T assays and TEM imaging revealed the partial inhibition of fibres formation in presence of Cit-AuNPs. The same aggregation kinetics measured in presence and in absence of Cit-

AuNPs and the decrease of the NP inhibitory capability as the protein concentration increases suggest a competitive mechanism between the fibrillogenesis pathway and the protein-NP interaction. In general, all the consequences on protein structure and behaviour proved to propagate in the bulk involving more than the single shell of proteins in direct contact with the surface. This consideration is consistent with a dynamic turnover of proteins on the gold surface.

Since with other nanoparticles, e.g. carbon nanotubes, quantum dots and polymeric nanoparticles, opposite results have been found concerning β2m fibrillogenesis, the effect of AuNP physico-chemical properties on the interaction pattern with β2m WT was studied. To this aim, MHA-AuNPs and MUTAB-AuNPs of 7.5 nm and MPA-AuNPs of 3.6 nm were prepared. β2m WT was incubated with these AuNPs and the samples were analysed by UV-Vis, TEM, NMR and fluorescence spectroscopy. MHA-AuNPs have a destabilizing effect on the protein structure and in time cause its unfolding while precipitating together. β2m triggers the sudden precipitation of MUTAB-AuNPs by reducing the positive repulsion between them and is then released free in solution with minor conformational changes, at least at higher protein/NP ratios. With small MPA-AuNPs a strong localization of the interaction related to the compactness of the NP electron plasma was found. This interaction do not affect both the protein overall structure and the NP aggregation state. The results obtained with these different AuNPs prove that the interaction mechanisms are highly dependent on the NP properties and could lead to unexpected effects.

All in all, even if a comprehensive model of bio-nano interfaces is starting to emerge, much more efforts must be performed to fully understand and manage protein-NP interactions. Moreover, it is becoming increasingly clear that different techniques must be employed with expert data interpretation.

6 APPENDIX

Table A1. Relaxation rate and heteronuclear NOE values of 4 μM wild-type β2m measured at pH 7 in 50 mM HEPES buffer and 1.5 mM sodium citrate at 298 K. The errors reported for relaxation rates were calculated by systematic error variance averaging from repeated experiments. For NOE values errors were calculated from the signal-to-noise ratio.

Residue	R_1 (s^{-1})	R_1 error (s^{-1})	R_2 (s^{-1})	R_2 error (s^{-1})	$R_{1\rho}$ (s^{-1})	$R_{1\rho}$ error (s^{-1})	NOE	NOE error
Ile1								
Gln2							0,354	0,051
Arg3	2,744	0,939	9,062	2,496	8,730	2,601	0,899	0,130
Thr4								
Pro5								
Lys6	1,964	0,519	9,217	1,988	9,145	2,018	1,000	0,144
Ile7							0,921	0,133
Gln8								
Val9	1,998	0,319	7,675	1,184	8,420	1,333	0,587	0,085
Tyr10	1,918	0,310	10,313	1,631	9,721	1,389	0,801	0,116
Ser11	1,968	0,427	12,536	1,926	9,159	1,498	0,905	0,131
Arg12	2,348	0,450	10,864	1,923	11,217	1,668	0,939	0,136
His13	2,094	0,371	11,105	2,978	10,893	1,526	0,989	0,143
Pro14								
Ala15								
Glu16	1,406	0,285	11,651	2,408	10,366	1,889	0,570	0,082
Asn17							0,650	0,094
Gly18	1,977	0,452	12,495	2,205	11,293	1,946	0,999	0,144
Lys19	2,409	0,420	11,261	1,449	12,650	1,696	0,481	0,069
Ser20								
Asn21	1,423	0,231	10,177	1,428	12,150	2,648	0,981	0,141
Phe22	3,114	0,688	10,966	2,664	10,353	1,876	0,612	0,088
Leu23	1,926	0,281	10,828	1,433	10,218	1,555	0,926	0,134
Asn24							0,986	0,142
Cys25	2,144	0,463	8,626	1,462	7,454	1,437	0,804	0,116
Tyr26	2,308	0,426	10,925	1,785	12,119	2,201	0,851	0,123
Val27								
Ser28	2,813	0,923	14,660	4,663	11,495	3,527	0,850	0,123
Gly29								
Phe30	2,663	0,777	14,243	2,726	9,981	1,826	0,998	0,144
His31								
Pro32								
Ser33	1,667	0,340	12,549	2,092	12,075	2,127	0,803	0,116
Asp34	1,698	0,211	10,743	1,170	9,936	1,000	0,871	0,126
Ile35	1,269	0,188	10,127	1,049	9,401	0,975	0,794	0,115

Glu36								
Val37	1,809	0,164	8,526	0,640	8,275	0,694	0,858	0,124
Asp38							0,556	0,080
Leu39	2,665	0,577	12,555	2,003	9,893	1,857	0,721	0,104
Leu40	1,938	0,416	10,078	1,645	10,435	1,856	0,646	0,093
Lys41	1,586	0,291	11,378	1,737	8,587	1,323	0,659	0,095
Asn42	1,853	0,216	7,483	0,758	7,611	0,757	0,715	0,103
Gly43	2,062	0,392	10,687	1,700	7,660	1,764	0,826	0,119
Glu44	1,649	0,209	11,420	1,317	11,666	1,204	0,845	0,122
Arg45	2,142	0,329	9,498	1,563	7,256	1,252	0,659	0,095
Ile46	1,645	0,329	15,231	2,862	11,232	2,005	0,753	0,109
Glu47	1,824	0,293	10,888	1,575	14,093	1,725	0,608	0,088
Lys48	1,751	0,236	8,884	1,190	8,711	0,979	0,625	0,090
Val49	1,944	0,270	8,894	0,998	7,971	0,977	0,639	0,092
Glu50	1,486	0,218	10,007	1,113	9,463	1,052	0,764	0,110
His51								
Ser52	1,605	0,310	10,484	1,679	10,251	1,618	0,959	0,138
Asp53								
Leu54								
Ser55							0,909	0,131
Phe56	2,014	0,529	12,444	2,805	11,253	2,371	0,899	0,130
Ser57								
Lys58								
Asp59							0,842	0,121
Trp60								
Ser61								
Phe62								
Tyr63								
Leu64	2,412	0,424	11,448	1,903	8,921	1,613	0,982	0,142
Leu65							0,728	0,105
Tyr66	1,554	0,150	8,899	0,689	9,079	0,680	0,793	0,114
Tyr67	2,427	0,430	12,644	1,655	8,662	1,281	0,878	0,127
Thr68	1,565	0,247	10,151	1,536	8,447	1,193	0,781	0,113
Glu69	1,597	0,211	8,699	1,107	7,909	1,111	0,780	0,113
Phe70	1,962	0,366	6,406	1,174	6,637	1,516	0,512	0,074
Thr71	1,629	0,312	6,859	1,376	7,716	1,298	0,876	0,126
Pro72								
Thr73	1,415	0,237	9,946	1,641	7,567	1,352	0,817	0,118
Glu74	1,632	0,406	10,271	2,353	9,017	3,512	0,680	0,098
Lys75	1,636	0,234	9,238	1,120	8,066	1,033	0,790	0,114
Asp76	1,970	0,264	10,008	1,189	8,000	0,908	0,878	0,127
Glu77	1,988	0,336	9,216	1,425	11,343	1,540	0,971	0,140
Tyr78	2,205	0,380	9,429	1,408	7,852	1,522	0,740	0,107
Ala79	2,381	0,367	9,113	1,246	10,441	1,676	0,821	0,118
Cys80	1,957	0,424	10,714	2,162	8,617	1,816	0,651	0,094
Arg81	1,695	0,292	12,359	2,421	8,396	1,635	0,668	0,096

Val82							0,748	0,108
Asn83	1,805	0,385	12,056	1,735	9,255	1,665	0,841	0,121
His84	2,019	0,307	8,596	1,107	8,098	1,105	0,682	0,098
Val85							0,808	0,117
Thr86								
Leu87	2,096	0,380	10,420	1,494	8,614	1,103	0,814	0,117
Ser88								
Gln89	1,788	0,206	10,095	0,960	7,539	0,758	0,731	0,105
Pro90								
Lys91	1,823	0,292	9,654	1,305	9,017	1,279	0,895	0,129
Ile92	1,613	0,246	9,368	1,324	9,758	1,369	0,796	0,115
Val93	1,538	0,275	7,953	1,277	5,947	1,625	0,898	0,130
Lys94	1,525	0,344	11,527	1,905	11,417	2,037	0,709	0,102
Trp95	1,574	0,331	8,853	1,444	10,177	1,624	0,647	0,093
Asp96	1,514	0,252	10,336	1,547	11,221	1,509	0,745	0,108
Arg97	1,785	0,258	7,825	1,062	8,158	1,040	0,536	0,077
Asp98	2,011	0,192	6,199	0,678	5,462	0,605	0,559	0,081
Met99	1,650	0,136	3,984	0,380	4,824	0,423	0,187	0,027

Table A2. Relaxation rate and heteronuclear NOE values of 4 μM wild-type β2m in presence of 30 nM Cit-AuNPs measured at pH 7 in 50 mM HEPES buffer and 1.5 mM sodium citrate at 298 K. The errors reported for relaxation rates were calculated by systematic error variance averaging from repeated experiments. For NOE values errors were calculated from the signal-to-noise ratio.

Residue	R_1 (s^{-1})	R_1 error (s^{-1})	R_2 (s^{-1})	R_2 error (s^{-1})	$R_{1\rho}$ (s^{-1})	$R_{1\rho}$ error (s^{-1})	NOE	NOE error
Ile1								
Gln2							0,508	0,143
Arg3	2,794	3,094	10,539	8,047	10,260	5,526	0,789	0,222
Thr4								
Pro5								
Lys6	3,807	2,615	6,258	13,096	18,892	8,668	0,680	0,191
Ile7							0,799	0,225
Gln8								
Val9	1,130	0,397	9,579	2,802	11,081	2,526	0,803	0,226
Tyr10	1,770	0,508	9,744	4,029	13,044	2,463	0,780	0,219
Ser11	2,140	0,871	14,057	4,588	9,598	2,613	0,743	0,209
Arg12	1,802	0,620	12,457	3,643	11,273	2,216	0,778	0,219
His13	1,779	0,449	10,773	3,183	10,496	2,228	0,781	0,219
Pro14								
Ala15								
Glu16	1,744	0,649	11,607	4,228	12,284	2,629	0,431	0,121
Asn17							0,699	0,197
Gly18	1,607	0,661	10,278	3,593	7,991	2,525	0,690	0,194
Lys19	2,269	0,588	10,124	2,491	12,141	1,785	0,999	0,281
Ser20								
Asn21	1,936	0,528	8,893	2,834	17,073	4,380	0,519	0,146
Phe22	4,148	1,812	10,024	3,898	9,913	2,512	0,716	0,201
Leu23	2,267	0,521	11,488	2,100	10,219	2,615	0,997	0,280
Asn24							0,656	0,184
Cys25	1,841	0,612	12,967	4,060	7,152	2,055	0,561	0,158
Tyr26	1,909	0,616	11,965	3,882	12,598	3,895	0,874	0,246
Val27								
Ser28	1,124	0,898	11,217	16,398	18,967	10,644	1,000	0,281
Gly29								
Phe30	3,590	1,655	10,342	22,787	11,946	3,802	0,994	0,279
His31								
Pro32								
Ser33	2,063	0,681	10,851	4,874	9,381	3,024	0,981	0,276
Asp34	1,115	0,267	10,284	2,439	12,060	2,207	0,829	0,233
Ile35	1,908	0,508	8,717	1,800	9,012	1,719	0,722	0,203
Glu36								
Val37	1,487	0,260	9,224	1,396	9,609	1,389	0,965	0,271
Asp38							0,776	0,218

Leu39	1,683	0,657	11,366	4,620	11,992	3,668	0,746	0,210
Leu40	2,142	0,683	9,455	2,880	5,968	1,772	0,994	0,279
Lys41	1,998	0,536	13,346	4,469	14,446	3,660	0,724	0,203
Asn42	2,237	0,468	8,496	1,552	10,007	1,203	0,655	0,184
Gly43	1,835	0,544	10,338	3,246	14,417	3,167	0,757	0,213
Glu44	1,845	0,363	10,318	2,021	12,858	1,784	0,876	0,246
Arg45	2,413	0,778	9,669	2,865	7,415	1,906	0,990	0,278
Ile46	2,006	0,750	11,818	4,055	9,498	3,950	0,883	0,248
Glu47	1,843	0,548	16,673	5,399	10,770	2,143	0,995	0,280
Lys48	1,334	0,298	10,810	1,992	8,511	1,304	1,000	0,281
Val49	1,935	0,504	9,716	2,060	9,009	1,558	0,988	0,278
Glu50	1,688	0,587	9,634	2,497	8,387	1,612	0,730	0,205
His51								
Ser52	2,525	0,880	11,965	3,309	10,223	2,953	0,432	0,121
Asp53								
Leu54								
Ser55							0,797	0,224
Phe56	2,125	1,521	13,747	10,747	9,081	4,979	0,948	0,267
Ser57								
Lys58								
Asp59							0,608	0,171
Trp60								
Ser61								
Phe62								
Tyr63								
Leu64	3,076	1,844	8,830	6,720	15,238	3,307	0,751	0,211
Leu65							0,527	0,148
Tyr66	1,844	0,268	9,655	1,417	9,264	0,888	0,641	0,180
Tyr67	1,762	0,490	12,301	3,274	8,097	1,837	0,522	0,147
Thr68	1,777	0,496	8,195	1,987	9,602	2,577	0,917	0,258
Glu69	1,725	0,402	9,460	2,123	8,916	1,633	0,999	0,281
Phe70	1,945	1,076	6,612	2,979	6,520	2,309	0,497	0,140
Thr71	1,624	0,469	12,527	2,899	8,188	1,578	0,840	0,236
Pro72								
Thr73	1,592	0,483	11,127	2,762	14,830	2,717	0,748	0,210
Glu74	2,123	1,612	11,734	4,549	10,972	3,276	0,757	0,213
Lys75	1,861	0,406	8,290	1,770	8,279	1,427	0,683	0,192
Asp76	1,645	0,314	9,325	1,795	8,414	1,355	0,533	0,150
Glu77	1,350	0,382	8,905	2,934	10,738	1,924	0,928	0,261
Tyr78	1,994	0,680	9,586	2,854	9,967	2,341	0,811	0,228
Ala79	3,057	0,774	9,881	2,164	9,096	1,717	0,852	0,239
Cys80	1,819	0,672	11,726	3,893	9,797	2,736	0,944	0,265
Arg81	2,343	0,739	10,321	3,787	9,363	2,312	0,871	0,245
Val82							0,734	0,206
Asn83	1,826	0,571	10,864	2,613	11,800	2,264	0,999	0,281
His84	1,748	0,472	12,409	3,024	13,511	2,220	0,925	0,260

Val85							0,826	0,232
Thr86								
Leu87	1,595	0,422	8,646	2,353	10,270	1,831	0,998	0,280
Ser88								
Gln89	1,708	0,293	7,947	1,496	9,515	1,071	0,803	0,226
Pro90								
Lys91	2,209	0,591	8,985	2,905	10,040	2,167	1,000	0,281
Ile92	1,837	0,599	8,240	2,671	9,363	1,915	0,853	0,240
Val93	1,769	0,495	9,742	2,485	11,497	2,124	0,636	0,179
Lys94	1,649	0,641	11,086	3,044	9,227	3,121	0,989	0,278
Trp95	2,563	1,015	10,439	3,583	18,092	4,129	1,000	0,281
Asp96	3,019	1,376	10,090	4,918	3,690	7,734	0,963	0,271
Arg97	1,853	0,740	8,951	3,555	11,541	2,744	0,782	0,220
Asp98	2,262	0,380	6,953	1,366	5,297	0,969	0,814	0,229
Met99	1,365	0,375	3,482	1,419	4,331	1,122	0,840	0,236

7 BIBLIOGRAPHY

1. Nirmal, M. & Brus, L. Luminescence Photophysics in Semiconductor Nanocrystals. *Acc. Chem. Res.* **32,** 407–414 (1999).
2. Chan, W. C. W. & Nie, S. Quantum Dot Bioconjugates for Ultrasensitive Nonisotopic Detection. *Science* **281,** 2016–2018 (1998).
3. Alivisatos, A. P. Semiconductor Clusters, Nanocrystals, and Quantum Dots. *Science* **271,** 933–937 (1996).
4. De, M., Ghosh, P. S. & Rotello, V. M. Applications of Nanoparticles in Biology. *Adv. Mater.* **20,** 4225–4241 (2008).
5. Wang, Y. Nonlinear optical properties of nanometer-sized semiconductor clusters. *Acc. Chem. Res.* **24,** 133–139 (1991).
6. Steigerwald, M. L. & Brus, L. E. Semiconductor crystallites: a class of large molecules. *Acc. Chem. Res.* **23,** 183–188 (1990).
7. Weller, H. Quantized Semiconductor Particles: A novel state of matter for materials science. *Adv. Mater.* **5,** 88–95 (1993).
8. Mahmoudi, M., Azadmanesh, K., Shokrgozar, M. A., Journeay, W. S. & Laurent, S. Effect of Nanoparticles on the Cell Life Cycle. *Chem. Rev.* **111,** 3407–3432 (2011).
9. Fadeel, B. & Garcia-Bennett, A. E. Better safe than sorry: Understanding the toxicological properties of inorganic nanoparticles manufactured for biomedical applications. *Adv. Drug Deliv. Rev.* **62,** 362–374 (2010).

10. Klein, J. Probing the interactions of proteins and nanoparticles. *Proc. Natl. Acad. Sci.* **104,** 2029–2030 (2007).

11. Monopoli, M. P. *et al.* Physical−Chemical Aspects of Protein Corona: Relevance to in Vitro and in Vivo Biological Impacts of Nanoparticles. *J. Am. Chem. Soc.* **133,** 2525–2534 (2011).

12. Cedervall, T. *et al.* Detailed Identification of Plasma Proteins Adsorbed on Copolymer Nanoparticles. *Angew. Chem. Int. Ed.* **46,** 5754–5756 (2007).

13. Kaufman, E. D. *et al.* Probing Protein Adsorption onto Mercaptoundecanoic Acid Stabilized Gold Nanoparticles and Surfaces by Quartz Crystal Microbalance and ζ-Potential Measurements. *Langmuir* **23,** 6053–6062 (2007).

14. Lynch, I., Dawson, K. A. & Linse, S. Detecting Cryptic Epitopes Created by Nanoparticles. *Sci STKE* **2006,** pe14-pe14 (2006).

15. Lynch, I. & Dawson, K. A. Protein-nanoparticle interactions. *Nano Today* **3,** 40–47 (2008).

16. Nel, A. E. *et al.* Understanding biophysicochemical interactions at the nano–bio interface. *Nat. Mater.* **8,** 543–557 (2009).

17. Wang, A., Vangala, K., Vo, T., Zhang, D. & Fitzkee, N. C. A Three-Step Model for Protein–Gold Nanoparticle Adsorption. *J. Phys. Chem. C* **118,** 8134–8142 (2014).

18. Faunce, T. A., White, J. & Matthaei, K. I. Integrated research into the nanoparticle–protein corona: a new focus for safe, sustainable and equitable development of nanomedicines. *Nanomed.* **3,** 859–866 (2008).

19. Röcker, C., Pötzl, M., Zhang, F., Parak, W. J. & Nienhaus, G. U. A quantitative fluorescence study of protein monolayer formation on colloidal nanoparticles. *Nat. Nanotechnol.* **4,** 577–580 (2009).

20. Chakraborty, S. *et al.* Contrasting Effect of Gold Nanoparticles and Nanorods with Different Surface Modifications on the Structure and Activity of Bovine Serum Albumin. *Langmuir* **27,** 7722–7731 (2011).

21. Shang, L., Wang, Y., Jiang, J. & Dong, S. pH-Dependent Protein Conformational Changes in Albumin:Gold Nanoparticle Bioconjugates: A Spectroscopic Study. *Langmuir* **23,** 2714–2721 (2007).

22. Lundqvist, M., Sethson, I. & Jonsson, B.-H. Protein Adsorption onto Silica Nanoparticles: Conformational Changes Depend on the Particles' Curvature and the Protein Stability. *Langmuir* **20,** 10639–10647 (2004).

23. Lacerda, S. H. D. P. *et al.* Interaction of Gold Nanoparticles with Common Human Blood Proteins. *ACS Nano* **4,** 365–379 (2010).

24. Wang, Y. & Ni, Y. Combination of UV–vis spectroscopy and chemometrics to understand protein–nanomaterial conjugate: A case study on human serum albumin and gold nanoparticles. *Talanta* **119,** 320–330 (2014).

25. Delfino, I. & Cannistraro, S. Optical investigation of the electron transfer protein azurin–gold nanoparticle system. *Biophys. Chem.* **139,** 1–7 (2009).

26. Lee, I. S. *et al.* Ni/NiO Core/Shell Nanoparticles for Selective Binding and Magnetic Separation of Histidine-Tagged Proteins. *J. Am. Chem. Soc.* **128,** 10658–10659 (2006).

27. Xiao, Q. *et al.* Conformation, thermodynamics and stoichiometry of HSA adsorbed to colloidal CdSe/ZnS quantum dots. *Biochim. Biophys. Acta BBA - Proteins Proteomics* **1784,** 1020–1027 (2008).

28. Pompa, P. P. *et al.* Fluorescence resonance energy transfer induced by conjugation of metalloproteins to nanoparticles. *Chem. Phys. Lett.* **417,** 351–357 (2006).

29. Pons, T., Medintz, I. L., Wang, X., English, D. S. & Mattoussi, H. Solution-Phase Single Quantum Dot Fluorescence Resonance Energy Transfer. *J. Am. Chem. Soc.* **128,** 15324–15331 (2006).

30. AlléAaemann, E., Gravel, P., Leroux, J.-C., Balant, L. & Gurny, R. Kinetics of blood component adsorption on poly(D,L-lactic acid) nanoparticles: Evidence of complement C3 component involvement. *J. Biomed. Mater. Res.* **37,** 229–234 (1997).

31. Jiang, X. *et al.* Quantitative analysis of the protein corona on FePt nanoparticles formed by transferrin binding. *J. R. Soc. Interface* **7 Suppl 1,** S5–S13 (2010).

32. Karajanagi, S. S., Vertegel, A. A., Kane, R. S. & Dordick, J. S. Structure and Function of Enzymes Adsorbed onto Single-Walled Carbon Nanotubes. *Langmuir* **20,** 11594–11599 (2004).

33. Jiang, X., Jiang, J., Jin, Y., Wang, E. & Dong, S. Effect of Colloidal Gold Size on the Conformational Changes of Adsorbed Cytochrome c: Probing by Circular Dichroism, UV−Visible, and Infrared Spectroscopy. *Biomacromolecules* **6,** 46–53 (2005).

34. Shen, X.-C., Liou, X.-Y., Ye, L.-P., Liang, H. & Wang, Z.-Y. Spectroscopic studies on the interaction between human hemoglobin and CdS quantum dots. *J. Colloid Interface Sci.* **311,** 400–406 (2007).

35. George J. Thomas, J. Raman Spectroscopy of Protein and Nucleic Acid Assemblies. *Annu. Rev. Biophys. Biomol. Struct.* **28,** 1–27 (1999).

36. Aubin-Tam, M.-E. & Hamad-Schifferli, K. Gold Nanoparticle−Cytochrome c Complexes: The Effect of Nanoparticle Ligand Charge on Protein Structure. *Langmuir* **21,** 12080–12084 (2005).

37. Yang, J. A. *et al.* Study of Wild-Type α-Synuclein Binding and Orientation on Gold Nanoparticles. *Langmuir* **29,** 4603–4615 (2013).

38. Calzolai, L., Franchini, F., Gilliland, D. & Rossi, F. Protein−Nanoparticle Interaction: Identification of the Ubiquitin−Gold Nanoparticle Interaction Site. *Nano Lett.* **10,** 3101–3105 (2010).

39. Lindman, S. *et al.* Systematic Investigation of the Thermodynamics of HSA Adsorption to N-iso-Propylacrylamide/N-tert-Butylacrylamide Copolymer Nanoparticles. Effects of Particle Size and Hydrophobicity. *Nano Lett.* **7,** 914–920 (2007).

40. Brancolini, G. *et al.* Probing the Influence of Citrate-Capped Gold Nanoparticles on an Amyloidogenic Protein. *ACS Nano* **9,** 2600–2613 (2015).

41. Ceccon, A. *et al.* NMR investigation of the equilibrium partitioning of a water-soluble bile salt protein carrier to phospholipid vesicles. *Proteins Struct. Funct. Bioinforma.* **81,** 1776–1791 (2013).

42. Lundqvist, M., Sethson, I. & Jonsson, B.-H. High-Resolution 2D 1H−15N NMR Characterization of Persistent Structural Alterations of Proteins Induced by Interactions with Silica Nanoparticles. *Langmuir* **21,** 5974–5979 (2005).

43. Pedò, M. *et al.* NMR studies reveal the role of biomembranes in modulating ligand binding and release by intracellular bile acid binding proteins. *J. Mol. Biol.* **394,** 852–863 (2009).

44. Calvaresi, M. *et al.* C60@Lysozyme: Direct Observation by Nuclear Magnetic Resonance of a 1:1 Fullerene Protein Adduct. *ACS Nano* **8,** 1871–1877 (2014).

45. Chevelkov, V., Xue, Y., Rao, D. K., Forman-Kay, J. D. & Skrynnikov, N. R. 15NH/D-SOLEXSY experiment for accurate measurement of amide solvent exchange rates: application to denatured drkN SH3. *J. Biomol. NMR* **46,** 227–244 (2010).

46. Ceccon, A., Tugarinov, V., Bax, A. & Clore, G. M. Global Dynamics and Exchange Kinetics of a Protein on the Surface of Nanoparticles

Revealed by Relaxation-Based Solution NMR Spectroscopy. *J. Am. Chem. Soc.* **138,** 5789–5792 (2016).

47. Zanzoni, S. *et al.* Polyhydroxylated [60]fullerene binds specifically to functional recognition sites on a monomeric and a dimeric ubiquitin. *Nanoscale* **7,** 7197–7205 (2015).

48. Sauerbrey, G. Verwendung von Schwingquarzen zur Wägung dünner Schichten und zur Mikrowägung. *Z. Für Phys.* **155,** 206–222 (1959).

49. Brewer, S. H., Glomm, W. R., Johnson, M. C., Knag, M. K. & Franzen, S. Probing BSA Binding to Citrate-Coated Gold Nanoparticles and Surfaces. *Langmuir* **21,** 9303–9307 (2005).

50. Hardy, J. & Selkoe, D. J. The Amyloid Hypothesis of Alzheimer's Disease: Progress and Problems on the Road to Therapeutics. *Science* **297,** 353–356 (2002).

51. Nelson, R. & Eisenberg, D. Structural Models of Amyloid-Like Fibrils. in *Advances in Protein Chemistry* **73,** 235–282 (Academic Press, 2006).

52. Sato, T. *et al.* Inhibitors of Amyloid Toxicity Based on β-sheet Packing of Aβ40 and Aβ42. *Biochemistry (Mosc.)* **45,** 5503–5516 (2006).

53. Petkova, A. T., Yau, W.-M. & Tycko, R. Experimental Constraints on Quaternary Structure in Alzheimer's β-Amyloid Fibrils. *Biochemistry (Mosc.)* **45,** 498–512 (2006).

54. Jahn, T. R. & Radford, S. E. The Yin and Yang of protein folding. *FEBS J.* **272,** 5962–5970 (2005).

55. Gejyo, F. *et al.* A new form of amyloid protein associated with chronic hemodialysis was identified as β2-microglobulin. *Biochem. Biophys. Res. Commun.* **129,** 701–706 (1985).

56. Bjorkman, P. J. *et al.* Structure of the human class I histocompatibility antigen, HLA-A2. *Nature* **329,** 506–512 (1987).

57. Verdone, G. *et al.* The solution structure of human β2-microglobulin reveals the prodromes of its amyloid transition. *Protein Sci. Publ. Protein Soc.* **11,** 487–499 (2002).

58. Eichner, T. & Radford, S. E. A generic mechanism of beta2-microglobulin amyloid assembly at neutral pH involving a specific proline switch. *J. Mol. Biol.* **386,** 1312–1326 (2009).

59. Esposito, G., Corazza, A. & Bellotti, V. Pathological Self-Aggregation ofb2-Microglobulin: A Challenge for Protein Biophysics. in *Protein Aggregation and Fibrillogenesis in Cerebral and Systemic Amyloid Disease* 165–183 (Springer, Dordrecht, 2012). doi:10.1007/978-94-007-5416-4_7

60. Valleix, S. *et al.* Hereditary Systemic Amyloidosis Due to Asp76Asn Variant β2-Microglobulin. *N. Engl. J. Med.* **366,** 2276–2283 (2012).

61. Mangione, P. P. *et al.* Structure, Folding Dynamics, and Amyloidogenesis of D76N β2-Microglobulin. *J. Biol. Chem.* **288**, 30917-30930 (2013).

62. Bellotti, V. *et al.* β 2-microglobulin can be refolded into a native state from ex vivo amyloid fibrils. *Eur. J. Biochem.* **258,** 61–67 (1998).

63. Esposito, G. *et al.* Removal of the N-terminal hexapeptide from human β2-microglobulin facilitates protein aggregation and fibril formation. *Protein Sci.* **9,** 831–845 (2000).

64. Lindgren, M., Sörgjerd, K. & Hammarström, P. Detection and Characterization of Aggregates, Prefibrillar Amyloidogenic Oligomers, and Protofibrils Using Fluorescence Spectroscopy. *Biophys. J.* **88,** 4200–4212 (2005).

65. Jansen, R., Dzwolak, W. & Winter, R. Amyloidogenic Self-Assembly of Insulin Aggregates Probed by High Resolution Atomic Force Microscopy. *Biophys. J.* **88,** 1344–1353 (2005).

66. Howie, A. J. & Brewer, D. B. Optical properties of amyloid stained by Congo red: History and mechanisms. *Micron* **40,** 285–301 (2009).

67. Groenning, M. Binding mode of Thioflavin T and other molecular probes in the context of amyloid fibrils—current status. *J. Chem. Biol.* **3,** 1–18 (2010).

68. Ban, T., Hamada, D., Hasegawa, K., Naiki, H. & Goto, Y. Direct Observation of Amyloid Fibril Growth Monitored by Thioflavin T Fluorescence. *J. Biol. Chem.* **278**, 16462-16465 (2003).

69. Nilsson, K. P. R. Small organic probes as amyloid specific ligands – Past and recent molecular scaffolds. *FEBS Lett.* **583,** 2593–2599 (2009).

70. Lindgren, M. & Hammarström, P. Amyloid oligomers: spectroscopic characterization of amyloidogenic protein states. *FEBS J.* **277,** 1380–1388 (2010).

71. Kumar, M., Hong, Y., Thorn, D. C., Ecroyd, H. & Carver, J. A. Monitoring Early-Stage Protein Aggregation by an Aggregation-Induced Emission Fluorogen. *Anal. Chem.* **89,** 9322–9329 (2017).

72. Bitan, G., Lomakin, A. & Teplow, D. B. Amyloid β-Protein Oligomerization PRENUCLEATION INTERACTIONS REVEALED BY PHOTO-INDUCED CROSS-LINKING OF UNMODIFIED PROTEINS. *J. Biol. Chem.* **276,** 35176–35184 (2001).

73. Bitan, G. Structural Study of Metastable Amyloidogenic Protein Oligomers by Photo-Induced Cross-Linking of Unmodified Proteins. in *Methods in Enzymology* **413,** 217–236 (Academic Press, 2006).

74. Bagriantsev, S. N., Kushnirov, V. V. & Liebman, S. W. Analysis of Amyloid Aggregates Using Agarose Gel Electrophoresis. in *Methods in Enzymology* **412,** 33–48 (Academic Press, 2006).

75. Tycko, R. Molecular structure of amyloid fibrils: insights from solid-state NMR. *Q. Rev. Biophys.* **39,** 1–55 (2006).

76. Gremer, L. *et al.* Fibril structure of amyloid-β(1-42) by cryoelectron microscopy. *Science* eaao2825 (2017). doi:10.1126/science.aao2825

77. Shelton, C. C. *et al.* Modulation of γ-secretase specificity using small molecule allosteric inhibitors. *Proc. Natl. Acad. Sci.* **106,** 20228–20233 (2009).

78. Sun, Y. *et al.* Synthesis of scyllo-inositol derivatives and their effects on amyloid beta peptide aggregation. *Bioorg. Med. Chem.* **16,** 7177–7184 (2008).

79. Shoval, H., Lichtenberg, D. & Gazit, E. The molecular mechanisms of the anti-amyloid effects of phenols. *Amyloid* **14,** 73–87 (2007).

80. Findeis, M. A. Approaches to discovery and characterization of inhibitors of amyloid β-peptide polymerization. *Biochim. Biophys. Acta BBA - Mol. Basis Dis.* **1502,** 76–84 (2000).

81. Bard, F. *et al.* Peripherally administered antibodies against amyloid β-peptide enter the central nervous system and reduce pathology in a mouse model of Alzheimer disease. *Nat. Med.* **6,** 916–919 (2000).

82. Lee, K.-W. *et al.* Clusterin regulates transthyretin amyloidosis. *Biochem. Biophys. Res. Commun.* **388,** 256–260 (2009).

83. Ecroyd, H. & Carver, J. A. Crystallin proteins and amyloid fibrils. *Cell. Mol. Life Sci.* **66,** 62 (2009).

84. Mahmoudi, M., Kalhor, H. R., Laurentd, S. & Lynch, I. Protein fibrillation and nanoparticle interactions: opportunities and challenges. *Nanoscale*, **5**, 2570-2588 (2013).

85. Linse, S. *et al.* Nucleation of protein fibrillation by nanoparticles. *Proc. Natl. Acad. Sci.* **104,** 8691–8696 (2007).

86. Skaat, H., Belfort, G. & Margel, S. Synthesis and characterization of fluorinated magnetic core-shell nanoparticles for inhibition of insulin amyloid fibril formation. *Nanotechnology* **20,** 225106 (2009).

87. Boridy, S., Takahashi, H., Akiyoshi, K. & Maysinger, D. The binding of pullulan modified cholesteryl nanogels to Aβ oligomers and their suppression of cytotoxicity. *Biomaterials*, **30**, 5583-5591 (2009).

88. Ghavami, M. *et al.* Plasma concentration gradient influences the protein corona decoration on nanoparticles. *RSC Adv.* **3,** 1119–1126 (2012).

89. Wu, W. *et al.* TiO2 nanoparticles promote β-amyloid fibrillation in vitro. *Biochem. Biophys. Res. Commun.* **373,** 315–318 (2008).

90. Cabaleiro-Lago, C., Quinlan-Pluck, F., Lynch, I., Dawson, K. A. & Linse, S. Dual Effect of Amino Modified Polystyrene Nanoparticles on Amyloid β Protein Fibrillation. *ACS Chem. Neurosci.* **1,** 279–287 (2010).

91. Daniel, M.-C. & Astruc, D. Gold Nanoparticles: Assembly, Supramolecular Chemistry, Quantum-Size-Related Properties, and Applications toward Biology, Catalysis, and Nanotechnology. *Chem. Rev.* **104,** 293–346 (2004).

92. Giljohann, D. A. *et al.* Gold Nanoparticles for Biology and Medicine. *Angew. Chem. Int. Ed.* **49,** 3280–3294 (2010).

93. Gerber, A., Bundschuh, M., Klingelhofer, D. & Groneberg, D. A. Gold nanoparticles: recent aspects for human toxicology. *J. Occup. Med. Toxicol. Lond. Engl.* **8,** 32 (2013).

94. Alkilany, A. M. & Murphy, C. J. Toxicity and cellular uptake of gold nanoparticles: what we have learned so far? *J. Nanoparticle Res.* **12,** 2313–2333 (2010).

95. Turkevich, J., Stevenson, P. C. & Hillier, J. A study of the nucleation and growth processes in the synthesis of colloidal gold. *Faraday Discuss*, 55-75 (1951).

96. Schlenoff, J. B., Li, M. & Ly, H. Stability and Self-Exchange in Alkanethiol Monolayers. *J. Am. Chem. Soc.* **117,** 12528–12536 (1995).

97. Goulet, P. J. G. & Lennox, R. B. New Insights into Brust−Schiffrin Metal Nanoparticle Synthesis. *J. Am. Chem. Soc.* **132,** 9582–9584 (2010).

98. Mie, G. Beiträge zur Optik trüber Medien, speziell kolloidaler Metallösungen. *Ann. Phys.* **330,** 377–445 (1908).

99. Liu, X., Atwater, M., Wang, J. & Huo, Q. Extinction coefficient of gold nanoparticles with different sizes and different capping ligands. *Colloids Surf. B Biointerfaces* **58,** 3–7 (2007).

100. Hendel, T. *et al.* In Situ Determination of Colloidal Gold Concentrations with UV–Vis Spectroscopy: Limitations and Perspectives. *Anal. Chem.* **86,** 11115–11124 (2014).

101. Chen, S. & Kimura, K. Synthesis and Characterization of Carboxylate-Modified Gold Nanoparticle Powders Dispersible in Water. *Langmuir* **15,** 1075–1082 (1999).

102. Ivanov, M. R., Bednar, H. R. & Haes, A. J. Investigations of the Mechanism of Gold Nanoparticle Stability and Surface Functionalization in Capillary Electrophoresis. *ACS Nano* **3,** 386–394 (2009).

103. Wang, Z., Wu, L. & Cai, W. Size-Tunable Synthesis of Monodisperse Water-Soluble Gold Nanoparticles with High X-ray Attenuation. *Chem. – Eur. J.* **16,** 1459–1463 (2010).

104. Feng, Z. V. *et al.* Impacts of gold nanoparticle charge and ligand type on surface binding and toxicity to Gram-negative and Gram-positive bacteria. *Chem. Sci.* **6,** 5186–5196 (2015).

105. Niidome, T., Nakashima, K., Takahashi, H. & Niidome, Y. Preparation of primary amine-modified gold nanoparticles and their transfection ability into cultivated cells. *Chem. Commun.* **0,** 1978–1979 (2004).

106. Lin, S.-Y., Tsai, Y.-T., Chen, C.-C., Lin, C.-M. & Chen, C. Two-Step Functionalization of Neutral and Positively Charged Thiols onto Citrate-Stabilized Au Nanoparticles. *J. Phys. Chem. B* **108,** 2134–2139 (2004).

107. Nishiyama, K., Kubo, A., Ueda, A. & Taniguchi, I. Surface pKa of Amine-Terminated Self-assembled Monolayers Evaluated by Direct Observation of Counter Anion by FT-Surface Enhanced Raman Spectroscopy. *Chem. Lett.* 80–81 (2002).

108. Hassinen, J., Liljeström, V., Kostiainen, M. A. & Ras, R. H. A. Rapid Cationization of Gold Nanoparticles by Two-Step Phase Transfer. *Angew. Chem. Int. Ed.* **54,** 7990–7993 (2015).

109. Joshi, P. *et al.* Tryptophan–Gold Nanoparticle Interaction: A First-Principles Quantum Mechanical Study. *J. Phys. Chem. C* **115,** 22818–22826 (2011).

110. Kihara, M. *et al.* Conformation of Amyloid Fibrils of β2-Microglobulin Probed by Tryptophan Mutagenesis. *J. Biol. Chem.* **281,** 31061–31069 (2006).

111. *Principles of Fluorescence Spectroscopy | Joseph R. Lakowicz | Springer*.

112. Gao, J., Lai, Y., Wu, C. & Zhao, Y. Exploring and exploiting the synergy of non-covalent interactions on the surface of gold nanoparticles for fluorescent turn-on sensing of bacterial lipopolysaccharide. *Nanoscale* **5,** 8242–8248 (2013).

113. Bodenhausen, G. & Ruben, D. J. Natural abundance nitrogen-15 NMR by enhanced heteronuclear spectroscopy. *Chem. Phys. Lett.* **69,** 185–189 (1980).

114. Schanda, P., Kupče, Ē. & Brutscher, B. SOFAST-HMQC Experiments for Recording Two-dimensional Deteronuclear Correlation Spectra of Proteins within a Few Seconds. *J. Biomol. NMR* **33,** 199–211 (2005).

115. Schanda, P. & Brutscher, B. Very Fast Two-Dimensional NMR Spectroscopy for Real-Time Investigation of Dynamic Events in Proteins on the Time Scale of Seconds. *J. Am. Chem. Soc.* **127,** 8014–8015 (2005).

116. Keeler, J., Clowes, R. T., Davis, A. L. & Laue, E. D. Pulsed-field gradients: theory and practice. *Methods Enzymol.* **239,** 145–207 (1994).

117. Grzesiek, S. & Bax, A. The importance of not saturating water in protein NMR. Application to sensitivity enhancement and NOE measurements. *J. Am. Chem. Soc.* **115,** 12593–12594 (1993).

118. Mulder, F. A. A., Schipper, D., Bott, R. & Boelens, R. Altered flexibility in the substrate-binding site of related native and engineered high-alkaline Bacillus subtilisins11Edited by P. E. Wright. *J. Mol. Biol.* **292,** 111–123 (1999).

119. Luginbuhl, P. & Wuthrich, K. Semi-classical nuclear spin relaxation theory revisited for use with biological macromolecules. *Prog. Nucl. Magn. Reson. Spectrosc.* **40,** (2002).

120. Stone, M. J. *et al.* Backbone dynamics of the Bacillus subtilis glucose permease IIA domain determined from 15N NMR relaxation measurements. *Biochemistry (Mosc.)* **31,** 4394–4406 (1992).

121. CARR, H. & PURCELL, E. Effect of Diffusion on Free Precession in Nuclear Magnetic Resonance Experiments. *Phys. Rev. - PHYS REV X* **94,** 630–638 (1954).

122. Meiboom, S. & Gill, D. Modified Spin-Echo Method for Measuring Nuclear Relaxation Times. *Rev. Sci. Instrum.* **29,** 688–691 (1958).

123. Cavanagh, J., Fairbrother, W. J., Palmer iii, A. G., Rance, M. & Skelton, N. J. CHAPTER 5 - RELAXATION AND DYNAMIC PROCESSES. in *Protein NMR Spectroscopy (Second Edition)* 333–404 (Academic Press, 2007). doi:10.1016/B978-012164491-8/50007-5

124. Palmer, A. G. & Massi, F. Characterization of the Dynamics of Biomacromolecules Using Rotating-Frame Spin Relaxation NMR Spectroscopy. *Chem. Rev.* **106,** 1700–1719 (2006).

125. Neudecker, P., Lundström, P. & Kay, L. E. Relaxation Dispersion NMR Spectroscopy as a Tool for Detailed Studies of Protein Folding. *Biophys. J.* **96,** 2045–2054 (2009).

126. Hansen, D. F., Vallurupalli, P. & Kay, L. E. Using relaxation dispersion NMR spectroscopy to determine structures of excited, invisible protein states. *J. Biomol. NMR* **41,** 113–120 (2008).

127. Kay, L. E., Torchia, D. A. & Bax, A. Backbone dynamics of proteins as studied by nitrogen-15 inverse detected heteronuclear NMR spectroscopy:

application to staphylococcal nuclease. *Biochemistry (Mosc.)* **28,** 8972–8979 (1989).

128. Dayie, K. T. & Wagner, G. Relaxation-Rate Measurements for 15N−1H Groups with Pulsed-Field Gradients and Preservation of Coherence Pathways. *J. Magn. Reson. A* **111,** 121–126 (1994).

129. Kay, L. E., Nicholson, L. K., Delaglio, F., Bax, A. & Torchia, D. A. Pulse sequences for removal of the effects of cross correlation between dipolar and chemical-shift anisotropy relaxation mechanisms on the measurement of heteronuclear T1 and T2 values in proteins. *J. Magn. Reson. 1969* **97,** 359–375 (1992).

130. Tollinger, M., Skrynnikov, N. R., Mulder, F. A. A., Forman-Kay, J. D. & Kay, L. E. Slow Dynamics in Folded and Unfolded States of an SH3 Domain. *J. Am. Chem. Soc.* **123,** 11341–11352 (2001).

131. Wang, C., Grey, M. J. & Palmer, A. G. CPMG sequences with enhanced sensitivity to chemical exchange. *J. Biomol. NMR* **21,** 361–366 (2001).

132. Fawzi, N. L., Ying, J., Ghirlando, R., Torchia, D. A. & Clore, G. M. Atomic-resolution dynamics on the surface of amyloid-β protofibrils probed by solution NMR. *Nature* **480,** 268–272 (2011).

133. Morris, K. F. & Johnson, C. S. Diffusion-ordered two-dimensional nuclear magnetic resonance spectroscopy. *J. Am. Chem. Soc.* **114,** 3139–3141 (1992).

134. Piotto, M., Saudek, V. & Sklenár, V. Gradient-tailored excitation for single-quantum NMR spectroscopy of aqueous solutions. *J. Biomol. NMR* **2,** 661–665 (1992).

135. Hwang, T. L. & Shaka, A. J. Water Suppression That Works. Excitation Sculpting Using Arbitrary Wave-Forms and Pulsed-Field Gradients. *J. Magn. Reson. A* **112,** 275–279 (1995).

136. Höök, F., Rodahl, M., Brzezinski, P. & Kasemo, B. Energy Dissipation Kinetics for Protein and Antibody−Antigen Adsorption under Shear Oscillation on a Quartz Crystal Microbalance. *Langmuir* **14,** 729–734 (1998).

137. Glomm, W. R., Halskau, Øyvind, Hanneseth, A.-M. D. & Volden, S. Adsorption Behavior of Acidic and Basic Proteins onto Citrate-Coated Au Surfaces Correlated to Their Native Fold, Stability, and pI. *J. Phys. Chem. B* **111,** 14329–14345 (2007).

138. Park, J.-W. & Shumaker-Parry, J. S. Structural Study of Citrate Layers on Gold Nanoparticles: Role of Intermolecular Interactions in Stabilizing Nanoparticles. *J. Am. Chem. Soc.* **136,** 1907–1921 (2014).

139. Becker, J. W. & Reeke, G. N. Three-dimensional structure of beta 2-microglobulin. *Proc. Natl. Acad. Sci. U. S. A.* **82,** 4225–4229 (1985).

140. Esposito, G. *et al.* Monitoring the Interaction between β2-Microglobulin and the Molecular Chaperone αB-crystallin by NMR and Mass Spectrometry αB-CRYSTALLIN DISSOCIATES β2-MICROGLOBULIN OLIGOMERS. *J. Biol. Chem.* **288,** 17844–17858 (2013).

141. Corazza, A. *et al.* Properties of Some Variants of Human β2-Microglobulin and Amyloidogenesis. *J. Biol. Chem.* **279,** 9176–9189 (2004).

142. TESHIMA, Y. & OGAWA, T. Dense Packing of Equal Circles on a Sphere by the Minimum-Zenith Method: Symmetrical Arrangement. *Forma* **15,** 347–364 (2001).

143. Rennella, E. *et al.* Equilibrium Unfolding Thermodynamics of β2-Microglobulin Analyzed through Native-State H/D Exchange. *Biophys. J.* **96,** 169–179 (2009).

144. Gümral, D. *et al.* Reduction of conformational mobility and aggregation in W60G β2-microglobulin: assessment by 15N NMR relaxation. *Magn. Reson. Chem. MRC* **51,** 795–807 (2013).

145. Esposito, G. *et al.* The Controlling Roles of Trp60 and Trp95 in β2-Microglobulin Function, Folding and Amyloid Aggregation Properties. *J. Mol. Biol.* **378,** 887–897 (2008).

146. Cantarutti, C. *et al.* Citrate-stabilized gold nanoparticles hinder fibrillogenesis of a pathological variant of β2-microglobulin. *Nanoscale* **9,** 3941–3951 (2017).

147. Jiang, W., Kim, B. Y. S., Rutka, J. T. & Chan, W. C. W. Nanoparticle-mediated cellular response is size-dependent. *Nat. Nanotechnol.* **3,** 145–150 (2008).

148. Wright, L. B., Palafox-Hernandez, J. P., Rodger, P. M., Corni, S. & Walsh, T. R. Facet selectivity in gold binding peptides: exploiting interfacial water structure. *Chem. Sci.* **6,** 5204–5214 (2015).

149. Feng, J. *et al.* Adsorption mechanism of single amino acid and surfactant molecules to Au {111} surfaces in aqueous solution: design rules for metal-binding molecules. *Soft Matter* **7,** 2113–2120 (2011).

150. Ishima, R. & Nagayama, K. Quasi-Spectral-Density Function Analysis for Nitrogen-15 Nuclei in Proteins. *J. Magn. Reson. B* **108,** 73–76 (1995).

151. Ishima, R. & Nagayama, K. Protein Backbone Dynamics Revealed by Quasi Spectral Density Function Analysis of Amide N-15 Nuclei. *Biochemistry (Mosc.)* **34,** 3162–3171 (1995).

152. Farrow, N. A., Zhang, O., Szabo, A., Torchia, D. A. & Kay, L. E. Spectral density function mapping using 15N relaxation data exclusively. *J. Biomol. NMR* **6,** 153–162 (1995).

153. Peng, J. W. & Wagner, G. Frequency spectrum of NH bonds in eglin c from spectral density mapping at multiple fields. *Biochemistry (Mosc.)* **34,** 16733–16752 (1995).

154. Lefèvre, J.-F., Dayie, K. T., Peng, J. W. & Wagner, G. Internal Mobility in the Partially Folded DNA Binding and Dimerization Domains of GAL4: NMR Analysis of the N−H Spectral Density Functions. *Biochemistry (Mosc.)* **35,** 2674–2686 (1996).

155. van de Weert, M. & Stella, L. Fluorescence quenching and ligand binding: A critical discussion of a popular methodology. *J. Mol. Struct.* **998,** 144–150 (2011).

156. Yacamán, M. J., Ascencio, J. A., Liu, H. B. & Gardea-Torresdey, J. Structure shape and stability of nanometric sized particles. *J. Vac. Sci.*

Technol. B Microelectron. Nanometer Struct. Process. Meas. Phenom. **19,** 1091–1103 (2001).

157. Dixon, M. C. Quartz Crystal Microbalance with Dissipation Monitoring: Enabling Real-Time Characterization of Biological Materials and Their Interactions. *J. Biomol. Tech. JBT* **19,** 151–158 (2008).

158. Dominguez-Medina, S., Blankenburg, J., Olson, J., Landes, C. F. & Link, S. Adsorption of a Protein Monolayer via Hydrophobic Interactions Prevents Nanoparticle Aggregation under Harsh Environmental Conditions. *ACS Sustain. Chem. Eng.* **1,** 833–842 (2013).

159. Chanana, M., Correa-Duarte, M. A. & Liz-Marzán, L. M. Insulin-Coated Gold Nanoparticles: A Plasmonic Device for Studying Metal–Protein Interactions. *Small* **7,** 2650–2660 (2011).

160. Neupane, S. *et al.* Probing the Aggregation Mechanism of Gold Nanoparticles Triggered by a Globular Protein. *J. Phys. Chem. C* **121,** 1377–1386 (2017).

8 PUBLICATIONS

Full papers related to the thesis

Cantarutti C., Bertoncin P., Corazza A., Giorgetti S., Mangione P. P., Bellotti V., Fogolari F. and Esposito G. (**2017**), Short-chain alkanethiol coating for small-size gold nanoparticles supporting protein stability. *Magnetochemistry*, *3*: 40-51.

Cantarutti C., Raimondi S., Brancolini G., Corazza A., Giorgetti S., Ballico M., Zanini S., Palmisano G., Bertoncin P., Marchese L., Mangione P., Bellotti V., Corni S., Fogolari F., Esposito G. (**2017**), Citrate-stabilized Gold Nanoparticles hinder fibrillogenesis of a pathologic variant of β2-microglobulin. *Nanoscale*, *9*: 3941-3951.

Brancolini G., Maschio M. C., Cantarutti C., Corazza A., Fogolari F., Bellotti V., Corni S., Esposito G. Citrate stabilized Gold Nanoparticles interfere with Amyloid Fibril formation: D76N and ΔN6 Mutants

Subject to minor revisions in *Nanoscale*

Cantarutti C., Raj G., Fogolari F., Corazza A., Giorgetti S., Bellotti V., Naumov P. and Esposito G. Interference of citrate-stabilized gold nanoparticles on β2-microglobulin oligomeric association.

In preparation

Cantarutti C., Bertoncin P., Corazza A., Giorgetti S., Mangione P.P., Bellotti V., Fogolari F. and Esposito G. Investigation of gold nanoparticle and β2-microglobulin interaction: impact of gold nanoparticle charge and size.

In preparation

Other full papers

Soler M.A., Rodriguez A., Russo A., Adedeji A.F., Dongmo Foumthuim C.J., Cantarutti C., Ambrosetti E., Casalis L., Corazza A., Scoles G., Marasco D., Laio A., Fortuna S. (**2017**), Computational design of cyclic peptides for the

customized oriented immobilization of globular proteins., *Phys Chem Chem Phys*, *19*: 2740-2748.

Şologan M., Cantarutti C., Bidoggia S., Polizzi S., Pengo P., Pasquato L. (**2016**), Routes to the preparation of mixed monolayers of fluorinated and hydrogenated alkanethiolates grafted on the surface of gold nanoparticles. *Faraday Discuss.*, *191*: 527–543.

Bosi S., Fabbro A., Cantarutti C., Mihajlovic M., Ballerini L., Maurizio P. (**2016**), Carbon based substrates for interfacing neurons: Comparing pristine with functionalized carbon nanotubes effects on cultured neuronal networks. *Carbon*, *97*: 87-91.

Prakasam T., Cantarutti C., Sharma S. K., Jagannathan R., Palmisano G., Giorgetti S., Corazza A., Bellotti V., Fogolari F., Olsen J.C., Trabolsi A., Esposito G.
Metal-organic trefoil knots inhibit *in vitro* amyloidogenesis.
Submitted

Kumar M., Thorn D. C., Cantarutti C., Bellotti V., Esposito G., Wilson M. R., Ecroyd H., Carver, J. A.
The molecular chaperones clusterin and αB-crystallin prevent primary and secondary nucleation of a potently amyloidogenic variant of β2-microglobulin.
In preparation